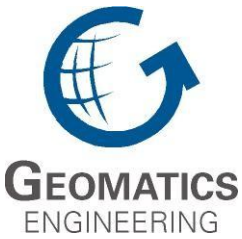

UCGE Reports
Number 20371

Department of Geomatics Engineering

DGPS and UWB Aided Vector-Based GNSS Receivers for Weak Signal Environments

(URL: http://www.geomatics.ucalgary.ca/graduatetheses)

by

Billy Chan

January 2013

UNIVERSITY OF CALGARY

DGPS and UWB Aided Vector-Based GNSS Receiver for Weak Signal Environments

by

Billy Chan

A THESIS

SUBMITTED TO THE FACULTY OF GRADUATE STUDIES

IN PARTIAL FULFILMENT OF THE REQUIREMENTS FOR THE

DEGREE OF MASTER OF SCIENCE

DEPARTMENT OF GEOMATICS ENGINEERING

CALGARY, ALBERTA

January 2013

Abstract

Vector-based GNSS (VBGNSS) receivers attempt to bridge the gap between Assisted GNSS (AGNSS) and High Sensitivity GNSS (HSGNSS); AGNSS use satellite orbit and network time information to predict the incoming satellite frequency during signal acquisition while HSGNSS enables the tracking of GNSS signals with strong attenuation. Similar to AGNSS, VBGNSS receivers make use of both satellite and receiver navigation information (position, velocity, and clock) to better estimate the incoming signal frequency and code-phase to improve the tracking sensitivity of weak GNSS signals.

The performance of VBGNSS receivers is proportional to the navigation solution accuracy; this research focuses on improving the performance of VBGNSS receivers using Ultra-Wideband (UWB) ranging and Differential GPS (DGPS) corrections. From the results presented herein, it was found that UWB ranging can improve the tracking sensitivity, position availability, and accuracy of a VBGNSS receiver; likewise DGPS can improve VBGNSS receiver performance in certain operating environments.

Acknowledgements

To my supervisor, Dr. Mark Petovello, this thesis could not exist without your guidance and encouragement. Thank you for your gracious support and for providing me with this opportunity to explore my interests in the field of navigation.

This work was funded in part by Alberta Innovates Technology Futures; funding was also provided by scholarships from the Faculty of Graduate Studies at the University of Calgary and the Institute of Navigation.

To the wonderful and diverse members of Position Location And Navigation (PLAN) Group, thank you for bearing with me in signing out all the lab equipment for my wildly ambitious data collections. To this end, I must acknowledge Behnam Aminian, Nima Sadrieh, Zhe He, Tao Lin, Boxiong Wang, and Da Wang; thank you for your help in making my data collections possible.

To the administrative staff at the Department of Geomatics, thank you for all your hard work behind the scenes and making my research possible.

To my parents, thank you for instilling in me a love for engineering and the natural sciences. Thank your also for you continued support and encouragement through the many years that led up to the completion of my thesis.

To my Mom and Dad

Cindy and Andrew

Table of Contents

List of Tables

List of Figures and Illustrations

List of Symbols, Abbreviations and Nomenclature

Symbol	Definition
AGNSS	Assisted GNSS
C/A	Coarse Acquisition
DGPS	Differential GPS
DOP	Dilution Of Precision
GLONASS	GLObal NAvigation Satellite System
GNSS	Global Navigation Satellite System
GPS	Global Positioning System
ICD	Interface Control Document
IF	Intermediate Frequency
IMU	Inertial Measurement Unit
INS	Inertial Navigation System
KF	Kalman Filter
LNA	Low Noise Amplifier
LOS	Line Of Sight
PRN	Pseudorandom Noise
RF	Radio Frequency
RMS	Root Mean Square
UWB	Ultra-wide Band

Chapter One: Introduction

The proliferation of Global Navigation Satellite System (GNSS) technologies into mainstream consumer products for positioning, navigation and timing (PNT) has been rapidly accelerating over the past decade. As early as 2009, Global Positioning System (GPS) technologies reached 100 percent penetration in the smartphone industry (van Diggelen 2009b). However, the spread of wireless positioning is not solely limited to mobile phones for pedestrian navigation. Asset tracking, vehicular navigation, and global time synchronization can and do take advantage of the benefits that GNSS have to offer. The main drivers for the mass adoption of GNSS technologies in civilian applications over the last decade can be largely attributed to two fundamental shifts in the way GNSS receivers operate. These two fundamental changes are the introduction of Assisted-GPS (AGPS) and High-Sensitivity GPS (HS-GPS). By incorporating assistance information such as satellite orbit, coarse position, timing and frequency information, AGPS receivers gained the ability to acquire satellite signals and obtain a position solution within seconds after starting up. HS-GPS further improved the signal tracking performance of GPS receivers operating in weak signal environs such as those found indoors and beneath heavy foliage by using open-loop block processing receiver architectures that employ a vast number of parallel correlators (van Graas et al 2005). Although the block processing approach greatly improved the robustness of HS-GPS receivers while operating in weak signal environments, its main drawback was the increase in power consumption due to the large computational load of using a large number of parallel correlators. More recently, much effort has been spent on using vector-based receiver architectures for

tracking weak GNSS signals (Psiaki 2001, Psiaki & Jung 2002, Petovello & Lachapelle 2006, Kim et al 2008, Won et al 2009, Groves & Mather 2010). The vector-based approach takes advantage of the estimated position, velocity and clock states of the GNSS receiver and combines this with the satellite trajectory information computed using the satellite ephemeris to estimate the frequency and code phase of the incoming signal being tracked. By using this method, the tracking sensitivity of weak GNSS signals is greatly improved, while at the same, the computational load required by a vector-based receiver is much lower as compared to an open-loop block processing architecture found in most HS-GPS receivers.

The research presented herein seeks to further enhance the capabilities of the vector-based GNSS receiver with a specific emphasis on indoor navigation. Since the performance of vector-based GNSS signal tracking algorithms depend greatly on the accuracy of the estimated receiver position, velocity and clock states, techniques that improve the accuracy of the navigation solution will also serve to enhance the signal tracking performance of a vector-based receiver. To this end, the work presented here seeks to improve the navigation solution accuracy of vector-based GNSS receivers operating in challenging indoor environments through the use of differential GPS (DGPS) corrections and ultra-wideband (UWB) ranging techniques. Although these techniques were originally designed to improve the navigation solution accuracy and availability when combined using tight-coupling (Petovello et al 2010, MacGougan et al 2010), the objective of this research is to determine the impact of combining DGPS and UWB augmentation techniques with a vector-tracking GNSS receiver (Chan & Petovello

2011). By means of a vector-based GNSS receiver, DGPS corrections and UWB range measurements serve, not only to improve the navigation accuracy of a GNSS receiver, but also serves to improve the GNSS signal tracking performance as well. The details of how aiding and augmentation techniques enhance the capabilities of GNSS receivers is discussed below; however, it is important to first discuss how a Global Navigation Satellite System work.

1.1 Background

The following subsections present a brief history of the Global Positioning System and introduce the techniques used to enhance the capabilities of modern GNSS receivers. These techniques include assisted GPS, high-sensitivity GPS, vector-based signal tracking, differential GPS, and UWB augmentation.

1.1.1 History of the Global Positioning System

When GPS was first developed by the United States Air Force, it was a military system designed to operate with direct Line Of Sight (LOS) between a GPS receiver and satellites in space. By transmitting a navigation message that allows a GPS receiver to determine the position of the satellite at any given time, the receiver can then use the satellite position along with pseudorange measurements between it and the satellite to derive its position. Due to the limited power availability for satellites in space and the vast distances that separate a GPS receiver from the satellites in view, by the time the GPS signals reaches the receiver, they are extremely weak and fall below the background electromagnetic radiation level. In order to overcome this problem, GPS satellites make

use of Code Division Multiple Access (CDMA) where a Pseudo-Random Noise (PRN) code is modulated on top of a continuous carrier signal and is repeated every one millisecond for the GPS L1 Coarse Acquisition (C/A) signal. In order to allow GPS receivers to determine the satellite position at a particular instant in time, a binary navigation message that contains the time of transmission and other orbital parameters are modulated on top of the PRN code. The navigation message is transmitted at a rate of 50 bits per second and the satellite's orbital parameters – the ephemerides – are repeated at 30 second intervals.

Upon reaching the receiver, a Doppler removal and correlation process is performed on the incoming signal using a local replica version of the same PRN code transmitted by the satellite being tracked. Doppler removal is performed by generating the local replica PRN code to match the incoming signal such that the two are aligned in the frequency domain. By performing a cross-correlation between the very weak incoming GPS signal and a local replica PRN code, the incoming signal is then despread and brought above the background noise (ARINC Research Corporation 2000). An added advantage of using a CDMA signal structure is that all GPS satellites can transmit on the same frequency since the correlation process will reject signals that are different from the local replica PRN code being used to track a particular satellite. The binary sequences that form a PRN code appear random in nature and the set of 32 PRN codes used for GPS satellite transmission were selected for their low cross-correlation properties (Wallner & Ávila-Rodríguez 2011).

1.1.2 Assisted GPS

Although the use of PRN spreading codes allowed GPS receivers to the track very weak line of sight signals, the slow transmission rate of the navigation message meant that it can take 30 seconds or more for a GPS receiver to download the navigation message once it has locked onto a GPS satellite's signal. This is because the ephemerides that contain the orbital parameters used for determine a satellite's position is repeated only once every 30 seconds and takes 6 seconds to transmit. Moreover, the ephemeris broadcasted by GPS satellites has a validity period of only four hours and are typically updated every two hours. Because of this, if a GPS receiver is shut off for more than several hours, upon power up, it would need to wait another 30 seconds or more before it can obtain the new ephemeris data to compute a satellite's position with an accuracy of several meters.

The development of Assisted GPS (AGPS) sought to overcome the long time required for a GPS receiver to obtain a position fix – commonly referred to as Time To First Fix (TTFF). The major contributing factor to long TTFF for traditional GPS receivers was the need to download the satellite ephemeris in order to obtain a position fix. Since data transfer rates of cellular networks and Wi-Fi internet connections are typically much higher than 50 bits per second, satellite ephemeris data can be made available to GPS receivers much quicker than obtaining such data directly from a GPS satellite. Moreover, precise orbits of GNSS satellites can be predicted many days in advanced using sophisticated satellite orbit modelling techniques (Derbez & Lee 2008). By either downloading the satellite ephemeris through other communication channels or predicting

the ephemeris in advance based on previous ephemeris data, AGPS enabled GPS receivers to greatly reduce the TTFF down to several seconds or less.

Other assisted GNSS data used to improve TTFF include coarse position estimates, reference timing and frequency aiding. Once ephemeris information is available, the position and velocity for all available satellites can be estimated. Provided that a rough position estimate of the receiver is available, the expected Doppler observed by the receiver for all available satellites can be computed. This then allows the receiver to reduce the frequencies that it must check when trying to determine whether the signal from a particular satellite is present or not. If the GPS receiver time can be determined to within a few seconds of the reference GPS time, the same ephemeris information and rough receiver position can be used to greatly reduce the number of code delay bins required for signal acquisition (van Diggelen 2009a). If a reference frequency is available, the frequency error on a GPS receiver oscillator can then be estimated beforehand, thereby reducing the uncertainty of the receiver clock frequency error – commonly referred to as clock drift. For mobile phones applications, this reference frequency is typically provided through the cellular phone's internal oscillator which is synchronized with the cellular network (van Diggelen 2009a).

An example provided by van Diggelen (2009a) shows that if the receiver time is known to within 2 seconds of the true GPS time, an initial position estimate accurate to within 3 km in the horizontal direction and 100 m in the vertical direction is available, a reference frequency is known to 100 ppb and the maximum speed is limited to 160 km/h, the

frequency search space can be reduced to ±630 Hz. This is just 16 percent of the typical ±4 kHz search space used in the absence of a priori information. Likewise, for the same scenario, the code-delay can be reduced to ±22 chips.

Although ground-based ephemeris transmission, ephemeris prediction, coarse position, time and frequency assistance information as described above focuses specifically on aiding GPS receivers, these techniques also apply to other GNSS such as the Russian GLObal NAvigation Satellite System (GLONASS), the European Galileo GNSS, and the Chinese Beidou/Compass GNSS as well. However, it is important to note that once a GPS receiver has acquired the available signals and a position solution has been obtained, the assistance data is no longer used. This is because such assistance data, at the moment at least, cannot be used to enhance the performance of the GNSS signal tracking loops. Because of this, high-sensitivity GNSS, Kalman filter tracking, and vector-based tracking techniques have all been actively developed to improve the tracking sensitivity and robustness of GNSS receivers operating in weak signal environments; these techniques are discussed in the following subsections.

1.1.3 High Sensitivity GNSS

The primary objective of using High Sensitivity GNSS (HS-GNSS) techniques is to improve the tracking performance of weak GNSS signals in environments such as urban canyons, beneath heavy foliage and indoor locations. By allowing GNSS receivers to track highly attenuated GNSS signals in environments that a traditional GNSS receiver would otherwise be rendered ineffective using standard signal tracking techniques, the

GNSS navigation solution availability is greatly increased while operating in weak signal environments. Such HS-GNSS techniques include the use of long signal integration periods (in excess of 20 ms) and open-loop block processing receiver architectures. It should be noted that, although HS-GNSS can improve the positioning availability of GNSS receivers, it does not necessarily guaranty an improvement in the positioning accuracy. This is because GNSS signals tend to be corrupted by large multipath ranging errors in the presence of nearby reflectors that may include tall buildings and nearby vehicles.

One of the first developments in the area of HS-GNSS was to extend the integration period of GNSS signals during the Doppler removal and correlation processing – more specifically, the "integrate and dump" step commonly found in commercially available GNSS receivers. During the integrate-and dump step, 1 millisecond blocks of Intermediate Frequency (IF) data from the RF front-end are typically integrated to increase the Signal to Noise Ratio (SNR) (Ward et al 2006). The primary reason that this operation is performed in 1 millisecond blocks is because the GPS L1 C/A code is repeated every millisecond. Since the navigation message on the GPS L1 C/A code is transmitted at a data rate of 50 bits per second, a bit change may occur every 20 milliseconds. For receivers that do not have a priori information about the incoming navigation message bits, the maximum integration period is limited to 20 milliseconds. However, by knowing or predicting the navigation message bits, the integration period can be extended up to several seconds. By doing so, the detection sensitivity can allow

for weak signals with a carrier to noise density ratio (C/N_0) as low as 5 dB-Hz to be detected (Watson et al 2006).

Aside from the need to accurately predict the navigation message bits, two other obstacles that limit the duration of long integration periods are the receiver dynamics and the stability of the oscillator used to control the RF front-end sampling rate. Although the cost of high quality oscillators such as oven-controlled crystal oscillators (OCXO) may be prohibitively high for low-cost GNSS applications, their deployment is nonetheless an effective solution to allow GNSS receivers to extend their integration period and thereby improve their tracking sensitivity.

Many HS-GNSS receivers also make use of open-loop block processing architectures to improve robustness in tracking weak signals. Open-loop block processing typically employs millions of parallel correlators, each checking a different frequency and code phase combination, to determine the Doppler and pseudorange of the incoming signal. Although this allows HS-GNSS receivers to reliably make use of weak signals with large signal dynamics, the massively parallel correlator architecture is very computationally expensive; this results in increased power consumption and limits the use of such receivers in low-power devices (van Graas et al 2005).

1.1.4 Kalman Filter Tracking

Another method for improving GNSS signal tracking performance is through the use of Kalman filter tracking loops. In a traditional GNSS receiver, a local replica version of the

incoming GNSS signal is generated by a Numerically Controlled Oscillator (NCO). The local replica signal is then used in the Doppler removal and correlation of the incoming signal. Differences in frequency, code phase and carrier phase between the local replica and the incoming signal is determined using frequency, code, and carrier phase discriminators, respectively (Spilker 1996). Because the frequency, code phase and carrier phase of a GNSS signal are directly related to the receiver position and velocity, these signal parameters are time-variant by nature. Frequency, code, and phase discriminators on the other hand treat GNSS signal parameters as time-invariant; one consequence of this is that information from past epochs, which can be used to predict the parameters in future epochs, are left unused. Kalman filter based tracking loops seek to overcome this weakness in traditional GNSS tracking loops.

Kalman filter based tracking loops take advantage of the time-variant nature of GNSS signal parameters by employing a dynamics model that predicts the incoming signal based on signal parameters estimated in previous epochs. Doing so allows the tracking loop to operate in situations where the receiver may experience large signal dynamics (Psiaki & Jung 2002, Ziedan & Garrison 2004). By exploiting a Kalman filter for GNSS signal tracking, it has been found that Kalman filter tracking can provide a C/N_0 gain of 2 dB and an increase in code tracking accuracy of 25% and a C/N_0 gain of 3 dB along with a 30% improvement in accuracy for Doppler tracking (Won et al 2009).

1.1.5 Vector-based and Ultra-Tight GNSS Signal Tracking

Other methods have been developed to account for line of sight signal dynamics caused by receiver motion. In ultra-tightly coupled receiver architectures, high-rate (typically 50-200 Hz) Inertial Measurement Units (IMU) are used to measure receiver motion and estimate the movement of the GNSS antenna. By knowing the antenna motion, it is then possible to communicate this information to the GNSS signal tracking loops to account for the line of sight dynamics between the GNSS receiver and the satellite being tracked (Groves et al 2007, Petovello et al 2007a, Petovello et al 2007b). Similar to alleviating oscillator instability by using high quality oscillators, signal tracking performance can be improved by employing IMUs in GNSS receivers through ultra-tightly coupled signal tracking loops; however, even the use of low-grade IMUs can be a problem in extremely cost sensitive applications. Furthermore, the power requirements of IMUs present an added burden that may prohibit the use of ultra-tight receivers in some consumer applications.

Vector-based GNSS receiver architecture seeks to allow the GNSS receiver tracking loops to account for receiver dynamics without the need for costly IMUs. On a conventional GNSS receiver, each signal from a particular satellite being tracked is assigned to a corresponding channel. These channels contain a tracking loop where Doppler removal and correlation processing takes place. The correlator outputs are then used to estimate the code phase, Doppler frequency and carrier phase of the incoming signal. After this, estimates of the incoming signal frequency, code phase and carrier phase are used to drive the channel's NCO which generates the local replica signal for the

next epoch. It is important to note that although the GNSS receiver consists of many channels that work in parallel for tracking multiple satellites at the same time, each channel operates independently from each other. This method of GNSS signal tracking where each GNSS signal is tracked independently is commonly referred to as a scalar tracking. Because each tracking loop within the receiver operates independently, using information from one channel to aid another is impossible and changes in receiver position, velocity, clock offset and clock drift (which affect all channels) are entirely ignored (Petovello & Lachapelle 2006).

What is different on a vector-based receiver is that, instead of using tracking loop estimates of the frequency, code phase and carrier phase to drive the NCO as in a scalar tracking receiver, the vector-based receiver takes the estimated position, velocity, clock offset and clock drift from its navigation filter outputs and combines this with the satellite position, velocity and clock information to drive the NCO. Because the position, velocity and clock terms for both the receiver and the tracked satellites are known, the incoming signal frequency and code phase can be estimated directly and fed to the NCO for each channel. This effectively accounts for any line of sight signal dynamics that caused by the motion of the GNSS receiver provided that the receiver's position and more importantly the velocity and clock estimates are sufficiently accurate. The vector-based receiver architecture is very similar to that found in an ultra-tight receiver. As a matter of fact, an ultra-tight receiver can be viewed as an extension of the vector-based receiver. What sets the vector-based receiver apart from an ultra-tight receiver is that it does not make use of any measurements from IMUs and the navigation filter on a vector-based receiver

operates at a lower update rate (typically 20 Hz or less) as compared to one found on an ultra-tight receiver (typically 100 Hz or more).

In tests performed at Stanford University, it was found that a vector-based GNSS receiver is capable of achieving a gain in C/N_0 of 2-6.5 dB when compared with a conventional scalar tracking receiver; the average C/N_0 gain over a 14 hour test period was 5.1 dB (Lashley & Bevly 2009). Moreover, further testing and analysis performed at the University FAF Munich in Germany has been able to determine that when Kalman filter-based tracking is combined with a vector tracking receiver architecture, 7 dB of C/N_0 gain can be achieved. Of the 7 dB, 2-3 dB can be attributed to the Kalman filter tracking, while the rest of the performance improvement is due to the global loop closure provided by the vector-based architecture (Won et al 2009).

While vector-based tracking can improve the receiver tracking sensitivity without the need for an IMU, it is important to bear in mind that a sufficiently accurate estimate of receiver position, velocity, clock offset and clock drift are paramount to the stability of the tracking loops since they are used directly drive the NCOs on each receiver channel. Because of this, any large errors in the estimated position, velocity or clock states within the navigation filter may contribute to a loss of lock on all channels. With this in mind, the tuning of the navigation filter along with the actual receiver dynamics also has a large influence on the performance of a vector-based receiver. Since the update rate of the navigation filter from a vector-based receiver is considerably lower than an ultra-tight

receiver, a vector-based receiver is less tolerant to large changes the receiver dynamics when compared to an ultra-tight receiver.

Given the weaknesses and limitations of vector-based tracking loops, it should be noted that the primary factor that affects the tracking performance of vector-based receivers is the accuracy and update rate of the navigation solution. Since 3-5 dB of C/N_0 gain comes from the global loop closure within a vector-based receiver (Won et al 2009), this improvement in tracking performance can be gained or lost based on the quality of the navigation solution. With this in mind, an improvement in the navigation solution – both in terms of its availability and accuracy – can significantly improve a vector-based GNSS receiver's ability to track weak signals. Two methods that can be used to improve the navigation solution of a vector-based receiver are the use of differential GNSS corrections and Ultra-wideband ranging measurements; these techniques are discussed in the following subsections.

1.1.6 Differential GNSS

The use of differential GNSS techniques is primarily focused on the removal of systematic errors present in GNSS observations. Differencing of satellite observations such as pseudorange, Doppler and carrier phase observations may be performed either between receivers, between satellites and between epochs. When single linear combinations of satellite observations are formed either between receivers, satellites or different epochs, this is commonly referred to as a single difference (SD) between

observations. Likewise, performing linear combinations between two SD observations is commonly referred to as double differencing (DD).

Between-receiver SD has the effect of removing systematic errors that are common between two nearby receivers. These systematic biases include satellite orbit errors, satellite clock errors, tropospheric delay, ionosphere errors and the receiver clock offset component that is common between two receivers. Since the receiver clock offset component that is common between two receivers is removed through single differencing, the clock state that results from the navigation solution is the relative receiver clock offset between two receivers. Also, the tropospheric delay, ionosphere errors and satellite orbit error that show up in GNSS observations is spatially correlated; as distance between two receivers grows, the amount of systematic errors that can be removed by between-receiver differencing also diminishes (Petovello 2011).

Between-satellite SD observations are typically formed by generating linear combinations of satellite observations with respect to one particular satellite. This has the effect of removing systematic errors that are common between a pair of satellite observations – namely, the receiver clock offset and drift states. Although forming between-satellite SD pseudorange observations will remove the need to solve for the receiver clock errors, because one satellite is used as the 'base' satellite from which all other SD observations are generated, forming between-satellite SD observations also come at the expense of removing one pseudorange observation from the navigation solution. Similar to using between-satellite pseudorange observations, if between-satellite

SD Doppler observations are used, the receiver clock drift state can be eliminated from the solution at the expense of one Doppler observation. As using between-satellite SD observations does not serve to improve positioning accuracy, between-satellite differencing is rarely used except in the context of resolving integer carrier phase ambiguities where GNSS observations are differenced between both satellites and receivers to form double differenced observations.

An alternative to using between-receiver SD observations to improve the positioning accuracy is to directly estimate the ranging errors as observed by a GNSS receiver. Once these ranging errors are known, they can be subtracted from the observations of other nearby GNSS receivers. Compared to using between-receiver SD observations, the primary benefit in using a corrections-based approach for reducing GNSS errors such as tropospheric delay, ionosphere errors, and satellite orbital errors, is that the GNSS receiver that accepts observation corrections from a nearby receiver is still capable of directly estimating an absolute receiver clock bias and drift. In the context of implementing a vector-based receiver, the absolute clock bias and drift terms are needed by the NCO to generate a local replica version of the incoming signal.

It should be noted that, although differential GNSS techniques present an effective solution for mitigating systematic errors with a high degree of spatial correlation that exists between multiple receivers, these techniques also increase non-systematic errors such as multipath and receiver noise. This is because multipath errors have a very low degree of spatial correlation (Jost et al 2010) and receiver noise is a random process that

is receiver dependent. When linear combinations of satellite observations are formed between two receivers, stochastic errors such as pseudorange multipath and receiver noise errors are combined. Subsequently, the standard deviation of the SD observation is increased by a factor of $\sqrt{2}$. With this in mind, for environments where multipath errors are very large, using between-receiver SD observations may increase the stochastic errors to such a point where the increase in stochastic errors from forming SD observations actually become greater than the decrease in systematic errors.

The goal of providing differential GNSS corrections to a vector-based GNSS receiver is to improve the position accuracy of the GNSS receiver, thereby allowing the receiver to better predict the line of sight signal from the satellite. Moreover, by removing systematic biases in the GNSS measurements through a corrections-based approach, receiver clock offsets can still be estimated directly within a GNSS receiver's navigation solution. This receiver clock offset estimate is important as it is required to determine the incoming signal within the vector-based receiver.

1.1.7 Ultra-Wideband Ranging

Unlike differential GNSS observations which cannot be used when common GNSS measurements are not available between two receivers, Ultra-Wideband (UWB) ranging measurements operate independently from GNSS (Yan & Bellusci 2009, Ni et al 2010). Therefore, UWB ranging provides an effective means for augmenting GNSS observations in environments where GNSS signals are either denied or heavily degraded (Vydhyanathan et al 2009, Chiu 2008, MacGougan & Klukas 2009, MacGougan et al

2010, Petovello et al 2010). UWB ranging operates through measuring the time required to send and return an RF signal between two radios. First, a polling radio starts by sending a polling message to nearby UWB responder radios. Once the signal reaches the desired responder radio and is detected, the responder radio waits a predetermined amount of time before sending a return message to the polling radio. The total time required by the polling radio to initiate the polling message and detect a response message is equal to the two-way time of flight of the RF signal plus the predetermined response time of the responder radio. By knowing how long an RF signal requires to travel between two radios, it is then possible to compute the distance that separates the two (MacGougan et al 2010).

The main error sources that influence UWB ranging accuracy are RF propagation delays that are a function of the density of the medium in which UWB signals must penetrate, multipath errors from reflected signals, and system clock offsets that exist between the UWB radio logging software and the reference GNSS time standard. UWB ranging errors can be modelled using scale factor and bias components on a per-radio-pair basis and a time shift for UWB range measurements can be applied to account for the UWB-GNSS system clock offset (MacGougan & Klukas 2009).

It is important to bear in mind that, to date, the use of UWB ranging for navigation has been primarily focused on using UWB as either stand-alone navigation systems (Yan & Bellusci 2009, Xu et al 2007, MacGougan et al 2009, Xu 2006) or as tightly-integrated GNSS/UWB navigation systems (MacGougan et al 2010). The work presented herein

takes GNSS and UWB measurements to a deeper level of integration wherein UWB range measurements are used to aid the GNSS signal tracking loops within the receiver – this is referred to as an aided GNSS vector-tracking loop (Lashley & Bevly 2009).

1.2 Scope and Objective of Research

The scope of this thesis is the signal tracking of weak GPS L1 C/A signals in high multipath environments, both indoors and out. The impact of using corrections-based Differential GPS (DGPS) and Ultra-Wideband (UWB) ranging techniques in an ultra-tightly coupled manner for aiding a vector-based GNSS receiver is discussed. It does not deal with signal acquisition in weak signal environments and, as such, the GNSS receiver is always initialized in an outdoor, open-sky environment for all datasets discussed in this thesis. Another reason for initializing the vector-based receiver in an open-sky environment is to ensure that the receiver has a valid set of ephemerides for each satellite in view. This is important since vector tracking requires receiver navigation information to be able to predict the parameters of the incoming line-of-sight signal. Without a valid ephemeris, the receiver cannot compute the position, velocity and clock terms of satellites in view, nor can it estimate the receiver's own navigation solution. Moreover, the signal strength required in GNSS signal acquisition is generally much higher than that needed for tracking in a vector-based tracking loop. Therefore, unless a high sensitivity assisted GNSS acquisition algorithm is employed whereby information such as external ephemerides, along with receiver position, velocity, time and frequency estimates are used, such weak signal environments would pose an major challenge for conventional GNSS signal acquisition algorithms..

As discussed in section 1.1.5, the gain in tracking sensitivity that a vector-based receiver provide is primarily a function of the navigation solution accuracy of the receiver itself. In previous work where vector-based receivers have been developed, tested and analyzed, the navigation solution of these receivers have all been computed based solely on GNSS measurements generated within the receiver itself. To this end, the objective of this research is to expand on the basic vector-based receiver architecture by improving the accuracy and availability of the receiver navigation solution using DGPS corrections and UWB range measurements. DGPS corrections are generated using pseudorange residuals obtained from the navigation filter of a software GNSS receiver located in an open-sky environment. This receiver does not attempt to model or identify components of GPS propagation errors such as tropospheric delay, ionosphere delay and multipath errors. GPS and UWB observations are assumed to be completely independent and have no effect on each other. Furthermore, UWB ranging errors in real-world data are assumed to consist of a scale factor and bias component that vary between radio pairs and is modelled to remove most (but not all) of the systematic effects found in UWB ranges. Time offsets between UWB ranges and GPS observations are assumed to be random constants that are determined empirically by shifting the observed UWB ranges to match, as closely as possible, the reference ranges generated using the reference/surveyed coordinates of the UWB radios and the reference trajectory of the receiver of interest.

The objective of this thesis is to assess the benefits of augmenting a vector-based GNSS receiver with DGPS corrections from other nearby receivers, and using UWB augmentation to improve the GNSS signal tracking performance of a vector-based

receiver. The environments used to assess such benefits include the upstairs and basement areas of a wooden single story residential house, an urban canyon environment and the inside of a three story commercial building with a large glass façade.

1.3 Main Contributions

This research focuses on the tracking of weak GNSS signals in urban environments using a vector-based GNSS receiver architecture and assesses the benefits of aiding such architecture by means of adding DGPS corrections and UWB ranging observations. To this end, the research focuses primarily on various aspects of signal tracking performance and availability. Although the importance of navigation accuracy is of secondary interest in this work since signal tracking performance of a vector-based GNSS receiver is inextricably tied to the accuracy of its navigation filter, the analysis of a receiver's navigation performance will be used as an investigative tool for understanding how DGPS and UWB ranging influences the performance of a vector-based GNSS receiver as a whole.

The main contributions of this research include:

1. Characterizing the benefits and limitations in using DGPS and UWB augmentation techniques for vector-based GNSS receivers. Since many indoor navigation applications currently require the use of costly inertial sensors, this assessment is important for the continued development and growth of low-cost indoor navigation applications. Such characterization includes the:

a. Analysis of signal tracking performance improvements provided by DGPS and UWB augmentation on a vector-based GNSS receiver operating in various urban environments
b. Investigation of real-world benefits and limitations of using UWB ranging techniques for improving the navigation accuracy in urban environments.
c. Assessing the limits for which UWB augmentation can improve the performance of a vector-based GNSS receiver given simulated ranges while operating in harsh indoor signal environments.

2. Development and testing of a vector-based software GNSS receiver capable of incorporating DGPS corrections and UWB ranging observations for improved navigation accuracy.

1.4 Author's Contribution

The author has acted as a third author for the publication (Petovello et al 2010), and first author for the publication (Chan & Petovello 2011).

The author has contributed to (Petovello et al 2010) by collecting data and writing software for resolving float carrier phase ambiguities on multiple moving-baselines using GNSS and UWB observations between three vehicles.

The author's contribution to (Chan & Petovello 2011) has been to assess the benefits of using UWB ranges and single differenced DGPS observations in a vector-based GNSS

receiver, and to write software for allowing such capabilities in an existing standalone vector-based GNSS receiver.

1.5 Thesis Outline

The concepts and principles of satellite navigation and UWB ranging are presented in Chapter 2. The performance improvements provided by a vector-based receiver as compared to a scalar receiver design is demonstrated and reviewed in Chapter 3. The development of the navigation filter used to combine GPS measurements with DGPS corrections and UWB ranges is described in Chapter 4; this chapter also includes a description of the receiver test environment, equipment setup, and the methodology for obtaining a reference navigation solution. Chapter 5 analyzes the performance improvements gained by aiding a vector-based GNSS receiver with UWB range measurements and DGPS corrections; this chapter focuses on receiver performance differences in signal tracking sensitivity, GPS measurement quality, navigation solution availability and accuracy. Lastly, Chapter 6 summarizes the work performed, concludes this thesis with the findings, and provides a list of recommended work for future research.

Chapter Two: Wireless Positioning

2.1 Overview

The purpose of this chapter is to provide the background information required to understand the various components which make up the receiver architecture developed in this research. To do this, one must understand how GNSS signals are acquired and the operation of a GNSS signal tracking loop. Moreover, differential GNSS and UWB ranging techniques are presented to demonstrate how they can be used to improve a conventional vector-based GNSS receiver.

This chapter details the concepts of wireless positioning using GNSS and UWB ranging observations. It begins by giving an overview of the GPS signal structure. Key components of a software GNSS receiver are then discussed and details of their roles and functions are presented. This is followed by a review of the primary sources of errors found in GNSS positioning. Differential GNSS techniques are then presented with an emphasis on how these techniques can remove or reduce systematic biases commonly found in GNSS observations. Finally, the concept of UWB ranging and positioning is discussed along with the advantages of combining UWB ranging techniques with GNSS positioning for improved navigation accuracy in environments where GNSS observations are either severely degraded or unavailable.

2.2 GPS Signal Structure

The Navstar Global Positioning System (GPS) currently broadcasts on three frequencies: namely L1 with a centre frequency of 1575.42 MHz, L2 centred at 1227.60 MHz, and L5 at 1176.45 MHz. Only the GPS L1 Coarse Acquisition (C/A) signal was used for the results presented in this dissertation. As such, the Navstar L2 and L5 signals, along with other GNSS signals such as those transmitted by GLONASS, Galileo, and Compass will not be discussed herein. The Navstar GPS L1 signal can be represented in the time-domain by equation (2.1) where s_{L1} represents the L1 signal, k is for the kth satellite, P_c and P_{Y1} are the signal powers for the civilian C/A-code and encrypted military P(Y)-code, respectively. x^k and y^k are the PRN codes for the C/A- and P(Y)-code on satellite k, $D^{(k)}$ is the data bit stream for the navigation message, f_{L1} is the centre frequency of the GPS L1 signal, and θ_{L1} is the phase offset (Misra & Enge 2006a).

$$s_{L1}^k(t) = \sqrt{2P_c}\,x^k(t)D^k(t)\cos(2\pi f_{L1}t + \theta_{L1}) + \sqrt{2P_{Y1}}\,y^k(t)D^k(t)\sin(2\pi f_{L1}t + \theta_{L1}) \quad (2.1)$$

In the context of navigation and positioning, the C/A code phase from $x^k(t)$ is tracked by the GNSS receiver to generate pseudorange observations, and the frequency f_{L1} is used to generate Doppler observations. Since the navigation message bits, $D^k(t)$, are transmitted at a rate of 50 bits per second and have a value of either +1 or -1, once the location of the transitions are known, the data bits remain constant over the entire signal integration period for tracking loops operating with a measurement output rate of 20 Hz or less.

2.3 Software Defined GNSS Receiver

The development of software GNSS receivers began in earnest near the start of the 21st century (Schamus & Tsui 1999, Thor et al 2002, Schamus et al 2002, Pany et al 2004, Ma et al 2004). Although software GNSS receivers perform the exact same set of tasks as those found on hardware GNSS receivers used in many commercial applications, what sets a software receiver apart is the flexibility that it allows for the rapid development, testing, and deployment of new signal structures as well as acquisition and tracking algorithms (O'Driscoll et al 2006). In particular, when used with an RF front-end that is capable of recording Intermediate Frequency (IF) data – that is the digitized down-converted signal from the antenna – a software GNSS receiver can reprocess the same data many times over using different operating parameters. This greatly improves the ability to compare and analyze the impact of using different signal acquisition strategies, tracking parameters, receiver architectures, and so on. Such flexibility means that a software GNSS receiver provides an ideal test bed for analyzing the operating characteristics of different GNSS receiver designs.

The software GNSS receiver used for the work presented herein is based on the GNSS Software Navigation Receiver (GSNRx™) developed by the Position Location And Navigation (PLAN) Group at the University of Calgary (O'Driscoll et al 2006). **Error! Reference source not found.** presents a high level view of the components that make up a GNSS receiver as a whole. These components are separated into processes that are performed on hardware and software. As illustrated, the RF signal from a GNSS satellite is first captured by the antenna and converted into an electrical signal which is then

amplified by a preamplifier. Following this, the signal is down converted to an intermediate frequency and then transformed from an analog signal to a digital signal for sampling. At this point in time, the digitized signal can be processed by the GSNRx^{TM} software receiver in real-time or stored for post processing at a later point in time. As shown in **Error! Reference source not found.**, a reference frequency is needed to perform the signal down conversion and sampling. The reference frequency required depends on the centre frequency of the desired signal to be tracked. A frequency synthesizer is used to generate various reference frequencies so that GNSS signals of different centre frequencies can be sampled using a common oscillator.

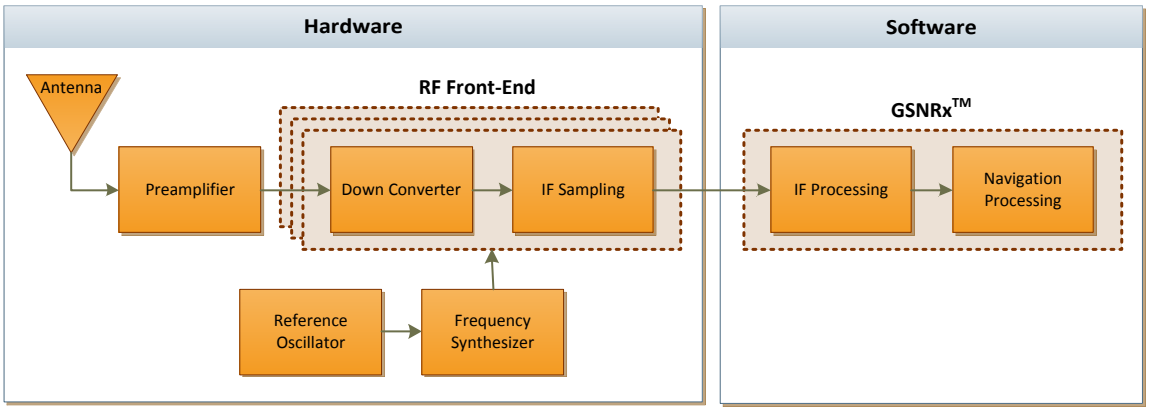

Figure 2.1: GNSS Receiver Schematic

The processes that occur within GSNRx^{TM} can be separated into two parts. IF processing components on the software receiver is responsible for acquiring and tracking the incoming GNSS signals, as well as generating pseudorange, Doppler and carrier phase measurements. The navigation processing portion of the receiver is responsible for

deriving a navigation solution based on the pseudorange, Doppler and carrier phase measurements.

2.3.1 Acquisition

Signal acquisition is the first step that software GNSS receivers must take once the incoming signal has been down converted, digitized, and sampled. Before a receiver can track a signal, it must determine whether a GNSS signal is present or not, and if so, estimate the frequency and PRN code phase of the incoming signal for a given satellite (Krumvieda et al 2001). Relative motion between the receiver and satellites in view contribute to a Doppler shift on the incoming signal. For a signal to be tracked by the receiver, a coarse estimate of the signal frequency must be within the pull-in range of the tracking loop being used. Since the pull-in range varies depending on the integration time being used, the required accuracy of the estimated signal parameters will vary depending on the type of tracking loop as well as the integration time needed to track weak signals. For a typical phase lock loop (PLL) to lock onto the incoming signal, its initial estimated frequency must be accurate to within a few tens of Hertz (Tsui 2005).

Although GPS signal acquisition algorithms may vary in the way they try to estimate the incoming signal frequency and code phase, they treat signal acquisition as a two dimensional search problem. First, a particular satellite is chosen as a search candidate; this determines which PRN code is used for acquisition. Next, a set of Doppler frequency offsets and code phase combinations are used in an attempt to generate a local replica signal that matches the Doppler frequency and code phase of the incoming signal (Van

Dierendonck 1996a). The range of the Doppler frequency offset search space is a function of the line of sight velocity between the receiver and satellite while the tracking loop pull-in range determines the frequency resolution required. In the case of a static receiver, the conventional Doppler frequency offset and code phase search space used to acquire a GPS L1 C/A signal are respectively, ± 5 kHz with a 666 Hz spacing, and 1023 chips with a 0.5 chip spacing (Tsui 2005).

Using the available frequency offset and code phase combinations, if a match exists between the incoming and locally generated signal, a correlation peak will be observed as in the example shown in Figure 2.2. The amplitude of the correlation peak allows a receiver to determine if a signal for the given PRN is present. If the amplitude exceeds a predetermined threshold, the satellite is considered to be available. Once a signal is detected, the Doppler frequency offset and code phase combination that produced the correlation peak provides a coarse estimate of the incoming signal frequency and code phase (Krumvieda et al 2001). Some of the more sophisticated acquisition algorithms take advantage of the computational efficiency afforded by using a Fast Fourier Transform (FFT) algorithm to perform the same correlation functions described above (Ma et al 2011).

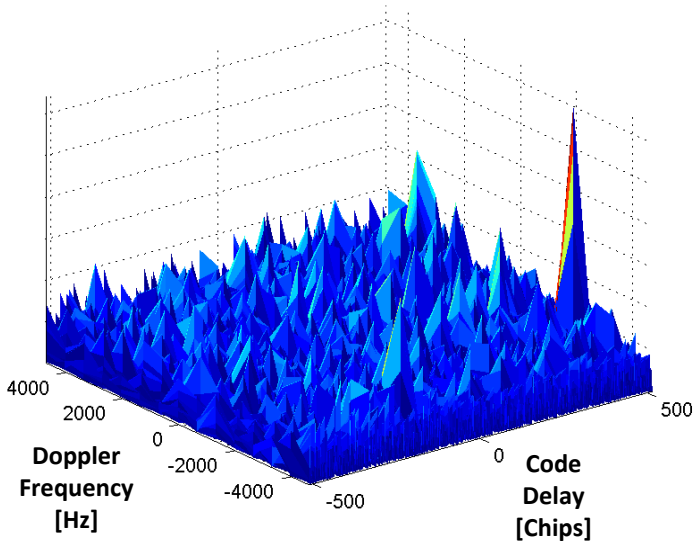

Figure 2.2: Correlator Outputs

2.3.2 Tracking

Upon the acquisition of an available signal, tracking can begin. Signal tracking allows a GNSS receiver to continuously estimate the incoming signal frequency, code phase and carrier phase, among other things. This then allows the receiver to generate satellite Doppler, pseudorange, and carrier phase observations used for navigation.

2.3.3 Closed-Loop Sequential Tracking

At present, GNSS tracking algorithms primary fall into two categories, namely open-loop and closed-loop tracking. Figure 2.3 shows the processes involved in tracking a traditional GNSS signal using a closed-loop sequential tracking loop. In this form, a Numerically Controlled Oscillator (NCO) is used to generate a local replica signal based on previous estimates of the signal frequency and code phase. This local replica signal is

then cross-correlated with the incoming signal during the Doppler Removal and Correlation (DRC) process (Van Dierendonck 1996b, Petovello & Lachapelle 2006).

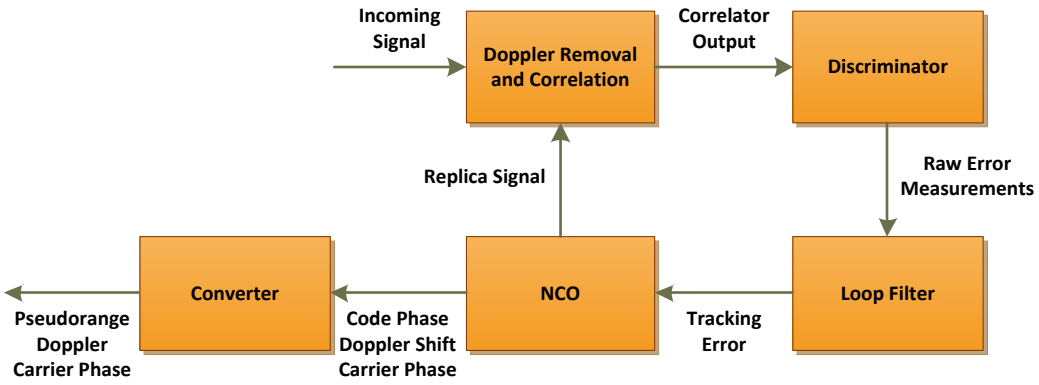

Figure 2.3: Closed-Loop Sequential Tracking Schematic

After DRC is performed on the incoming signal, the correlator outputs are used to determine the difference between the incoming and local replica signal. Correlator outputs consists of in-phase (I) and quadra-phase (Q) components as represented by equation (2.2); these I and Q components are a function of the signal amplitude A, the number of accumulated samples N, the error in the local code phase $\delta\tau$, the error in the local frequency δf, the averaged local carrier phase error $\overline{\delta\varphi}$ integrated over the period T, and the correlator offset Δ between the prompt, and early/late correlators (Petovello & Lachapelle 2006).

$$I = A \cdot N \cdot R(\delta\tau - \Delta) \cdot \frac{\sin(\pi \cdot \delta f \cdot T)}{\pi \cdot \delta f \cdot T} \cdot \cos(\overline{\delta\varphi})$$
$$Q = A \cdot N \cdot R(\delta\tau - \Delta) \cdot \frac{\sin(\pi \cdot \delta f \cdot T)}{\pi \cdot \delta f \cdot T} \cdot \sin(\overline{\delta\varphi}) \quad (2.2)$$

On a traditional tracking loop, Delay Lock Loop (DLL), Frequency Lock Loop (FLL) and Phase Lock Loop (PLL) discriminators are used to determine the code phase, frequency and carrier phase differences between the two signals (Ward et al 2006). These raw error measurements are then fed into a loop filter whereby the signal is smoothed using an integrate-and-dump process. The primary role of the loop filter is to reduce the noise in the discriminator outputs. For estimator-based tracking algorithms, a Kalman Filter is used to perform the role of the discriminator and/or the loop filter (Psiaki 2001, Psiaki & Jung 2002, Petovello & Lachapelle 2006, Lin et al 2011).

One of the primary benefits of using a closed-loop sequential processing is that this approach, compared to open-loop algorithms, is much more computationally efficient. This is especially true when a high resolution estimate of the signal parameters is desired (van Graas et al 2005). However, the drawback of using a closed-loop approach for signal tracking is that the NCO must make constant adjustments to the frequency, code phase and carrier phase of the local replica signal so that it matches the incoming signal as closely as possible. If the code phase, frequency or carrier phase error between the local replica and incoming signal is too large a loss of lock will occur (Ward et al 2006).

2.3.4 Open-Loop Block Processing

Open-loop tracking algorithms operate in a manner similar to the closed-loop algorithms in that an NCO is used to generate the local replica signal which is then correlated with the incoming signal. What differs is that, instead of generating a single replica signal, a batch of replica signals with differing frequency offsets are fed to a large bank of correlators. Correspondingly, a two dimensional array of correlator outputs are generated for a wide range of code phase and frequency offset combinations; this is similar to the array of correlator outputs generated during the signal acquisition process as illustrated in Figure 2.2. Moreover, similar to the signal acquisition process, a batch estimator uses the correlator outputs to identify the frequency offset and code phase combination that generates the largest correlation peak. Thus, the Doppler and pseudorange measurement is then generated based on frequency offset and code phase combination that provides the largest correlation peak within the array of correlation outputs (van Graas et al 2005). This process for an open-loop batch processing algorithm is shown in Figure 2.4.

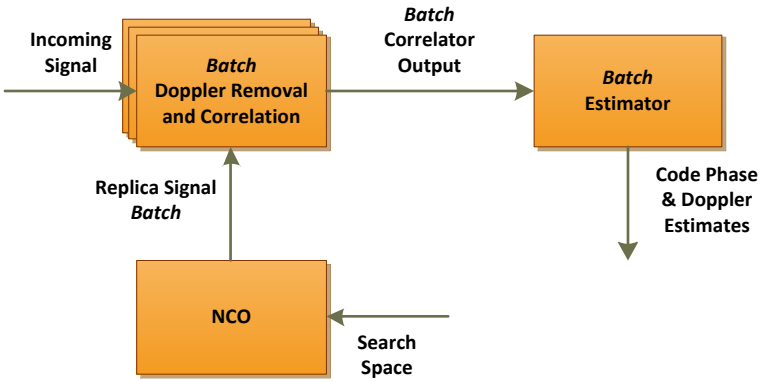

Figure 2.4: Open-Loop Block Processing Schematic

The open-loop approach has both benefits and drawbacks compared to tradition closed-loop tracking. The primary benefit of open-loop tracking is that the receiver never loses lock on the incoming signal since the NCO does not need to be fully synchronized to the incoming signal and is considered to be more robust compared to closed-loop tracking (Lin et al 2011, van Graas et al 2005). However, a major drawback of employing open-loop block processing is that this approach requires significantly more computational power while performing high-precision, wide-bandwidth signal tracking as compared to a sequential, closed-loop tracking receiver architecture (van Graas et al 2005).

2.3.5 Scalar Tracking

As mentioned in the previous sections, GNSS signal tracking algorithms can be classified into open and closed-loop algorithms. In such a classification scheme, it is often assumed that the tracking algorithms operate on a signal-by-signal basis. In other words, each

signal is tracked by the receiver on a channel-by-channel basis whereby the tracking loops for each signal operates independently from each other. As shown in Figure 2.5, this form of receiver architecture is often referred to as scalar tracking.

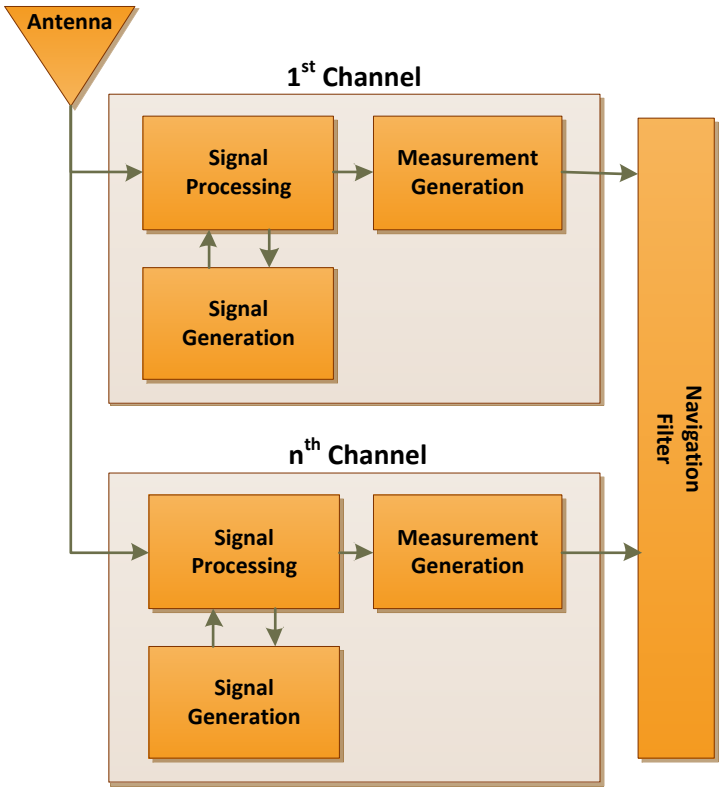

Figure 2.5: Scalar Tracking Receiver Architecture

The primary benefit of this receiver architecture is its simplicity in design since identical tracking loops can be replicated within the receiver and no communication is required between channels. On the other hand, because each channel operates completely independently from each other, information is not shared between the channels.

Moreover, signal dynamics due to receiver motion and clock errors cannot be modelled and accounted for within the scalar tracking loops (Petovello & Lachapelle 2006). Also, when a tracking channel momentarily loses lock on a signal due to line-of-sight obstructions, the receiver channel must return to a signal acquisition mode in order to reacquire the signal (Pany & Eissfeller 2006).

2.3.6 Vector-Based Tracking

To overcome some of the limitations of scalar tracking, vector-based tracking algorithms attempt to take account of the line-of-sight signal dynamics caused by the motion of a GNSS receiver. In the context of closed-loop sequential vector-based tracking as shown in Figure 2.6, the NCO is driven, not by the tracking loop as shown in Figure 2.3, but by the navigation filter. To do this, DRC is performed on the incoming signal in the same way as scalar tracking. Also, the tracking error between the incoming and local replica signal are used to estimate the code phase, frequency and carrier phase of the incoming signal; in turn, these signal parameters are used to generate the pseudorange, Doppler and carrier phase measurements for the navigation filter. In contrast to a scalar receiver however, the estimated incoming signal parameters are not used to drive the NCO on a vector-based receiver. Instead, estimates of the receiver position, velocity and clock errors from the navigation filter are combined with the satellite position, velocity and clock model to generate the local replica for a direct line-of-sight signal.

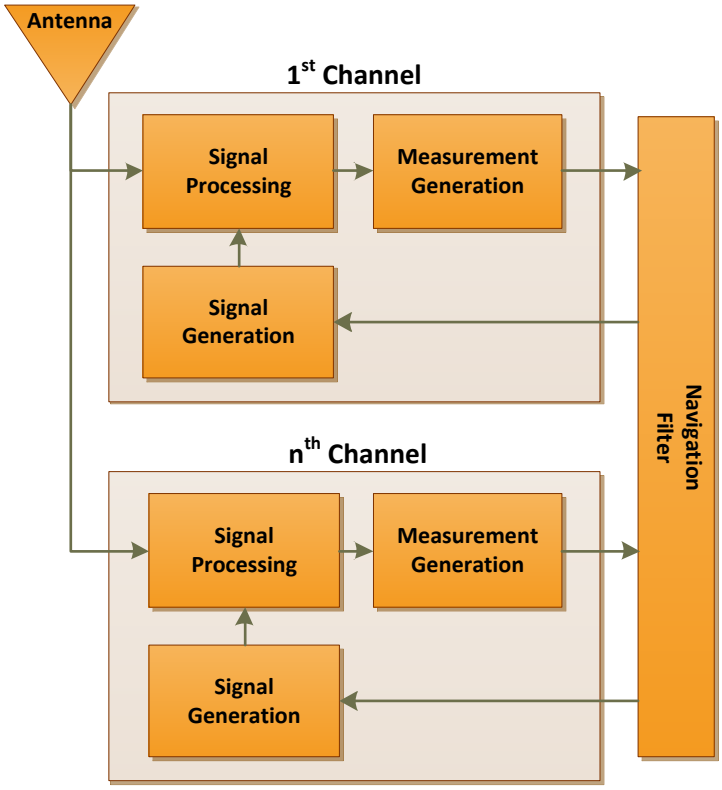

Figure 2.6: Vector-Based Tracking Receiver Architecture

There are several benefits of the vector-based tracking approach; these benefits include:

- 3-6dB improvement in interference and jamming mitigation (Benson 2007)
- Increased signal tracking sensitivity to below 10 dB-Hz (Pany & Eissfeller 2006)
- Ability to bridge signal outages without the need for signal reacquisition (Pany & Eissfeller 2006)
- Ability to minimize the effects of signal dynamic stress caused by receiver motion (Hamm & Bevly 2005)

The primary drawback of vector-based tracking algorithm is their requirement for a sufficiently accurate navigation solution since it is required by the NCO to generate the local replica signal. In the absence of an accurate navigation solution, the signal correlation process will breakdown due to gross mismatches between the incoming and local replica signal (Pany & Eissfeller 2006). This prerequisite places several key demands from the navigation solution. First, the navigation solution must have a sufficiently high update rate that allows it to detect changes in receiver motion; otherwise, any undetected receiver motion will manifest itself as line-of-sight signal dynamic stress between the receiver and satellites.

Second, because the local replica signal generated by a vector-based receiver needs to match that of the incoming signal, any error in the estimated receiver position and clock bias will manifest itself as a code phase prediction error. Likewise, errors in the estimated velocity and clock drift will also manifest itself as a Doppler prediction error. With this in mind, it is important to note that although a vector-based receiver is capable of tracking very weak signals, the resulting code phase and Doppler measurements from these very weak signals may be prone to large errors. Any undetected blunder observations that are not rejected by the navigation filter may inject gross errors into the navigation solution, thereby reducing the signal tracking performance of the vector-based receiver. It is also important to emphasize the fact that, unlike scalar tracking where errors in local signal generation only impacts a single channel, navigation errors on a vector-based receiver have the potential to negatively impact signal tracking on all receiver channels. Since, the rejection of poor pseudorange and Doppler measurements by the navigation filter is of

utmost importance for a vector-based receiver, observation pre-filtering, blunder detection, and navigation filter tuning are all critical to the performance of a vector-based GNSS receiver (Pany & Eissfeller 2006).

2.3.7 Position Determination

For the results presented in this dissertation, two methods for determining the position of a GNSS receiver are used – namely, least squares adjustment and extended Kalman filtering. The two methods have similar requirements in that they require ranging information in the form of a range between two UWB radios or a pseudorange between a GNSS satellite and a receiver. The primary difference between the two methods is that a parametric least squares adjustment does not take into account information from prior epochs while estimating the states – for example, the receiver position, velocity, and clock terms. On the other hand, an extended Kalman filter incorporates both deterministic and stochastic information from previously estimated states and combines this with new estimates based on an updated set of observations.

In both methods, the following system models are used for the pseudorange and Doppler observations as shown in equations (2.3). Here, ρ and $\dot{\rho}$ are the geometric range and range rate between the receiver r and satellite s; E, N and U represent the easting, northing and up components in the local level frame from the estimated receiver position, $\dot{E}$, $\dot{N}$ and $\dot{U}$ are the easting, northing and up velocity components in the local level frame. Lastly, c is the speed of light, while dT_r and $d\dot{T}_r$ represent the receiver clock

offset and drift with respect to the GPS time system; when multiplied the product of cdT and $c\dot{dT}$ are expressed in units of metres and metres per second, respectively.

$$\begin{aligned}
&\rho_r^s = \sqrt{(E^s - E_r)^2 + (N^s - N_r)^2 + (U^s - U_r)^2} + cdT_r \\
&\rho_r^s = f(E_r, N_r, U_r, dT_r) \\
&\\
&\dot{\rho}_r^s = \sqrt{(\dot{E}^s - \dot{E}_r)^2 + (\dot{N}^s - \dot{N}_r)^2 + (\dot{U}^s - \dot{U}_r)^2} + c\dot{dT}_r \\
&\dot{\rho}_r^s = f(\dot{E}_r, \dot{N}_r, \dot{U}_r d\dot{T}_r)
\end{aligned} \tag{2.3}$$

Likewise, an approximate pseudorange $\hat{\rho}_r^s$ and pseudorange rate $\hat{\dot{\rho}}_r^s$ can be expressed using the approximate receiver position $(\hat{E}_r, \hat{N}_r, \hat{U}_r)$, velocity $(\hat{\dot{E}}_r, \hat{\dot{N}}_r, \hat{\dot{U}}_r)$, and clock terms $(d\hat{T}_r, d\hat{\dot{T}}_r)$ as shown in equations (2.4).

$$\begin{aligned}
&\hat{\rho}_r^s = \sqrt{(E^s - \hat{E}_r)^2 + (N^s - \hat{N}_r)^2 + (U^s - \hat{U}_r)^2} + cd\hat{T}_r \\
&\hat{\rho}_r^s = f(\hat{E}_r, \hat{N}_r, \hat{U}_r, d\hat{T}_r) \\
&\\
&\hat{\dot{\rho}}_r^s = \sqrt{(\dot{E}^s - \hat{\dot{E}}_r)^2 + (\dot{N}^s - \hat{\dot{N}}_r)^2 + (\dot{U}^s - \hat{\dot{U}}_r)^2} + cd\hat{\dot{T}}_r \\
&\hat{\dot{\rho}}_r^s = f(\hat{\dot{E}}_r, \hat{\dot{N}}_r, \hat{\dot{U}}_r d\hat{\dot{T}}_r)
\end{aligned} \tag{2.4}$$

In order to solve for the states in equations (2.3), the non-linear equations are first rearranged in the form

$$
\begin{aligned}
E_r &= \hat{E}_r + \Delta E_r & \dot{E}_r &= \hat{\dot{E}}_r + \Delta \dot{E}_r \\
N_r &= \hat{N}_r + \Delta N_r & \dot{N}_r &= \hat{\dot{N}}_r + \Delta \dot{N}_r \\
U_r &= \hat{U}_r + \Delta U_r & \dot{U}_r &= \hat{\dot{U}}_r + \Delta \dot{U}_r \\
dT_r &= d\hat{T}_r + \Delta cdT_r & d\dot{T}_r &= d\hat{\dot{T}}_r + \Delta cd\dot{T}_r
\end{aligned}
\tag{2.5}
$$

where the Δ terms represent the difference between the observed position, velocity and clock terms, and the initial point of expansion – the approximate receiver position, velocity, clock bias and drift. From this, equations (2.3) can be express as:

$$
\begin{aligned}
f(E_r, N_r, U_r, cdT_r) &= f(\hat{E}_r + \Delta E_r, \hat{N}_r + \Delta N_r, \hat{U}_r + \Delta U_r, cd\hat{T}_r + \Delta cdT_r) \\
f(\dot{E}_r, \dot{N}_r, \dot{U}_r, cd\dot{T}_r) &= f(\hat{\dot{E}}_r + \Delta \dot{E}_r, \hat{\dot{N}}_r + \Delta \dot{N}_r, \hat{\dot{U}}_r + \Delta \dot{U}_r, cd\hat{\dot{T}}_r + \Delta cd\dot{T}_r)
\end{aligned}
\tag{2.6}
$$

using a first-order Taylor series expansion, equations (2.6) take on the form

$$
\begin{aligned}
f(E_r, N_r, U_r, cdT_r) = f(\hat{E}_r, \hat{N}_r, \hat{U}_r, cd\hat{T}_r) & \\
+ \frac{\partial f(\hat{E}_r, \hat{N}_r, \hat{U}_r, cd\hat{T}_r)}{\partial \hat{E}_r} \Delta E_r & \\
+ \frac{\partial f(\hat{E}_r, \hat{N}_r, \hat{U}_r, cd\hat{T}_r)}{\partial \hat{N}_r} \Delta N_r & \\
+ \frac{\partial f(\hat{E}_r, \hat{N}_r, \hat{U}_r, cd\hat{T}_r)}{\partial \hat{U}_r} \Delta U_r & \\
+ \frac{\partial f(\hat{E}_r, \hat{N}_r, \hat{U}_r, cd\hat{T}_r)}{\partial cd\hat{T}_r} \Delta cdT_r &
\end{aligned}
\tag{2.7}
$$

and

$$
\begin{aligned}
f(\dot{E}_r,\dot{N}_r,\dot{U}_r cd\dot{T}_r) = f(\hat{\dot{E}}_r,\hat{\dot{N}}_r,\hat{\dot{U}}_r,cd\hat{\dot{T}}_r) \\
+\frac{\partial f(\hat{\dot{E}}_r,\hat{\dot{N}}_r,\hat{\dot{U}}_r,cd\hat{\dot{T}}_r)}{\partial\hat{\dot{E}}_r}\Delta\dot{E}_r \\
+\frac{\partial f(\hat{\dot{E}}_r,\hat{\dot{N}}_r,\hat{\dot{U}}_r,cd\hat{\dot{T}}_r)}{\partial\hat{\dot{N}}_r}\Delta\dot{N}_r \\
+\frac{\partial f(\hat{\dot{E}}_r,\hat{\dot{N}}_r,\hat{\dot{U}}_r,cd\hat{\dot{T}}_r)}{\partial\hat{\dot{U}}_r}\Delta\dot{U}_r \\
+\frac{\partial f(\hat{\dot{E}}_r,\hat{\dot{N}}_r,\hat{\dot{U}}_r,cd\hat{\dot{T}}_r)}{\partial cd\hat{\dot{T}}_r}\Delta cd\dot{T}_r
\end{aligned}
\tag{2.8}
$$

where the first-order partial derivatives are

$$
\begin{aligned}
&\frac{\partial f(\hat{E}_r,\hat{N}_r,\hat{U}_r,cd\hat{T}_r)}{\partial\hat{E}_r} = -\frac{E^s-\hat{E}_r}{\hat{R}_r^s} \qquad \frac{\partial f(\hat{\dot{E}}_r,\hat{\dot{N}}_r,\hat{\dot{U}}_r,cd\hat{\dot{T}}_r)}{\partial\hat{\dot{E}}_r} = -\frac{\dot{E}^s-\hat{\dot{E}}_r}{\hat{\dot{R}}_r^s} \\
&\frac{\partial f(\hat{E}_r,\hat{N}_r,\hat{U}_r,cd\hat{T}_r)}{\partial\hat{N}_r} = -\frac{N^s-\hat{N}_r}{\hat{R}_r^s} \qquad \frac{\partial f(\hat{\dot{E}}_r,\hat{\dot{N}}_r,\hat{\dot{U}}_r,cd\hat{\dot{T}}_r)}{\partial\hat{\dot{N}}_r} = -\frac{\dot{N}^s-\hat{\dot{N}}_r}{\hat{\dot{R}}_r^s} \\
&\frac{\partial f(\hat{E}_r,\hat{N}_r,\hat{U}_r,cd\hat{T}_r)}{\partial\hat{U}_r} = -\frac{U^s-\hat{U}_r}{\hat{R}_r^s} \qquad \frac{\partial f(\hat{\dot{E}}_r,\hat{\dot{N}}_r,\hat{\dot{U}}_r,cd\hat{\dot{T}}_r)}{\partial\hat{\dot{U}}_r} = -\frac{\dot{U}^s-\hat{\dot{U}}_r}{\hat{\dot{R}}_r^s} \\
&\frac{\partial f(\hat{E}_r,\hat{N}_r,\hat{U}_r,cd\hat{T}_r)}{\partial cd\hat{T}_r} = 1 \qquad \frac{\partial f(\hat{\dot{E}}_r,\hat{\dot{N}}_r,\hat{\dot{U}}_r,cd\hat{\dot{T}}_r)}{\partial cd\hat{\dot{T}}_r} = 1
\end{aligned}
\tag{2.9}
$$

and

$$\hat{R}_r^s = \sqrt{(E^s - \hat{E}_r)^2 + (N^s - \hat{N}_r)^2 + (U^s - \hat{U}_r)^2}$$
$$\dot{\hat{R}}_r^s = \sqrt{(\dot{E}^s - \dot{\hat{E}}_r)^2 + (\dot{N}^s - \dot{\hat{N}}_r)^2 + (\dot{U}^s - \dot{\hat{U}}_r)^2} \quad (2.10)$$

Based on Figure 2.7, it is possible to see that the following expressions relate the Cartesian and curvilinear coordinates in the local level frame

$$R_r^s = \sqrt{\Delta E^2 + \Delta N^2 + \Delta U^2}$$
$$R_{Hz} = \sqrt{\Delta E^2 + \Delta N^2} = R_r^s \cos(\varepsilon)$$
$$\Delta E = R_{Hz} \sin(\alpha) \quad (2.11)$$
$$\Delta N = R_{Hz} \cos(\alpha)$$
$$\Delta U = R_r^s \sin(\varepsilon)$$

where ΔE, ΔN, and ΔU are the easting, northing and vertical distance between the receiver and satellite, R_{Hz} is the horizontal distance between the receiver and satellite in the local level frame, α is the azimuth angle and ε is the elevation angle from the receiver to the satellite.

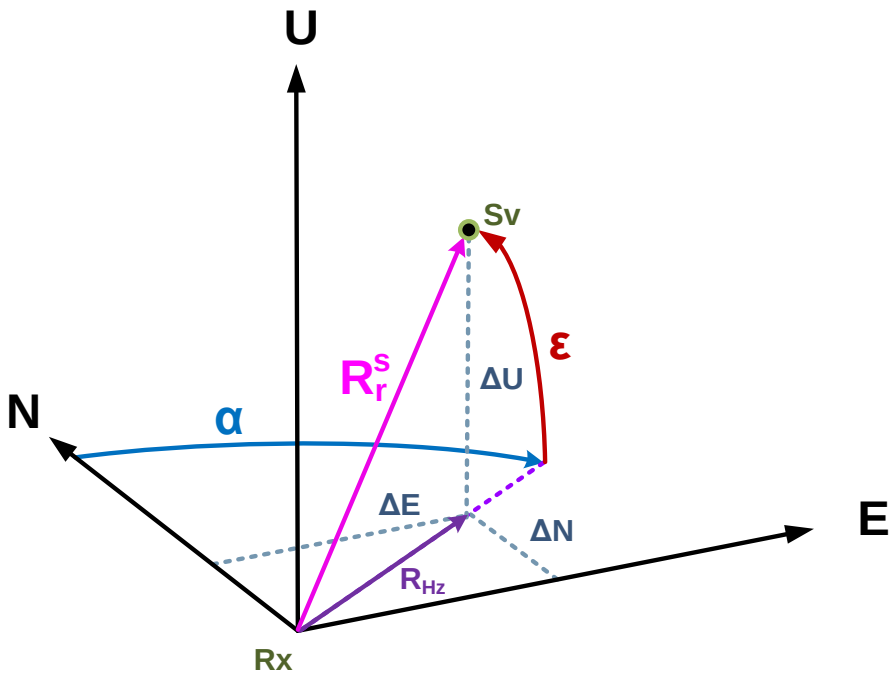

Figure 2.7: Receiver-to-Satellite Vector

Substituting the expressions from (2.11) into the partial derivatives in (2.9) allows the partial derivatives to be expressed as a function of α and ε as shown in (2.12).

$$\begin{aligned}
&\frac{\partial f(\hat{E}_r,\hat{N}_r,\hat{U}_r,cd\hat{T}_r)}{\partial \hat{E}_r} = -\cos(\alpha)\cos(\varepsilon)\\
&\frac{\partial f(\hat{E}_r,\hat{N}_r,\hat{U}_r,cd\hat{T}_r)}{\partial \hat{N}_r} = -\sin(\alpha)\cos(\varepsilon)\\
&\frac{\partial f(\hat{E}_r,\hat{N}_r,\hat{U}_r,cd\hat{T}_r)}{\partial \hat{U}_r} = -\sin(\varepsilon)\\
&\frac{\partial f(\hat{E}_r,\hat{N}_r,\hat{U}_r,cd\hat{T}_r)}{\partial cd\hat{T}_r} = 1
\end{aligned}$$

$$\begin{aligned}
&\frac{\partial f(\dot{\hat{E}}_r,\dot{\hat{N}}_r,\dot{\hat{U}}_r,cd\dot{\hat{T}}_r)}{\partial \dot{\hat{E}}_r} = -\cos(\alpha)\cos(\varepsilon)\\
&\frac{\partial f(\dot{\hat{E}}_r,\dot{\hat{N}}_r,\dot{\hat{U}}_r,cd\dot{\hat{T}}_r)}{\partial \dot{\hat{N}}_r} = -\sin(\alpha)\cos(\varepsilon)\\
&\frac{\partial f(\dot{\hat{E}}_r,\dot{\hat{N}}_r,\dot{\hat{U}}_r,cd\dot{\hat{T}}_r)}{\partial \dot{\hat{U}}_r} = -\sin(\varepsilon)\\
&\frac{\partial f(\dot{\hat{E}}_r,\dot{\hat{N}}_r,\dot{\hat{U}}_r,cd\dot{\hat{T}}_r)}{\partial cd\dot{\hat{T}}_r} = 1
\end{aligned} \qquad (2.12)$$

Substituting the partial derivatives from (2.12) into equations (2.7) and (2.8), the pseudorange and Doppler misclosure, representing the difference between the actual and estimated observations, is given below.

$$
\begin{aligned}
&f(E_r, N_r, U_r, cdT_r) - f(\hat{E}_r, \hat{N}_r, \hat{U}_r, cd\hat{T}_r) \approx \rho_r^s - \hat{\rho}_r^s \approx \delta\rho_r^s \\
&\delta\rho_r^s \approx -\cos(\alpha)\cos(\varepsilon)\Delta E_r - \sin(\alpha)\cos(\varepsilon)\Delta N_r - \sin(\varepsilon)\Delta U_r + \Delta cdT_r \\
&f(\dot{E}_r, \dot{N}_r, \dot{U}_r, cd\dot{T}_r) - f(\hat{\dot{E}}_r, \hat{\dot{N}}_r, \hat{\dot{U}}_r, cd\hat{\dot{T}}_r) \approx \dot{\rho}_r^s - \hat{\dot{\rho}}_r^s \approx \delta\dot{\rho}_r^s \\
&\delta\dot{\rho}_r^s \approx -\cos(\alpha)\cos(\varepsilon)\Delta \dot{E}_r - \sin(\alpha)\cos(\varepsilon)\Delta \dot{N}_r - \sin(\varepsilon)\Delta \dot{U}_r + \Delta cd\dot{T}_r
\end{aligned}
\tag{2.13}
$$

and further simplified to

$$
\begin{aligned}
&\delta\rho_r^s \approx a_{r,E}^s \Delta E_r + a_{r,N}^s \Delta N_r + a_{r,U}^s \Delta U_r + \Delta cdT_r \\
&\delta\dot{\rho}_r^s \approx a_{r,\dot{E}}^s \Delta E_r + a_{r,\dot{N}}^s \Delta N_r + a_{r,\dot{U}}^s \Delta U_r + \Delta cdT_r
\end{aligned}
\tag{2.14}
$$

where ($a_{r,E}^s$, $a_{r,N}^s$, $a_{r,U}^s$) and ($a_{r,\dot{E}}^s$, $a_{r,\dot{N}}^s$, $a_{r,\dot{U}}^s$) are the direction cosine vector components from receiver r to satellite s in the east, north, and up direction, respectively. From this, equations (2.14), can be written in a matrix form as shown

$$\begin{bmatrix} \delta\rho_r^1 \\ \vdots \\ \delta\rho_r^n \end{bmatrix} = \begin{bmatrix} a_{r,E}^1 & a_{r,N}^1 & a_{r,U}^1 & 1 \\ \vdots & \vdots & \vdots & \vdots \\ a_{r,E}^n & a_{r,N}^n & a_{r,U}^n & 1 \end{bmatrix} \begin{bmatrix} \Delta E \\ \Delta N \\ \Delta U \\ \Delta cdT \end{bmatrix}$$

$$\delta\rho_r = H_\rho \Delta x_\rho$$

$$\begin{bmatrix} \delta\dot{\rho}_r^1 \\ \vdots \\ \delta\dot{\rho}_r^n \end{bmatrix} = \begin{bmatrix} a_{r,\dot{E}}^1 & a_{r,\dot{N}}^1 & a_{r,\dot{U}}^1 & 1 \\ \vdots & \vdots & \vdots & \vdots \\ a_{r,\dot{E}}^n & a_{r,\dot{N}}^n & a_{r,\dot{U}}^n & 1 \end{bmatrix} \begin{bmatrix} \Delta\dot{E} \\ \Delta\dot{N} \\ \Delta\dot{U} \\ \Delta cd\dot{T} \end{bmatrix} \quad (2.15)$$

$$\delta\dot{\rho}_r = H_{\dot{\rho}} \Delta x_{\dot{\rho}}$$

where $\delta\rho_r$ is the misclosure vector for the observed and estimated pseudorange observations, H_ρ is the design matrix for the pseudorange observations, Δx_ρ is the difference between the estimated and approximated position and clock offset states, $\delta\dot{\rho}_r$ is the misclosure vector for the observed and estimated Doppler observations, $H_{\dot{\rho}}$ is the design matrix for the Doppler observations, and $\Delta x_{\dot{\rho}}$ is the difference between the estimated and approximated velocity and clock drift states. To solve for the difference between the estimated and approximated states, an iterative parametric least squares adjustment or extended Kalman filter can be used. This is shown in sections 2.3.7.1 and 2.3.7.2 respectively.

2.3.7.1 Least Squares Adjustment

Using a parametric least squares adjustment, Δx_{ρ} and $\Delta x_{\dot{\rho}}$ can be solved by

$$\Delta\hat{x}_{\rho} = (H^T RH)^{-1} H^T R\delta\rho_r$$
$$\Delta\hat{x}_{\dot{\rho}} = (H^T RH)^{-1} H^T R\delta\dot{\rho}_r \tag{2.16}$$

where $\Delta\hat{x}_{\rho}$ and $\Delta\hat{x}_{\dot{\rho}}$ are the estimated difference in position, velocity and clock state from the initial point of expansion, and R is the observation weight matrix (Hegarty 2006). Adding $\Delta\hat{x}_{\rho}$ and $\Delta\hat{x}_{\dot{\rho}}$ to the initial point of expansion results in an updated estimate of the position velocity and time. After iterating the least squares adjustment until convergence has been reached, the final position and clock terms become the best estimate for the navigation solution.

2.3.7.2 Extended Kalman Filter

Besides using a parametric least squares adjustment to obtain a navigation solution from GNSS observations, an extended Kalman filter (EKF) can also be used. In contrast to the a least squares adjustment which generates a unique solution only when the number of linearly independent observations are equal to or more than the number of states, an EKF is capable of updating its navigation solution even when the number of observations are less than the number of unknowns. To do this, the EKF takes information based on previous estimates and tries to predict the states ahead using a dynamics model. Once a prediction has been made, information from new observations is used to update the

predicted states. This prediction and update process is shown with greater detail in Figure 2.8 (symbols used are described in the following paragraph).

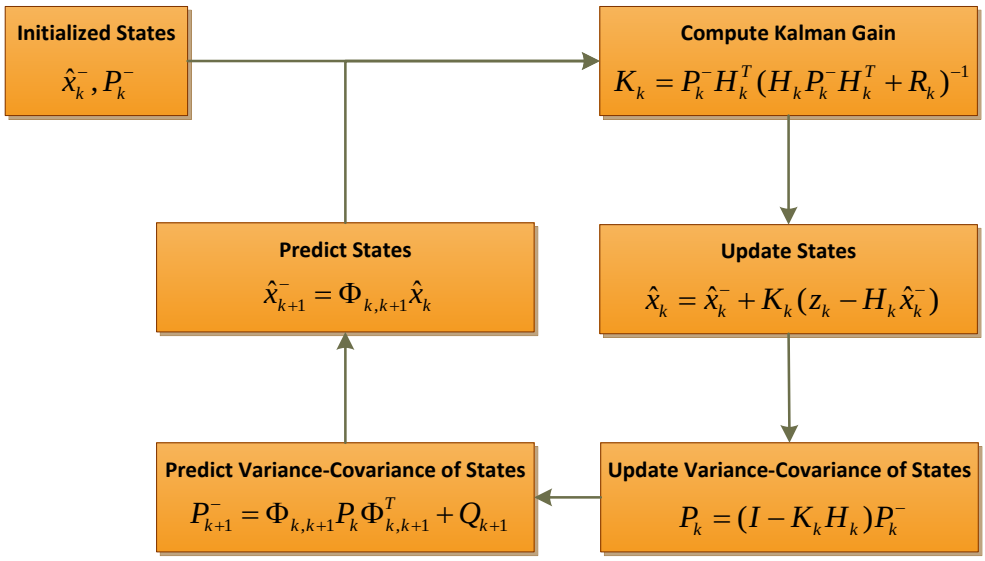

Figure 2.8: Kalman Filter Predict and Update Loop

In Figure 2.8, the predicted state vector and state variance-covariance matrix are denoted with a superscript "-", subscript k denotes the current epoch while $k+1$ denotes the next epoch. Within the Kalman filter, the state vector $\hat{x}^-$ can be either predicted based on information from a previous epoch or be initialized from a least squares solution – in this case, $\hat{x}_k$ and P_k from the initial least squares solution take the place of $\hat{x}_k^-$ and P_k^-. Once the states and their variance-covariance information are available, a Kalman gain matrix K_k is used to determine how much weight should be placed on the information from the predicted states versus the information provided by a new set of observations, z_k.

To compute the Kalman gain matrix, the design matrix H_k used is the same as that used in a least squares solution and is given in equation (2.15). The weighting of information from the predicted states and the new observations is based on the uncertainty of the predicted states given in P_k^-, and the variance of the incoming observations R_k. The design matrix H_k acts as a mapping matrix that enables elements in the state space to be mapped into the observation or measurement space, and vice versa. The observation covariance matrix used for the GNSS satellite observations are given by

$$R = \sigma_o^2 \begin{bmatrix} \frac{1}{\sin(\varepsilon^1)} & 0 & 0 \\ 0 & \ddots & 0 \\ 0 & 0 & \frac{1}{\sin(\varepsilon^n)} \end{bmatrix} \tag{2.17}$$

where σ_o^2 is the variance of the satellite observation at zenith, and ε^n is the elevation angle of the nth satellite. Note that the value of σ_o^2 varies based on the associated observation type such as pseudorange and Doppler observations.

After the Kalman gain matrix is computed, the state vector and its variance-covariance matrix are updated using the observation vector z_k. It is important to note that since the system is non-linear, a first order Taylor-series is used to solve for the *differences* between the approximate and observed position, velocity and clock terms rather than the actual terms themselves. Thus, the observation vector consists of the differences between

the predicted satellite measurements, generated using the approximate receiver position, velocity and clock terms, and the observed satellite measurements.

Following this, the state vector $\hat{x}_k$ and the variance-covariance matrix P_k provides the navigation solution for epoch k, and can be predicted forward for a new epoch using the transition matrix $\Phi_{k,k+1}$ shown in equation (2.18). Note that the dynamics model used here is a constant velocity model where the position states are assumed to be

$$\begin{bmatrix} \Delta E_{k+1}^{-} \\ \Delta N_{k+1}^{-} \\ \Delta U_{k+1}^{-} \\ \Delta \dot{E}_{k+1}^{-} \\ \Delta \dot{N}_{k+1}^{-} \\ \Delta \dot{U}_{k+1}^{-} \\ \Delta cdT_{k+1}^{-} \\ \Delta cd\dot{T}_{k+1}^{-} \end{bmatrix} = \begin{bmatrix} 1 & 0 & 0 & \Delta T & 0 & 0 & 0 & 0 \\ 0 & 1 & 0 & 0 & \Delta T & 0 & 0 & 0 \\ 0 & 0 & 1 & 0 & 0 & \Delta T & 0 & 0 \\ 0 & 0 & 0 & 1 & 0 & 0 & 0 & 0 \\ 0 & 0 & 0 & 0 & 1 & 0 & 0 & 0 \\ 0 & 0 & 0 & 0 & 0 & 1 & 0 & 0 \\ 0 & 0 & 0 & 0 & 0 & 0 & 1 & \Delta T \\ 0 & 0 & 0 & 0 & 0 & 0 & 0 & 1 \end{bmatrix} \begin{bmatrix} \Delta \hat{E}_k \\ \Delta \hat{E}_k \\ \Delta \hat{U}_k \\ \Delta \hat{\dot{E}}_k \\ \Delta \hat{\dot{N}}_k \\ \Delta \hat{\dot{U}}_k \\ \Delta cd\hat{T}_k \\ \Delta cd\hat{\dot{E}}_k \end{bmatrix} \qquad (2.18)$$

$$\hat{x}_{k+1}^{-} = \Phi_{k,k+1}\hat{x}_k$$

where ΔT is the prediction interval between epoch k and $k+1$.

The process noise matrix Q_{k+1} is used to inflate the variance of the predicted state variance-covariance matrix P_k in order to account for errors introduced from the prediction of the states. The process noise model used for the state vector is a random

walk velocity model for navigation determination, and a voltage-controlled temperature compensated crystal oscillator (VCTCXO) model for the clock terms. This process noise model is shown below

$$Q = \begin{bmatrix} \frac{S_{\dot{E}}\Delta t3}{3} & 0 & 0 & \frac{S_{\dot{E}}\Delta t^2}{2} & 0 & 0 & 0 & 0 \\ 0 & \frac{S_{\dot{N}}\Delta t3}{3} & 0 & 0 & \frac{S_{\dot{N}}\Delta t}{2} & 0 & 0 & 0 \\ 0 & 0 & \frac{S_{\dot{U}}\Delta t3}{3} & 0 & 0 & \frac{S_{\dot{U}}\Delta t^2}{2} & 0 & 0 \\ \frac{S_{\dot{E}}\Delta t^2}{2} & 0 & 0 & S_{\dot{E}}\Delta t & 0 & 0 & 0 & 0 \\ 0 & \frac{S_{\dot{N}}\Delta t^2}{2} & 0 & 0 & S_{\dot{N}}\Delta t & 0 & 0 & 0 \\ 0 & 0 & \frac{S_{\dot{U}}\Delta t^2}{2} & 0 & 0 & S_{\dot{U}}\Delta t & 0 & 0 \\ 0 & 0 & 0 & 0 & 0 & 0 & q_{11} & q_{12} \\ 0 & 0 & 0 & 0 & 0 & 0 & q_{12} & q_{22} \end{bmatrix} \quad (2.19)$$

where $S_{\dot{E}}$, $S_{\dot{N}}$ and $S_{\dot{U}}$ are the spectral density values for the east, north and up velocity, ΔT is the time interval in which the states are being predicted forward since the last Kalman filter update, q_{11}, q_{12}, q_{21} and q_{22} represent the elements of a VCTCXO noise model found in equation (4.10). For the results presented in this research, the horizontal and vertical velocity spectral density value used is $1\,\mathrm{m/s^2}/\sqrt{Hz}$ and $0.5\,\mathrm{m/s^2}/\sqrt{Hz}$, respectively. These values describe the variability in velocity typical for pedestrian motion. These process noise parameters are discussed with greater detail in Chapter 4.

2.4 GNSS Error Sources

For GNSS positioning and navigation, error sources that impact the accuracy of the navigation solution can be grouped into three types: satellite errors, propagation errors, and receiver errors. With this in mind, the pseudorange measurement model is given by

$$\rho_r^s = R_r^s + \varepsilon_{orbit}^s \cdot u_r^s + \delta_{tropo}^s + \delta_{iono}^s + \delta_{multipath,r}^s + c(\delta T_{satellite}^s + \delta T_{receiver,r}) + \varepsilon_{noise,r} \qquad (2.20)$$

where ρ_r^s is the observed pseudorange between receiver r and satellite s, R_r^s is the geometric range between the receiver and satellite, $\varepsilon_{orbit}^s \cdot u_r^s$ is the absolute orbital positioning error, ε_{orbit}^s, projected onto the line-of-sight unit vector u_r^s from the receiver to the satellite, δ_{tropo}^s and δ_{iono}^s are the delay caused by the troposphere and ionosphere $\delta_{multipath,r}^s$ is multipath delay, c is the speed of light, $\delta T_{satellite}^s$ and $\delta T_{receiver,r}$ are the satellite and receiver clock errors, and $\varepsilon_{noise,r}$ is the receiver noise (Conley et al 2006b). These error sources are discussed in the following subsections.

2.4.1 Satellite Errors

The two primary sources of satellite error are the satellite orbit position error and the satellite clock error. Satellite orbit position error is the discrepancy between the true position of the satellite and the position derived from the satellite ephemeris. In the case of the broadcast ephemeris that is provided in the navigation message from a GPS satellite, the orbit errors are typically within 1 metre within two hours of the ephemeris' time of week (IGS Products 2010). Satellite clock errors represent the time difference between the satellite's broadcasted time of week and the GNSS time system being used. A satellite clock error model is provided in the GPS satellite navigation message; however, the discrepancy between the corrected time generated from the broadcast model and the actual system time has a standard deviation of 2.5 nanoseconds (IGS Products 2010).

2.4.2 Signal Propagation Errors

GNSS signal propagation errors consists primarily of tropospheric delay, ionosphere error, and multipath error. Tropospheric delay is a function of the refractivity index of the lower atmosphere and is a function of temperature, humidity, and pressure. Troposphere error models such as the Saastamoinen and Hopfield models provide an effective means of reducing the effects of troposphere delay on GNSS signals (Misra & Enge 2006b). If left uncompensated, troposphere delay may vary between 2.4 metres and 25 metres depending on the elevation of the satellite (Conley et al 2006b).

The ionosphere in the context of GNSS positioning is considered to be the upper part of the Earth's atmosphere between 70 km and 1000 km above the Earth's surface. Due to the nature of the ionosphere's propagation properties, pseudorange code delay experienced by L-band GNSS signals are dispersive. This means that the GPS L1, L2 and L5 signals with different frequencies will experience a differing delay. In addition, this delay is also a function of the amount of free electrons along the path in which a GNSS signal must travel through to reach the receiver (Conley et al 2006b). As such, signals from low elevation satellites will experience up to three times the amount of ionospheric delay as compared to that of a satellite located near the zenith. Ionosphere models such as the Klobuchar model attempts to model the effects of the ionosphere (Misra & Enge 2006b). Left uncompensated, ionosphere errors may reach several tens of metres depending on the amount of free electrons in the ionosphere.

Multipath signals present GNSS receivers with additional challenges. Pseudorange errors from multipath signals that are reflected off nearby objects vary depending on the strength of the multipath signals, antenna type, as well as the design of the signal tracking loops within the receiver. Multipath signals that reflect off large, smooth, reflecting surfaces with a surface roughness of less than a few centimetres and uniform electrical properties will be specular (Misra & Enge 2006b). These surfaces are typical in dense urban environments and a common example is the panelling found on the side of large office buildings. On the other hand, signals that reflect off of rough, non-uniform surfaces result in diffuse multipath that have a weaker strength compared to specular multipath (Conley et al 2006a). Depending on the code phase differences between the multipath and

line-of-sight signals, either a delay or an advance in the pseudorange may result. The ranging error found in multipath corrupted pseudorange observations generated from the GPS L1 C/A code may range from 1-2 metres up to 150 metres – half the length of a C/A code chip.

Since the direction of multipath signals depend on the relative location between the satellites and the receiver, along with nearby reflectors, multipath errors may differ greatly from location to location (Ray 2000). In contrast to multipath errors, both troposphere delay and ionosphere effects are spatially correlated and GPS receivers that are located close to each other – within several kilometres – experience similar amounts of propagation delay. This property of the atmospheric effects can be exploited using differential GNSS techniques where GNSS measurements between two nearby receivers are combined to reduce the effects of troposphere and ionosphere errors and is discussed in section 2.5.

2.4.3 Receiver Errors

GNSS receiver errors primarily consist of receiver noise and hardware biases. 1σ pseudorange errors due to receiver noise in modern high-performance receivers are typically in the decimetre level and is caused by thermal noise jitter (Montenbruck 2003). Hardware biases are caused by delays caused by the GNSS signals travelling through hardware components such as the antenna, cables, RF filters, low-noise amplifiers, and mixers. Although these biases may be significant, the delay is common on all signals that pass through the same components. As a result, the common biases will appear as a

receiver clock bias that is estimated as a state within the GNSS navigation solution either by a least squares adjustment or by the Kalman filter (Conley et al 2006b).

2.5 Differential GNSS Positioning

Differential GNSS positioning makes use of observations from nearby receivers in an effort to remove systematic biases that are common between receivers, namely satellite orbital errors, troposphere delay and ionosphere effects. There are two main approaches to achieve this; the first method uses linear combinations of pseudorange measurements that are common between two nearby receivers and/or satellites. Differencing pseudorange observations between two receivers, results in the reduction of spatially correlated errors such as troposphere delays, ionosphere errors and satellite orbit errors. However, measurement errors that are uncorrelated between the receivers such as multipath, noise and receiver clock biases are amplified due to the formation of linear combinations between multiple random processes.

Linear combination for a between-receiver single differenced pseudorange observation is shown in equation (2.21).

$$\Delta\rho = \rho_2^i - \rho_1^i \tag{2.21}$$

where $\Delta\rho$ is the between-receiver single differenced pseudorange observation, ρ_1^i and ρ_2^i are the pseudorange observations of satellite i measured by the first and second receiver, respectively. Substituting equation (2.20) into equation (2.21) results in

$$\begin{aligned}\Delta\rho = &[R_2^i + \varepsilon_{orbit}^i \cdot u_2^i + \delta_{tropo,2}^i + \delta_{iono,2}^i + \delta_{multipath,2}^i + c(\delta T_{satellite}^i + \delta T_{receiver,2}) + \varepsilon_{noise,2}] \\ &-[R_1^i + \varepsilon_{orbit}^i \cdot u_1^i + \delta_{tropo,1}^i + \delta_{iono,1}^i + \delta_{multipath,1}^i + c(\delta T_{satellite}^i + \delta T_{receiver,1}) + \varepsilon_{noise,1}]\end{aligned} \tag{2.22}$$

where the superscript and subscript denotes the satellite and receiver, respectively. For receivers that are located near one another, spatially correlated errors are similar.

$$\begin{aligned}u_1^i &\approx u_2^i \\ \delta_{tropo,1}^i &\approx \delta_{tropo,2}^i \\ \delta_{iono,1}^i &\approx \delta_{iono,2}^i\end{aligned} \tag{2.23}$$

As such, equation (2.22) can be presented as follows:

$$\begin{aligned}\Delta\rho \approx &[R_2^i + \delta_{multipath,2}^i + c(\delta T_{receiver,2}) + \varepsilon_{noise,2}] \\ &-[R_1^i + \delta_{multipath,1}^i + c(\delta T_{receiver,1}) + \varepsilon_{noise,1}]\end{aligned} \tag{2.24}$$

Because multipath and receiver noise errors are considered random processes, when differenced, they have an additive effect. Therefore, equation (2.24) can be rewritten as:

$$\Delta\rho \approx \Delta R^{i}_{1\to 2} + c(\Delta\delta T_{receiver,1\to 2}) - \delta^{i}_{multipath,1} + \delta^{i}_{multipath,2} - \varepsilon_{noise,1} + \varepsilon_{noise,2} \qquad (2.25)$$

where $\Delta R^{i}_{1\to 2}$ is the difference in geometric range between the satellite i and the two receivers, and $\Delta\delta T_{receiver,1\to 2}$ is the relative receiver clock bias. From equation (2.25), it is possible to see that, by using between-receiver single differenced pseudorange observations, it is possible to either reduce or completely eliminate the satellite errors, troposphere delay, and ionosphere error. However, one of the disadvantages of using this approach is that multipath errors and receiver noise are amplified due to the linear combination of two independent random processes. Moreover, what remains of the receiver clock bias is not the absolute bias but a relative clock bias between the two receivers.

The second method for removing spatially correlated errors is through the use of GNSS corrections. In this approach, information about the measurement errors observed by a nearby GNSS receiver located at a predetermined position is used to correct incoming measurements. In situations where multiple receivers are providing corrections, the corrections may be weighted to form a network solution. However, in instances where only one receiver is available for generating corrections, the result is nearly identical to using between-receiver single differenced observations with one exception – that is, instead of estimating the relative position two receivers, an absolute position and clock bias can be attained.

2.6 Ultra-Wideband Ranging

Ranging by Ultra-Wideband (UWB) RF signals allow navigation systems to operate in environments where standard GNSS signals are either limited or unavailable. UWB ranging techniques may be used to form a stand-alone navigation system (Yan & Bellusci 2009, Ni et al 2010) or serve to augment GNSS measurements in areas where GNSS signals are either limited or unavailable (Vydhyanathan et al 2009, Chiu 2008, MacGougan & Klukas 2009, MacGougan et al 2010). The principles of using UWB signals for ranging, approaches to modelling UWB ranging errors, and the method for using UWB ranges for navigation is discussed in the following subsections.

2.6.1 Range Determination

The UWB radios used in the research presented were made by Multispectral Solutions Inc. and employ a Time Of Arrival (TOA) ranging technique. The UWB radios used can operate in two modes – a requester or responder. In the requester mode, the radio sends a polling message to a radio with a specific identifier and waits for a return message from a responder radio. In this way, the requester actively communicates with nearby radios while a responder radio operates passively – only responding when a polling message is directed at it.

Ranges between two radios are only measured by the requesting radio and not the responder; this is performed by determining the two-way time of flight taken by a polling message to travel from the requesting radio to the responder radio, and a return message to be sent back to the requesting radio (MacGougan et al 2009). It should be noted that radios operating as a responder have predetermined response times where, upon receiving

a polling message, it waits a predetermined amount of time before sending a return message. Therefore, the total time required for a polling message to be sent and a responding message to be received can be expressed as

$$\Delta T = (\Delta T_{request} + \Delta T_{response\ delay} + \Delta T_{return}) \tag{2.26}$$

where ΔT is the two-way time of flight that includes the time required for a polling message to travel from the requesting radio to the responder radio, $\Delta T_{request}$, a predetermined responds delay, $\Delta T_{response\ delay}$, and the time required for a response message to travel from the responder radio back to the requesting radio, ΔT_{return}. Based on equation (2.26), the range measurement can be expressed as follows:

$$R_{UWB} = c_{air} \cdot \left(\frac{\Delta T}{2} - \Delta T_{response\ delay} \right) \tag{2.27}$$

where R_{UWB} is the range measurement and c is the speed of light in air.

2.6.2 Range Error Modelling

Similar to GNSS measurements, UWB ranging is susceptible to propagation delays due to atmospheric delay. Since the speed of light used in the equation (2.27) is for an RF signal travelling through a vacuum, differences in atmospheric temperature, pressure and vapour pressure from the reference value used will create biases in the measured ranges.

Moreover, because range measurements are determined based on a signal's two-way time of flight, accurate measurement of time is paramount to the accuracy of the observations. In order to measure time, the UWB radios used for this research employ oscillators based on a crystal frequency standard. Since the frequency of crystal oscillators is sensitive to vibration and temperature fluctuations, changes in radio operating temperature and mechanical stress may cause time varying biases in UWB range measurements (MacGougan et al 2009).

Aside from measurement biases, UWB ranging is also susceptible to signal amplitude dependent scale factor errors. Such errors are caused by the detection method used to determine the presence of a Gaussian RF pulse in the UWB receiver. In the UWB radios used for this research, the receiver determines the presence of a signal pulse from a nearby radio based on a given signal amplitude threshold. As a sufficiently strong Gaussian pulse reaches the receiver, the amplitude of the incoming signal raises over time until a detection threshold has been exceeded and triggers a detection event; after a detection event has been triggered the amplitude of the incoming pulse continues to grow until it reaches its peak amplitude and then drop back down. Because a one-sided detection is used, weaker signals that are still sufficiently strong to trigger a detection event will take slightly longer to reach the detection threshold compared to a strong signal (MacGougan et al 2009); this timing difference caused by variations in signal strength is illustrated in Figure 2.9. Note that signals strength generally decreases as a function of the squared distance between radios due to propagation loss; because of this, ranging errors appear to vary as a function of distance. However, signal strengths can also

vary depending on the propagation medium and in instances where UWB signals must travel through denser mediums such as the walls within a building, ranging delays will also appear.

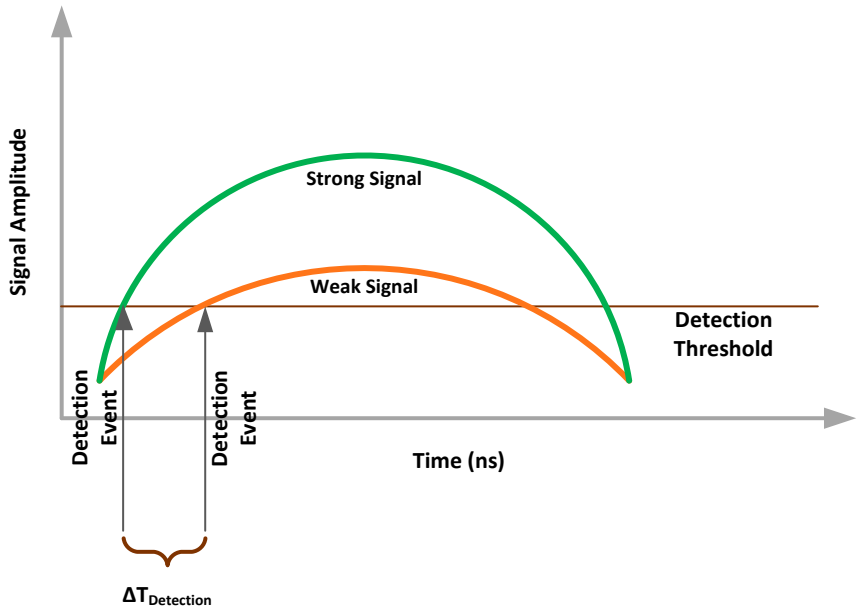

Figure 2.9: UWB Pulse Detection

One of the advantages of UWB ranging is its resistance to multipath. This is primarily due to the wide bandwidth of the UWB signal which allows for extremely short signal pulses to be sent. Because of the very short pulse duration (in the order of picoseconds), it is possible for a UWB receiver to differentiate between multipath signal reflections that arrive in at very close time intervals. GNSS signals offer similar capability in identifying multipath reflections, however, in order to clearly identify multipath reflections, the multipath error of a GNSS signal must be greater than one chip. For a GPS L1 C/A

signal, the each chip lasts 1 microsecond; as a result, only multipath reflections with a delay in excess of 300 m can be clearly identified for a GPS L1 C/A signal.

UWB range measurements are also subject to errors such as timing jitter and timing resolution. Timing jitter due to the oscillators causes noise in the resulting ranging measurements. In addition, the timing resolution of the UWB radio also affects the precision of the range measurements. Both multipath errors and timing jitter results in ranging errors that are random in nature. In the context of navigation, only the bias and scale factor errors are modelled. To mitigate these systematic errors found in UWB measurements, observed UWB ranges can be modelled as

$$R_{UWB} = S\left(R_{true} + B\right) + \varepsilon \tag{2.28}$$

where R_{UWB} is the range measured by a UWB radio pair, S is the scale factor error, R_{true} is the true geometric range between the radio pair, and ε are residual errors due to multipath and timing jitter.

2.6.3 Position Determination with UWB

The method for integrating UWB range measurements into a navigation solution for position determination is similar to that of GNSS pseudorange observations. However, UWB range measurements only consist of the geometric range between a pair of UWB radios, along with ranging errors discussed earlier; GNSS pseudorange observations on

the other hand comprise of the geometric range between a satellite and receiver as well as a receiver clock offset. As such, when UWB range observations are used, the receiver clock offset and drift is not estimated. Also, unlike GNSS signals which transmit ephemeris information that can be used to determine a satellite's position at a given point in time, the UWB radios used for this research do not provide such information. Because of this, the responding UWB radio's position must be determined by other means. One other notable difference between UWB and GNSS observations is that, unlike GNSS receivers which typically generate pseudorange measurements for all satellites tracked at regular time intervals, UWB range measurements are not synchronized with GNSS observations. Moreover, for the radios used in this research, UWB radios operating in a requesting mode can only poll one radio at a time. This means that only a single range measurement can be observed at any given epoch.

Given the operating characteristics of the UWB radios used, an initial position must be attained before an extended Kalman filter can make use of single UWB range observations for navigation. Typically, this initial position is computed using a least squares adjustment based on GNSS pseudorange observations and the resulting solution is used to initialize the extended Kalman filter. As mentioned earlier, because UWB range measurements are not synchronized with GNSS observations, asynchronous Kalman filter updates were employed whereby UWB ranges were processed as they become available independently from GNSS observations.

The observation misclosure vector, design matrix and navigation state vector for a UWB Kalman update, shown below, is similar to that found in equation (2.15).

$$\begin{bmatrix} \delta R_{a\to b} \end{bmatrix} = \begin{bmatrix} a_{a\to b,E} & a_{a\to b,N} & a_{a\to b,U} \end{bmatrix} \begin{bmatrix} \Delta E \\ \Delta N \\ \Delta U \end{bmatrix} \tag{2.29}$$

$$\delta R_{a\to b} = H_R \Delta x_R$$

where $\delta R_{a\to b}$ is the difference between the observed and estimated range, $a_{a\to b,E}$, $a_{a\to b,N}$ and $a_{a\to b,U}$ make up the direction cosine vector from radio a to radio b and form the design matrix H_R, ΔE, ΔN and ΔU is the difference between the estimated and predicted position in the state vector Δx_R. As mentioned, an extended Kalman filter was used to update the navigation filter and the structure of the extended Kalman filter used is discussed in Section 2.3.7.2.

2.7 Summary

This chapter described the concepts of GNSS and UWB positioning using estimation techniques that include least squares adjustment and Kalman filtering. In particular, the architecture of a software GNSS receiver was presented and GNSS signal tracking algorithms such as scalar and vector-based tracking was discussed. The performance of scalar and vector-based GNSS receivers in harsh indoor environments will be analyzed in the Chapter 3. The benefits of differential GNSS and UWB augmentation techniques, described in this chapter, will form the basis of Chapter 4 with an emphasis on navigation availability and accuracy. After this, the impact of using differential GNSS and UWB augmentation in a vector-based GNSS receiver is detailed in Chapter 5.

Chapter Three: Weak GNSS Signal Tracking

3.1 Overview

This chapter compares the performance of scalar and vector-based GNSS receivers in weak GNSS signal environments. The performance gains offered by a vector-based GNSS receiver can be clearly seen in the results presented in this chapter. The performance of the receiver architectures are evaluated using data collected inside a traditional North American timber-framed house. The scalar receiver performance provides a point of reference for evaluating the effectiveness of vector-based receiver architectures for indoor environments. It should be noted that the effects of differential GPS (DGPS) and Ultra-Wideband (UWB) augmentation on vector-based tracking is not covered in this chapter but will be examined in greater detail in chapters 4 and 5. The primary reason is that the use of DGPS and UWB augmentation did not provide any noticeable benefit for the vector-based GNSS receiver while operating within the timber-framed house environment presented in this chapter – even in the basement. A number of factors account for the lack of noticeable benefits in augmenting a vector-based GNSS receiver with DGPS corrections and UWB ranges; these factors include low signal attenuation of the timber structure, the ability of vector-based GNSS receiver's to maintain lock on up to 4 usable satellites while in the basement, and the lack of UWB signal penetration while the GNSS receiver was in the basement.

The following sections provide a description of the test environment and equipment setup used to evaluate the two GNSS receiver architectures followed by an analysis of the

tracking and navigation performance of the two receivers. Tracking and navigation performance metrics presented in this chapter are similar to those presented in chapters 4 and 5. These latter chapters focus on the impact of employing differential GNSS positioning and Ultra-Wideband augmentation techniques for vector-based GNSS receivers.

3.2 Weak GNSS Signal Environment Testing

Urban environments present significant challenges to traditional GNSS receivers. Natural foliage and manmade buildings often block or attenuate line-of-sight signals while reflective surfaces generate strong multipath signals. The resulting outcome often leads to large pseudorange observation errors which, in turn, result in gross navigation errors. In other instances, GNSS signals may be completely denied and a receiver may not be able to determine its position at all. Vector-based GNSS receivers seek to overcome some of the weaknesses found in traditional scalar GNSS receivers through combining information found in the receiver's navigation solution and the satellite ephemeris. By determining the relative position, velocity and clock offsets between a receiver and satellite, a line-of-sight local replica signal can be generated within the receiver irrespective of the signal dynamics on a given channel. This allows the receiver to bridge brief signal outages and increase the tracking sensitivity of weak GNSS signals. The following subsections describe the equipment setup and location used to test the performance of a standalone scalar and vector-based GNSS receiver.

3.2.1 Location and Environment

The results presented in this chapter are based on kinematic pedestrian GNSS data collected on November 30th, 2010 in a suburban area and spans both outdoor and indoor environments. The reference trajectory of the GNSS receiver is shown in light green on Figure 3.1; dark green blocks represent areas of dense vegetation, fence lines are represented in brown, and buildings are represented in magenta.

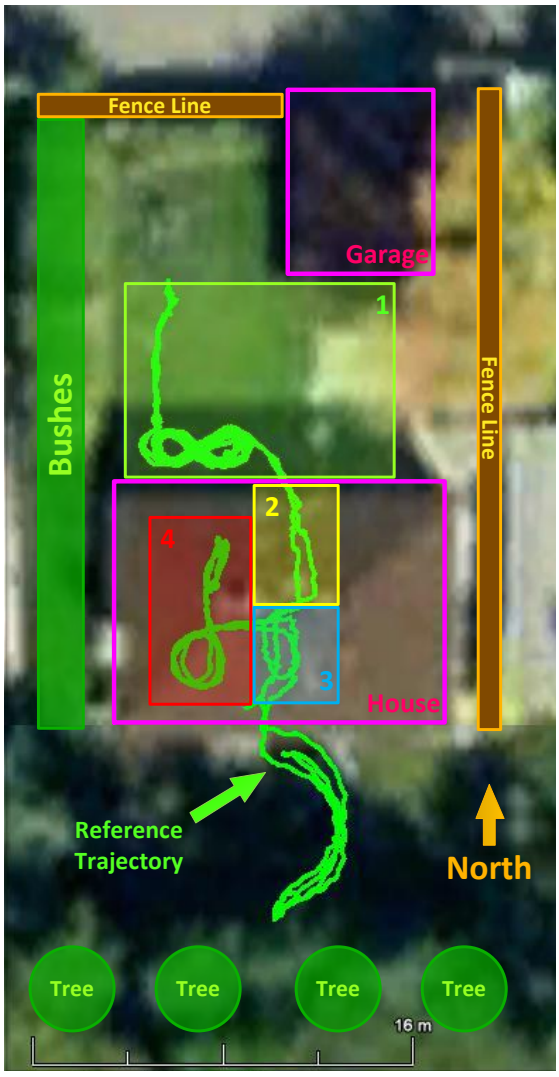

Figure 3.1: Residential Test Environment

Analysis of the dataset focuses on four key locations within a single story timber-framed house including:

1) An outdoor segment highlighted in light green in Figure 3.1
2) An indoor segment moving through the ground floor shown in yellow
3) An indoor segment transitioning from the ground floor to the basement denoted in light blue
4) An indoor segment spent in the basement represented in red

The outdoor test environment is shown on Figure 3.2 and Figure 3.3. The outside of the timber-framed house, along with the adjacent garage and backyard are clearly visible. Also shown is the open-framed backpack housing the data collection equipment (detailed in section 3.2.2).

Figure 3.2: Outdoor Environment - 1 of 2

The interior of the house's ground floor is shown in Figure 3.4. This portion of the house links the entrance from the backyard (shown on Figure 3.2) to the stairs that descend to the basement (shown on Figure 3.5). Last but not least, the basement of the house is shown on Figure 3.6.

Figure 3.3: Outdoor Environment - 2 of 2

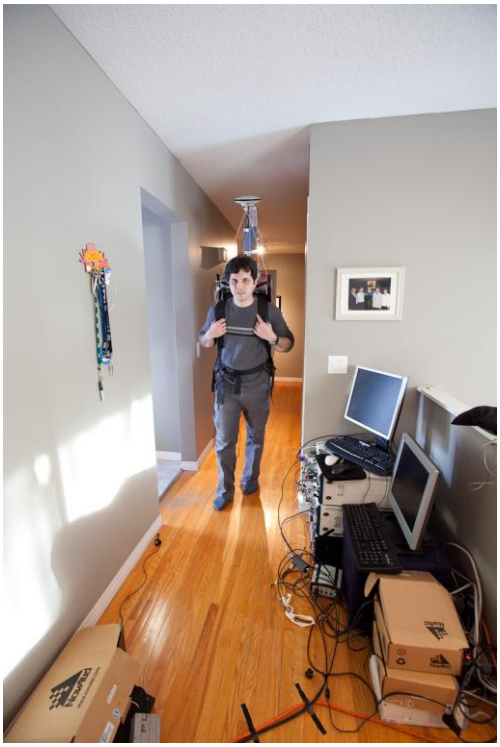

Figure 3.4: Ground Floor

Figure 3.5: Stairs to Basement

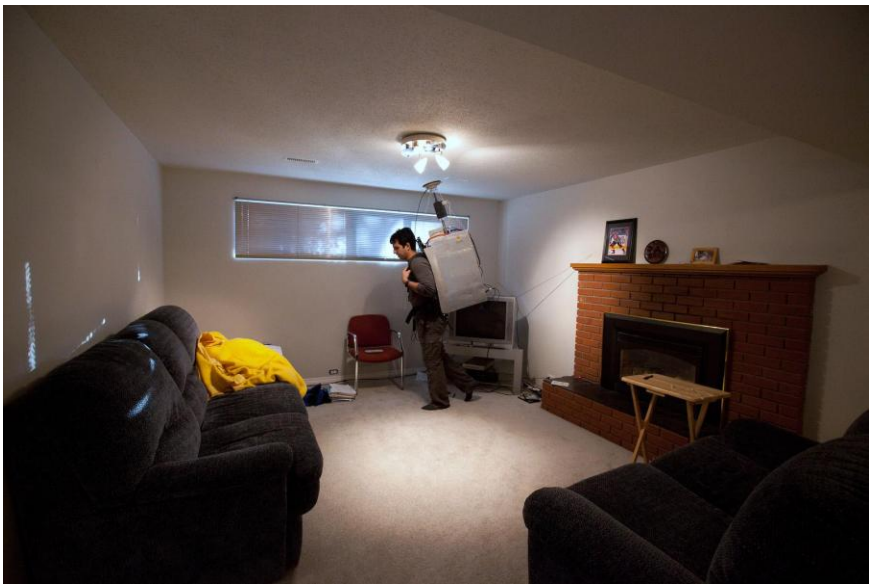

Figure 3.6: Basement

3.2.2 Equipment Setup

The data presented in this chapter was collected using the equipment setup presented in Figure 3.7. This setup consisted of a NovAtel GPS-702-GG antenna for GPS and GLONASS, a low-noise amplifier (LNA) for boosting the signal on long cable runs, and an RF splitter was used to feed the incoming RF signal to two different GNSS receivers. The GNSS receivers used can be separated into two groups – one for generating a reference navigation solution, and a second for the software receiver. To generate a GPS/GLONASS/INS tightly-coupled reference navigation solution, two receivers were needed. A NovAtel OEM4 DL4 receiver was used to log data from a Honeywell HG1700 IMU, and a second NovAtel OEMV3 receiver was used to log GPS/GLONASS measurements. The IMU and GNSS measurements were later combined and used in post-processing to compute the final reference navigation solution.

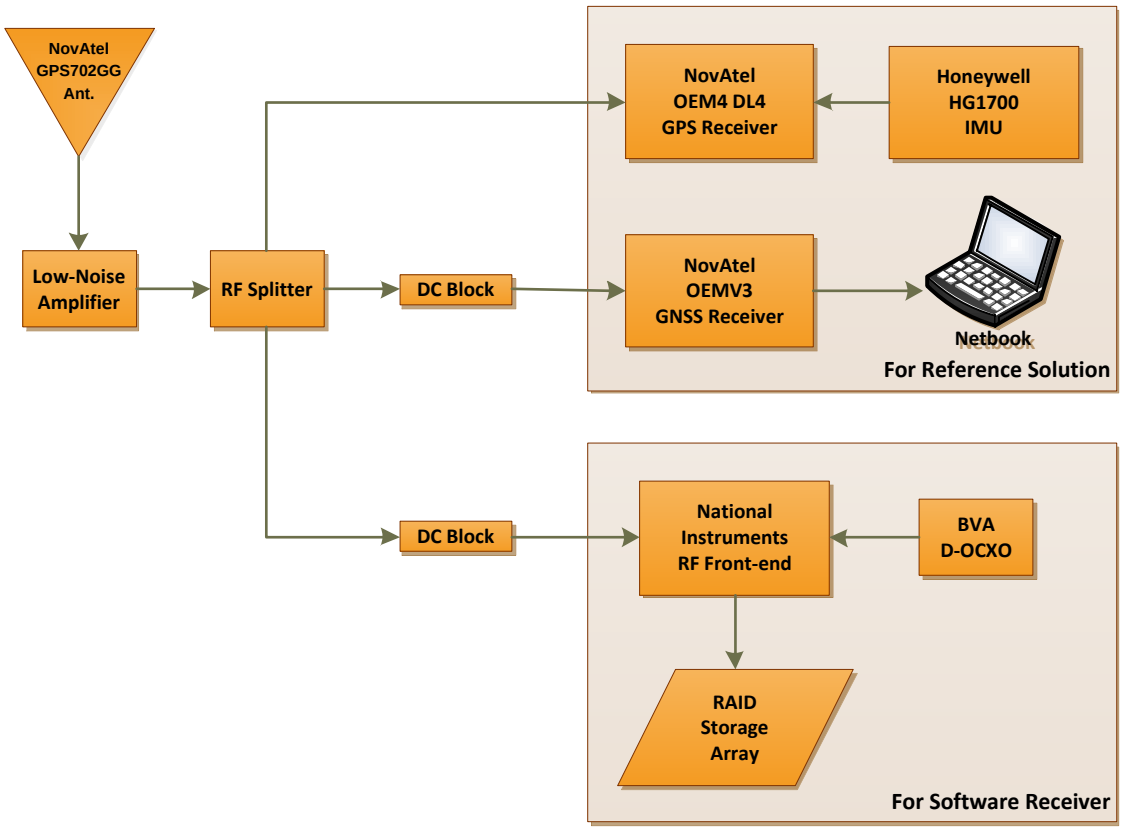

Figure 3.7: Equipment Setup for Wooden Framed House Data

For generating a reference tightly-coupled GNSS/INS solution, a NovAtel OEM4 DL4 GPS receiver was used to log data from a Honeywell HG1700 tactical grade inertial measurement unit (IMU), and a Novatel OEMV3 GNSS receiver was used to log GPS and GLONASS observations. IMU data from the HG1700 was logged at 100 Hz and provided accelerometer and gyroscope outputs in 3 axes; GPS and GLONASS observations from the OEMV3 were logged at 5 Hz. A second NovAtel GPS-702-GG antenna and OEMV3 receiver (not shown on Figure 3.7) was placed on a reference pillar located on the roof of the CCIT building at the University of Calgary; GPS and

GLONASS observations were logged at 20 Hz and was used for differential GNSS post-processing of the reference navigation solution. The NovAtel antenna, RF splitter, NovAtel OEM receivers and IMU were all mounted on an open-frame backpack for collecting pedestrian navigation data. The open-frame backpack is shown on Figure 3.2 through Figure 3.6.

A long antenna cable from the backpack was used to pass the RF signal from the antenna to a National Instruments RF front-end used for recording intermediate frequency (IF) data for the software GNSS receiver; the RF front-end was located on the ground floor shown in Figure 3.4 and Figure 3.8. Upon reaching the front-end, the RF signal is down converted to a complex IF signal, digitized with a resolution of 16 bit per sample, and sampled at 5 million samples per second. A high quality BVA double oven-controlled crystal oscillator (D-OCXO) was used to drive the RF front-end. IF data sampled by the front-end was stored on a hard disk RAID array for post-processing and testing. This setup is shown on the bottom left portion of Figure 3.8.

The primary reason for selecting a high quality oscillator (D-OCXO) was to allow for the testing of different oscillator models using the same dataset. By using a high quality oscillator, it is possible to increase the constraint on the receiver clock offset and drift states within the Kalman; this was done to evaluate the effectiveness of using a high quality oscillator for weak signal environments. With this setup, the effects of a lower quality oscillator can still be approximated by increasing the spectral density values in the oscillator error model used in the navigation filter. It should be noted that if a low-quality

oscillator was used, it would not possible to evaluate the effects a high quality oscillator. Although not discussed in detail, through the process of tuning the navigation filter for the above setup, it was found that increasing the constraint on the receiver clock states (such as using a OCXO clock model) often led to a reduction in tracking loop stability – causing loss of lock. Therefore, although a high quality oscillator was used for the hardware setup, a low-cost voltage-controlled temperature-compensated crystal oscillator (VCTCXO) clock model was used for the results presented herein.

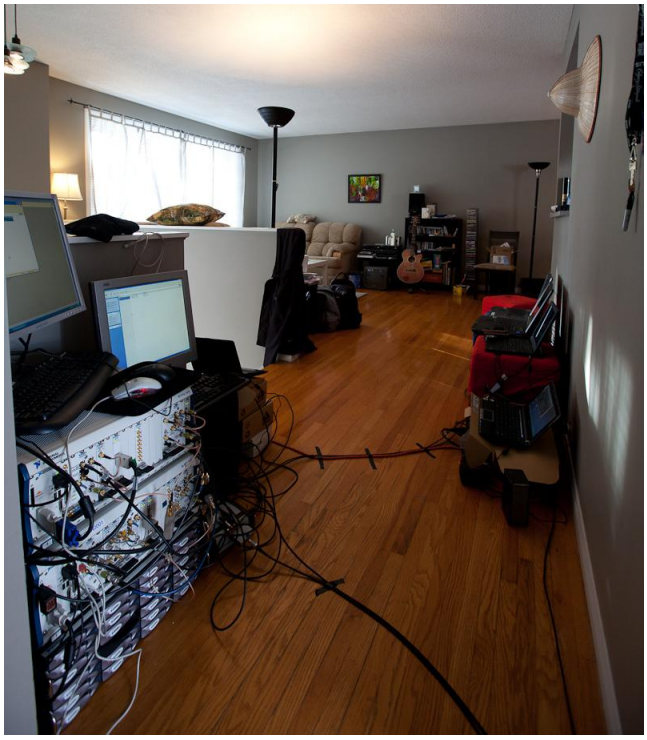

Figure 3.8: National Instruments RF Front-end (shown on the left)

3.2.3 Reference Navigation Solution

In order to determine the accuracy of the navigation solution generated by the software GNSS receiver being analyzed, a reference trajectory was generated for the antenna phase centre. This this trajectory serves as the reference navigation solution by which the scalar and vector-based GNSS receivers will be compared in this chapter. The reference solution was obtained using a tightly-coupled GNSS/INS solution computed by NovAtel's Waypoint Inertial Explorer post-processing software package. To achieve the decimetre level accuracy throughout the entire period of interest, the NovAtel inertial system was initialized with a 15 minute a static period, followed by 2 minutes of figure-8 motion to align the IMU; once fine alignment was achieved, the system was brought indoors. Upon completion of the indoor survey, the system was brought back outside and figure-8 manoeuvres were performed for a period of 2 minutes before allowing the system to sit stationary for another 10 minutes to facilitate reverse GNSS/INS processing. After processing the reference solution in both the forward and reverse direction, the two solutions were combined and smoothed using a Rauch-Tung-Striebel (RTS) smoother. The trajectory used as the reference navigation solution had a combined separation of less than 50 cm in position and 4 cm/s in velocity. Satellites which were above the horizon at the time of the data collection are shown on Figure 3.9; the numbers represent the PRNs of GPS satellites available and lines represent the trajectory of GPS satellites as they traverse the sky.

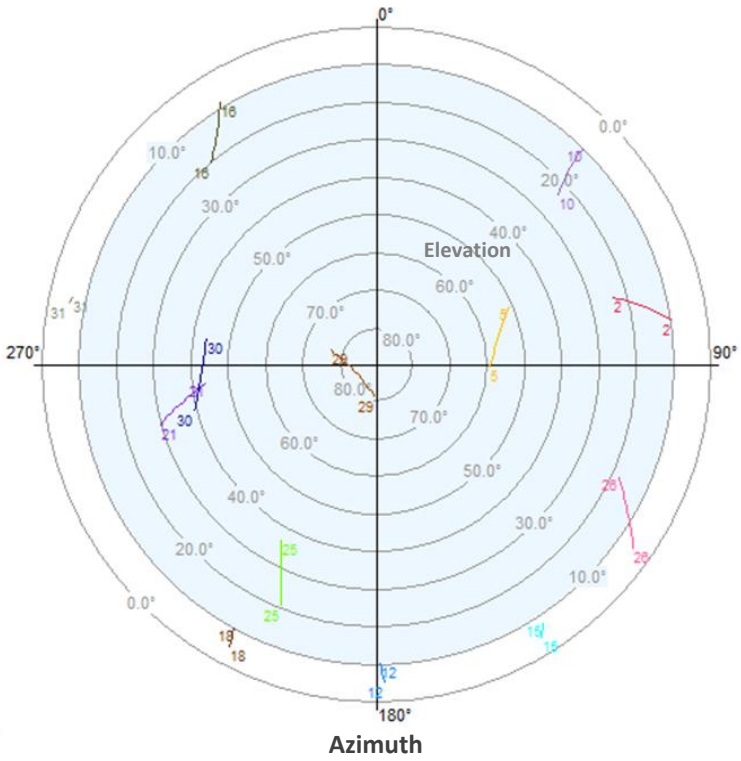

Figure 3.9: Sky Plot of Satellite Availability

3.3 Receiver Performance

In the following subsections, the performance of a traditional scalar tracking and vector-based tracking GNSS receiver are compared under environments introduced in section 3.2.1. The performance analysis focuses on two areas: tracking and navigation. Metrics for evaluating the receiver performance are introduced in their respective sections.

For the results presented herein, a Kalman filter using pseudorange and Doppler observations was employed to estimate receiver position, velocity and clock terms. Tracking and navigation filtering parameters used herein are shown in **Error! Reference**

source not found. and Table 3.2, respectively. To estimate the receiver clock offset and drift, a voltage-controlled temperature-compensated crystal oscillator (VCTCXO) model was used. Although the actual oscillator used to drive the RF front-end was a high-end double-oven crystal oscillator (D-OCXO), by modeling the oscillator as a VCTCXO, it is possible to evaluate the performance that one may expect from a low-cost receiver that uses a much more economical VCTCXO instead.

Table 3.1: Signal Tracking Parameters

General Tracking Parameters	
Sampling Rate (MSPS)	5.00
Sampling Type	Complex
Number of Correlators	3
Maximum Coherent Integration (ms)	20
Standard Tracking Parameters	
Code Loop Filter Order	1
Frequency Loop Filter Order	2
Frequency Loop Filter Bandwidth (Hz)	8.00
Phase Loop Filter Order	3
Phase Loop Filter Bandwidth (Hz)	15.00
Kalman Filter Tracking Parameters	
Amplitude Spectral Density $(\mathrm{dB}/\sqrt{\mathrm{Hz}})$	1.00
Code Carrier Divergence $(\mathrm{m}/\sqrt{\mathrm{Hz}})$	0.04
Line of Sight Spectral Density $(\mathrm{m/s}^2/\sqrt{\mathrm{Hz}})$	4.00
Frequency Error Threshold	5.00
Oscillator H-Parameter h_0 $(\mathrm{Hz}/\sqrt{\mathrm{Hz}})$	1.00E-21
Oscillator H-Parameters h_{-1} $(\mathrm{Hz}^2/\sqrt{\mathrm{Hz}})$	1.00E-20
Oscillator H-Parameters h_{-2} $(\mathrm{Hz}^3/\sqrt{\mathrm{Hz}})$	1.00E-20

Table 3.2: Navigation Filter Parameters

Navigation Filter Parameters	
GPS Measurement Rate (Hz)	20
GPS Pseudorange Standard Deviation (m)	5.00
GPS Doppler Standard Deviation (m/s)	0.20
Observed UWB Range Measurement Rate (Hz)	10.00
Simulated UWB Range Measurement Rate (Hz)	1.00
UWB Range Standard Deviation (m)	2.00
C/N_0 Mask (dB-Hz)	30.00
Elevation Mask (degrees)	10.00
Horizontal Velocity Spectral Density $(m/s/\sqrt{Hz})$	1.00
Vertical Velocity Spectral Density $(m/s/\sqrt{Hz})$	0.50
Oscillator H-Parameter h_0 $(Hz/\sqrt{Hz})$	1.00E-21
Oscillator H-Parameters h_{-1} $(Hz^2/\sqrt{Hz})$	1.00E-20
Oscillator H-Parameters h_{-2} $(Hz^3/\sqrt{Hz})$	1.00E-20

3.3.1 GNSS Signal Tracking Performance

In order to evaluate and compare the tracking performance of a scalar and vector-based receiver, the robustness of the code and frequency tracking along with the tracking sensitivity in weak signal environments will be compared based on the carrier-to-noise density ratio (C/N_0) and Frequency Lock Indicator observed in different environments.

C/N_0 estimates play an important role in determining the relationship between the power of the incoming signal being tracked and the background RF noise. For GPS receivers operating outdoors, C/N_0 values that can be expected are typically greater than 40 dB-Hz (Spilker 1996). For indoor GNSS applications however, C/N_0 are much lower due to signal attenuation and deep fading caused by multipath interference. The method used for estimating the C/N_0 is commonly referred to the narrow band, wide band method (Van

Dierendonck 1996c) and makes use of complex correlator outputs to compute the narrow band power (NBP) and wide band power (WBP) of the incoming signal. The NBP is then differenced with respect to the WBP, and averaged over a period of 20 milliseconds; the resulting value is then used to compute the carrier-to-noise density ratio (Van Dierendonck 1996c, Muthuraman & Borio 2010). When plotted in the form of a time series, the C/N_0 values provide an indication of how well a GNSS signal is being tracked. A sudden drop in C/N_0 below 20 dB-Hz typically indicates that a receiver has experienced a loss of lock on a particular satellite. However, one should bear in mind that a decrease in C/N_0 can also occur purely from signal attenuation caused by line-of-sight obstructions between the receiving antenna and the satellite being tracked. With this in mind, it is important to state that the absolute C/N_0 values cannot be used as a definitive metric on tracking performance; rather, it is relative C/N_0 differences between receivers over the same period that should be used to gauge tracking performance.

Similar to the C/N_0 estimate, the frequency lock indicator (FLI) allows the receiver to gauge the frequency tracking performance for a particular satellite. The full range of the FLI employed in GSNRx^{TM} ranges from -1 to +1. As the frequency error tends toward 0, the FLI value will converge toward +1 (Mongrédien et al 2006, Mongrédien 2008). Since poor frequency lock results in a loss of power on the tracked signal, a drop in the FLI will also correspond with a drop in C/N_0. FLI values are computed at each integration period (20 milliseconds); in contrast, the C/N_0 estimate is averaged over a 1 second interval.

3.3.1.1 Tracking Sensitivity and Robustness

To compare tracking sensitivity between scalar and vector-based GNSS receivers in different operating environments, the C/N_0 and FLI values are examined. Figure 3.10 and Figure 3.11 show the C/N_0 and FLI as a function of time when using scalar and vector-based tracking respectively in an outdoor kinematic environment. What is immediately apparent is that several instances exist in which loss of lock occurs on PRNs 10, 16, and 25 during the first 100 seconds. Referring to the sky plot on Figure 3.9, it is apparent that these three satellites were low lying satellites. In contrast to the scalar receiver, results from the vector-based receiver shown on Figure 3.11 did not indicate a loss of lock on any of the satellites being tracked during the same period.

In order to better compare the tracking performance differences between the scalar and vector-based receiver over the same period, the 66^{th} percentile of the C/N_0 and FLI values for the two receivers are shown on Figure 3.12. Here, the 66^{th} percentile values represent the minimum C/N_0 and FLI values achieved for a given satellite/receiver combination 66% of the time during the period of interest. The left and right subplots on Figure 3.12 show the 66^{th} percentile values of the C/N_0 and FLI respectively for each available satellite PRN. The red bars on the figure represent the results of the scalar receiver, while the green bars represent the results taken from the vector-based receiver. In the case of open-sky environment, the *overall* performance of the two receivers is very similar.

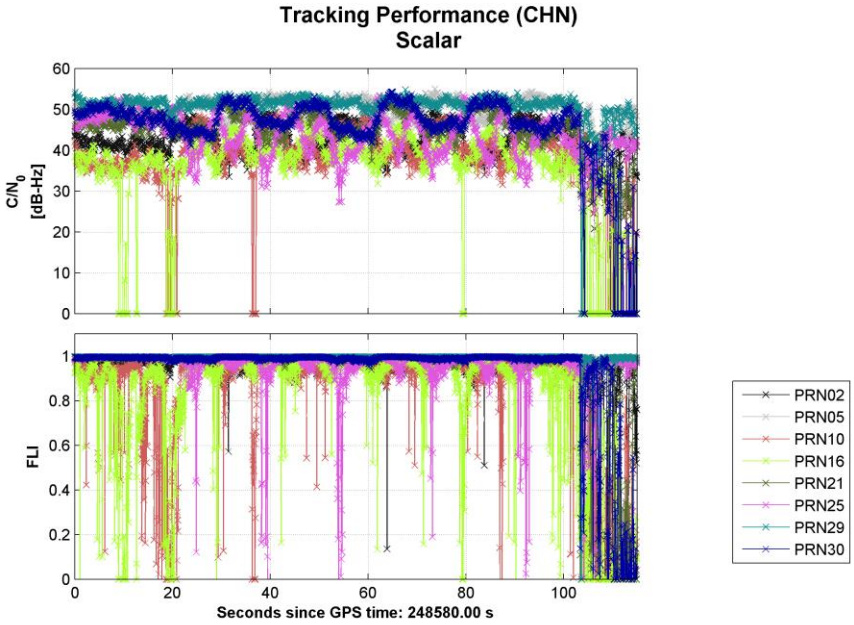

Figure 3.10: Outdoor Tracking Performance (Scalar Tracking)

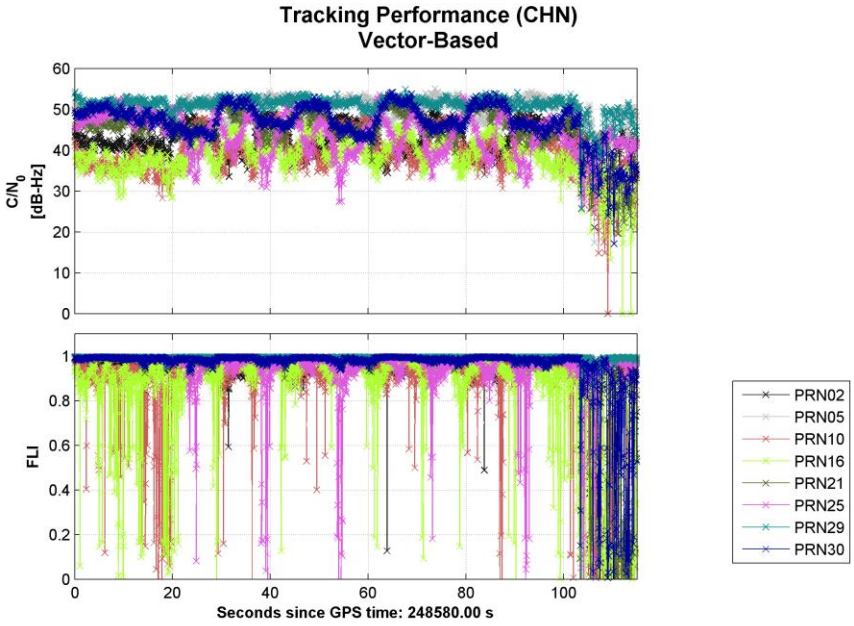

Figure 3.11: Outdoor Tracking Performance (Vector-Based Tracking)

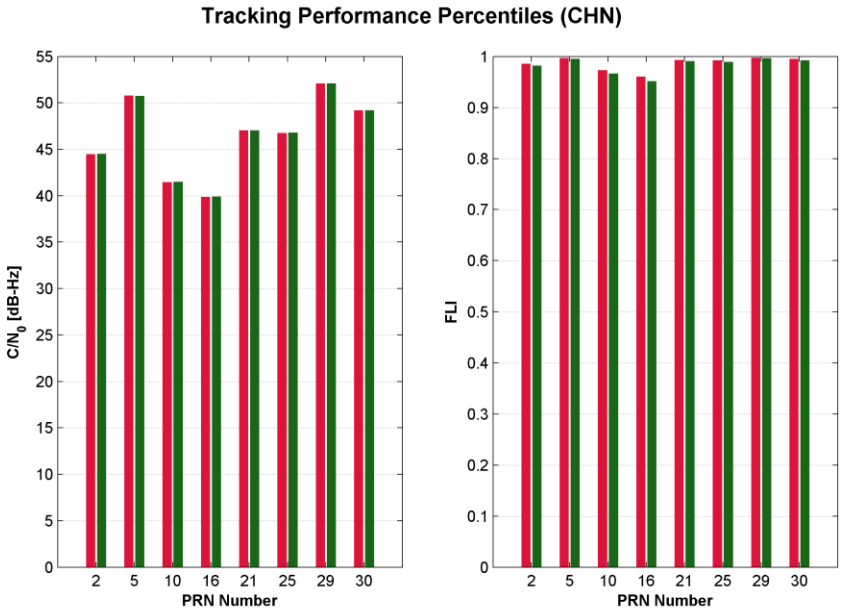

Figure 3.12: Outdoor Tracking Statistics for Scalar Tracking (Red) and Vector-Based Tracking (Green)

After spending just over 100 seconds in an open sky environment, the receiver moves towards the back entrance of the house. As the receivers approach the doorway in the last 15 seconds, occlusions and multipath interference caused by the house results in a large drop in C/N_0 and FLI for both receivers. However, it is possible to see that the vector-based tracking algorithm is much more robust compared to scalar tracking. During this transition period, the vector-based receiver experienced a loss of lock on PRN 10 and 16 in just three epochs. The scalar receiver on the other hand experienced significant loss of lock on several satellites just before the receiver is brought inside the house. Upon entering the house and travelling through the upstairs hallway, the trend continues in Figure 3.13 where the scalar receiver had great difficulty tracking low elevation satellites.

During this same period, the vector-based receiver (shown in Figure 3.14) was able to track all satellites in view and only experienced a brief loss of lock for PRN 10 and 16.

By looking at the 66th percentile C/N_0 and FLI values for PRN 10 and 16 in Figure 3.15, it is clear that the vector-based receiver performed noticeably better than the scalar receiver while in the upstairs portion of the timber-framed house. For both PRNs, it was found that the vector-based receiver had a 66th percentile C/N_0 value 16 dB-Hz higher than the scalar receiver; likewise, it was found that the vector-based receiver had 66th percentile FLI values 0.4 higher than that of the scalar tracking receiver. Although a major improvement in tracking performance was found for PRN 10 and 16, tracking performance for other satellites were almost identical between the two receivers during this period of time.

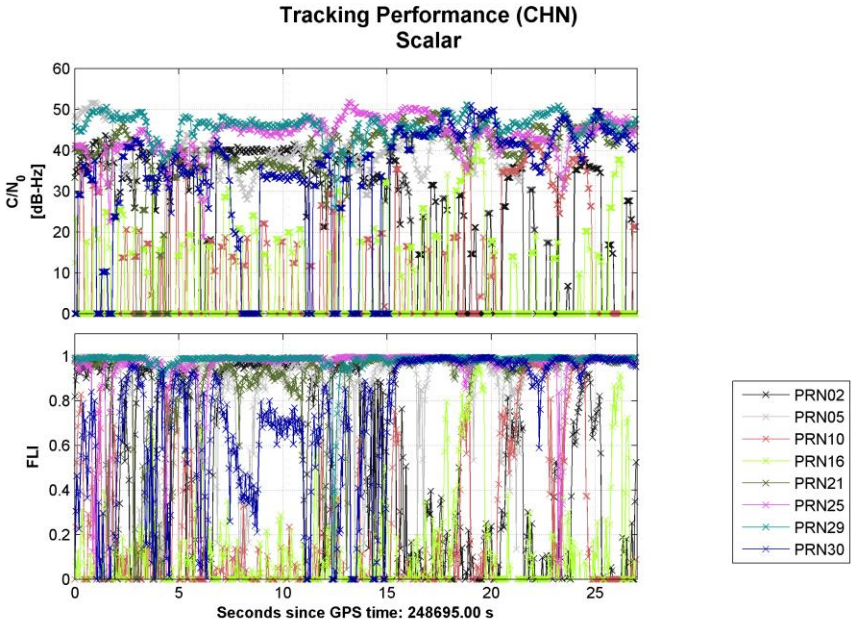

Figure 3.13: Indoor Upstairs Tracking Performance (Scalar Tracking)

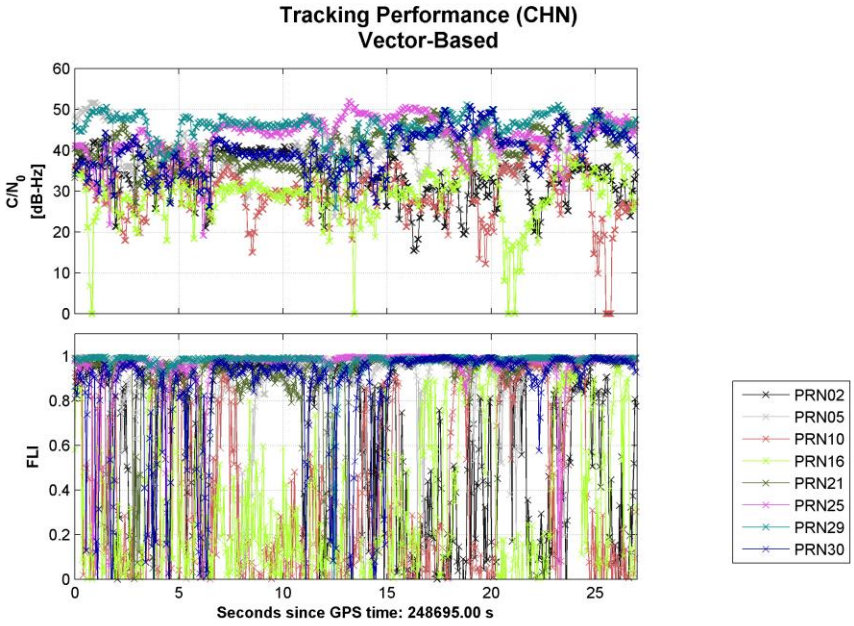

Figure 3.14: Indoor Upstairs Tracking Performance (Vector-Based Tracking)

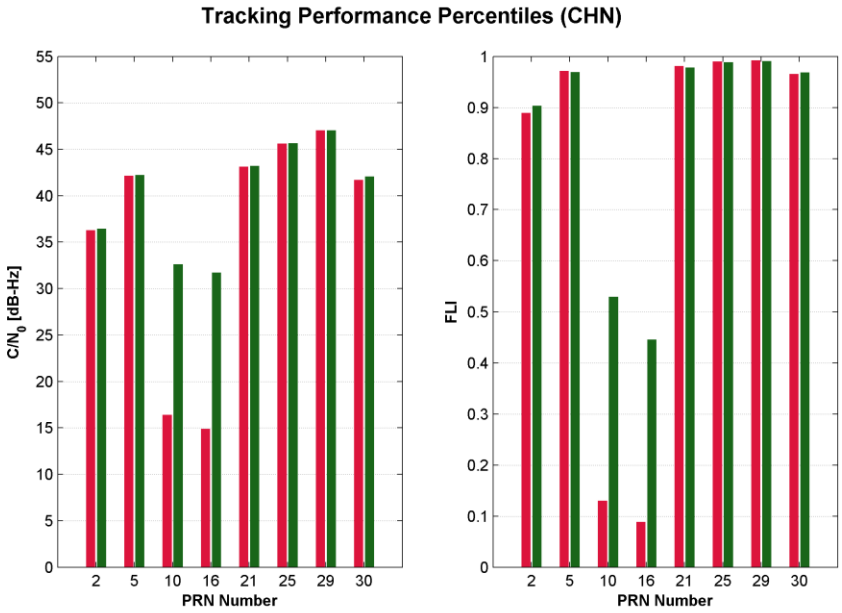

Figure 3.15: Indoor Upstairs Tracking Statistics for Scalar Tracking (Red) and Vector-Based Tracking (Green)

To fully appreciate the GNSS signal tracking robustness that a vector-based receiver provides, the receiver was brought downstairs to the basement; Figure 3.16 and Figure 3.17 shows this transition as the receiver travels down the stairway to the basement. Examining the C/N_0 values from the scalar receiver on Figure 3.16, it is possible to see that by the time the receiver has reached the basement level, the receiver had lost lock on all satellites. However, the vector-based receiver shown on Figure 3.17 was able to track all available satellites during this same period with only a minor but noticeable increase in loss of lock compared to the period while travelling upstairs within the house. Note also that during this period, for the first time, PRN 2 and 5 also experience a brief loss of

lock on the vector-based receiver. Referring to the sky plot on Figure 3.9, it is possible to see that PRN 2 is a low elevation satellite while PRN 5 is a high elevation satellite.

The differences in tracking performance as the scalar and vector-based receivers were moved to the basement can be seen more clearly on Figure 3.18. Here it was found that the overall tracking performance of PRN 5 was similar between the two receivers. However, PRN 2, 10, and 16 all indicated a dramatic drop in C/N_0 and FLI, similar to what was shown on Figure 3.15 while the receivers were upstairs.

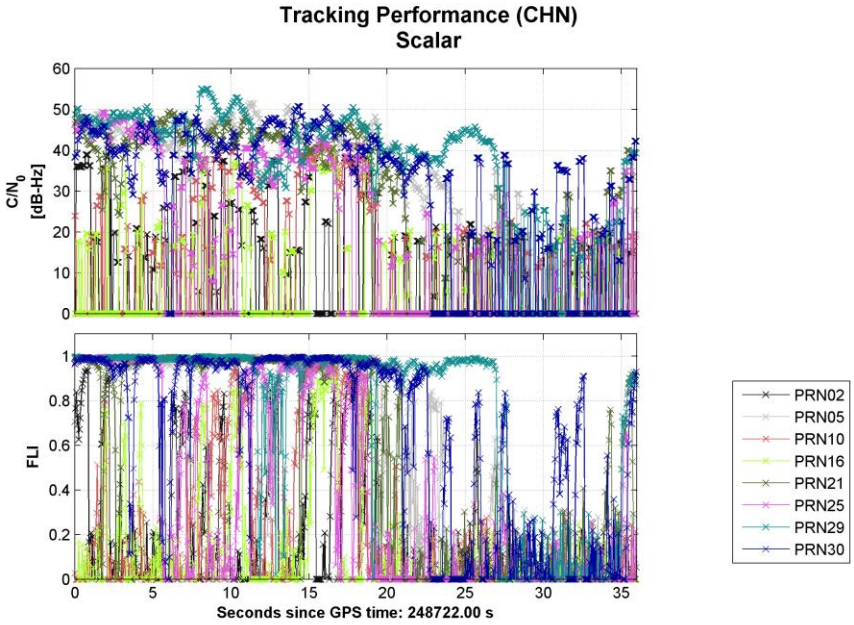

Figure 3.16: Descending Stairs Tracking Performance (Scalar Tracking)

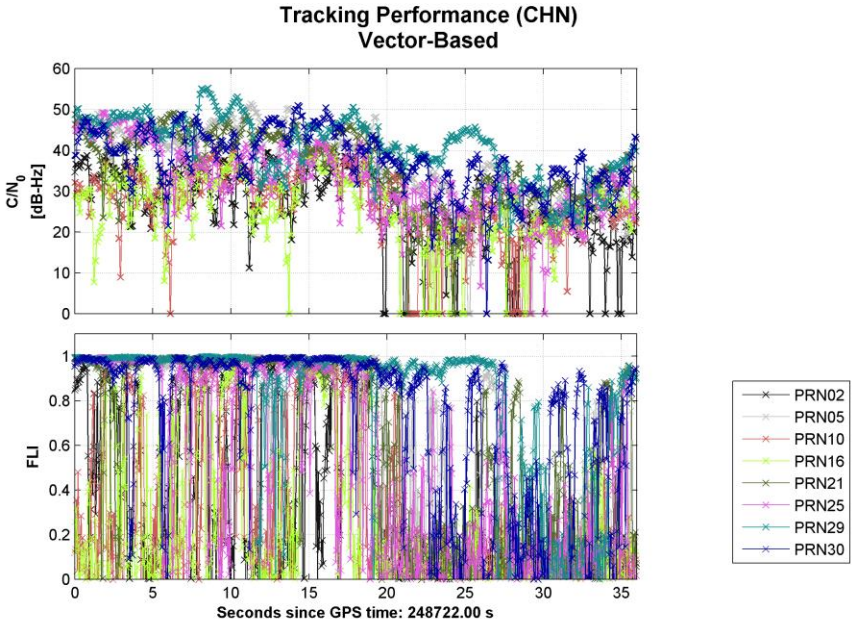

Figure 3.17: Descending Stairs Tracking Performance (Vector-Based Tracking)

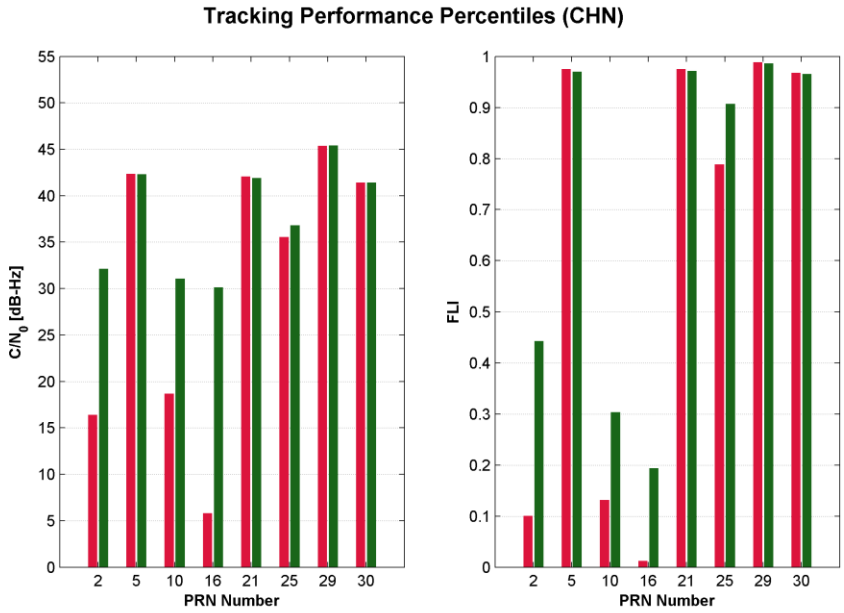

Figure 3.18: Descending Stairs Tracking Statistics for Scalar Tracking (Red) and Vector-Based Tracking (Green)

Comparing the tracking performance of the scalar and vector-based receiver on Figure 3.19 and Figure 3.20, the C/N_0 figures clearly show that the vector-based receiver was capable of tracking all satellites in view even while operating in the basement. The scalar tracking receiver however showed that it struggled to track all but the high elevation satellites – namely PRNs 5, 29, and 30. Moreover, the 66^{th} percentile C/N_0 and FLI values shown on Figure 3.21 shows that the scalar receiver could not reliably track PRNs 2, 10, and 16 whatsoever; meanwhile the vector-based receiver was able to track all eight satellites while in the basement. Also, by comparing the relative C/N_0 and FLI values shown on Figure 3.21, it is also clear that for satellites that could be tracked by both the

scalar and vector-based receivers, the vector-based receiver had an overall higher C/N_0 and FLI value compared to the scalar receiver.

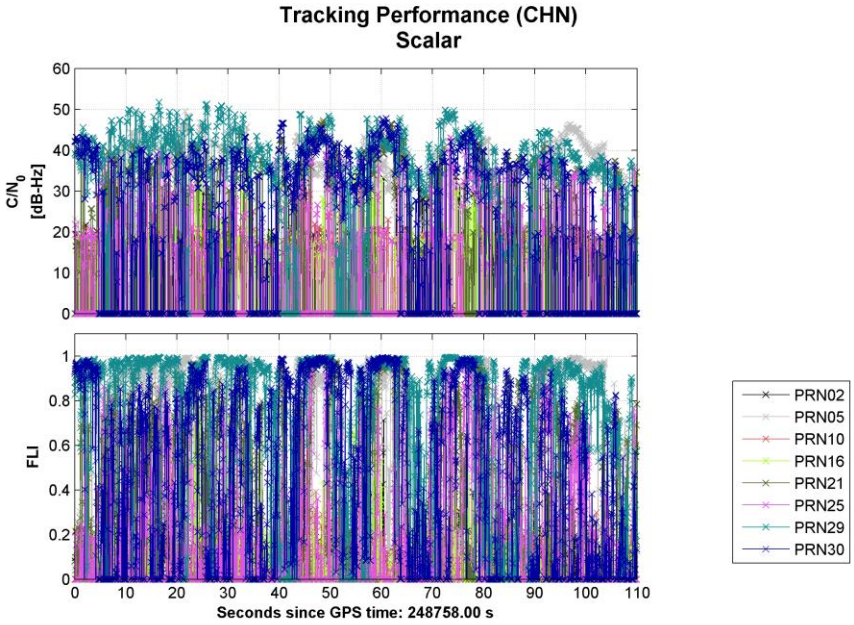

Figure 3.19: Basement Tracking Performance (Scalar Tracking)

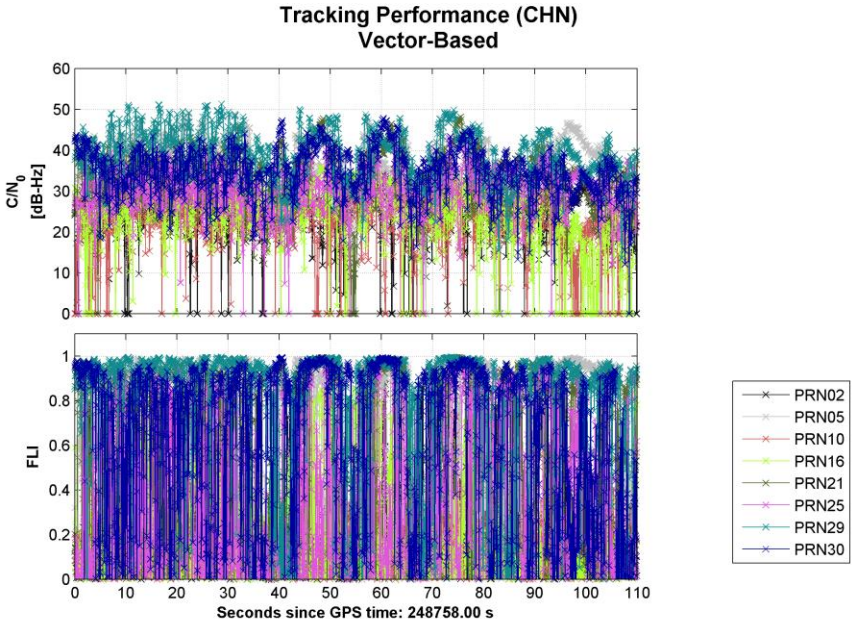

Figure 3.20: Basement Tracking Performance (Vector-Based Tracking)

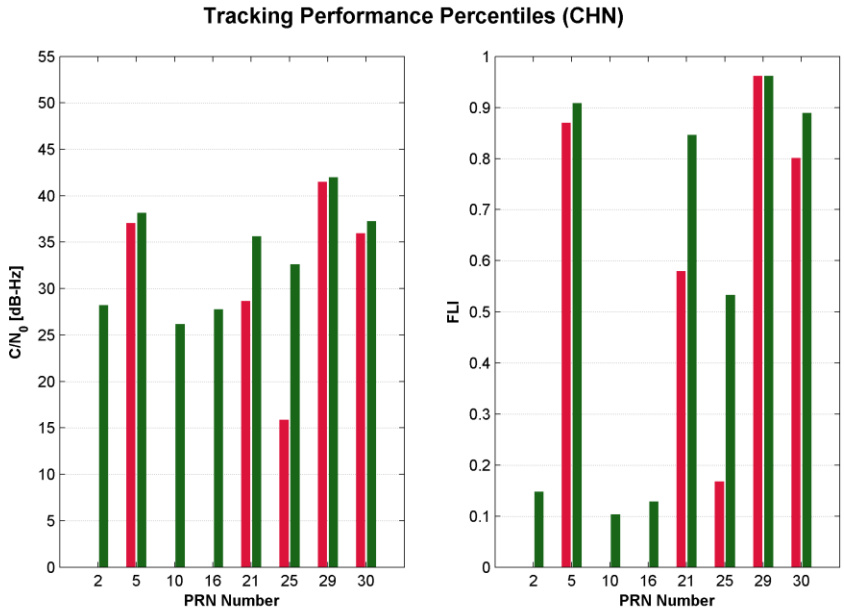

Figure 3.21: Basement Tracking Statistics for Scalar Tracking (Red) and Vector-Based Tracking (Green)

From the tracking performance plots presented thus far, it is evident that the performance gains provided by a vector-based GNSS receiver is indeed significant. This, therefore, provides motivation for examining the performance of vector-based GNSS receivers operating in even more challenging environments such as in urban canyons and within concrete buildings that attenuate GNSS signals to a larger degree; these environments are explored in chapters 4 and 5.

3.3.1.2 Observation Quality

The robustness of vector-based tracking loops easily exceeds that of scalar tracking loops while operating in indoor environments such as the timber-framed house exemplified in

this chapter. However, although a vector-based GNSS receiver is capable of generating GNSS observations such as pseudorange and Doppler estimates in such challenging environments, it is still important to evaluate the quality of these measurements. To do this, the pseudorange and Doppler residuals are examined as a function of the C/N_0 and FLI values respectively. The goal here is to determine the quality of the measurement precision as a function of the tracking performance and, indirectly, the signal strength. Note that the values of the residuals presented are all in *absolute* values.

In the following figures, the distribution of measurement residuals are shown for the four environments introduced in this chapter. Separate figures are provided for pseudorange and Doppler residuals. As can be seen in Figure 3.22, the residual distribution plots consists of five portions; starting from the top-left subplot and moving in a clockwise direction, the first, left-most, subplot consists of a cumulative histogram of all residuals (both used and rejected by the navigation filter) over the time period spent in a given environment. Contrary to the standard convention of a cumulative histograms plot, the percentage of epochs increases as the residuals tend toward zero. The reason for this is to show the percentage of epochs where a user can expect the measurement precision to be within – rather than outside – of a certain range.

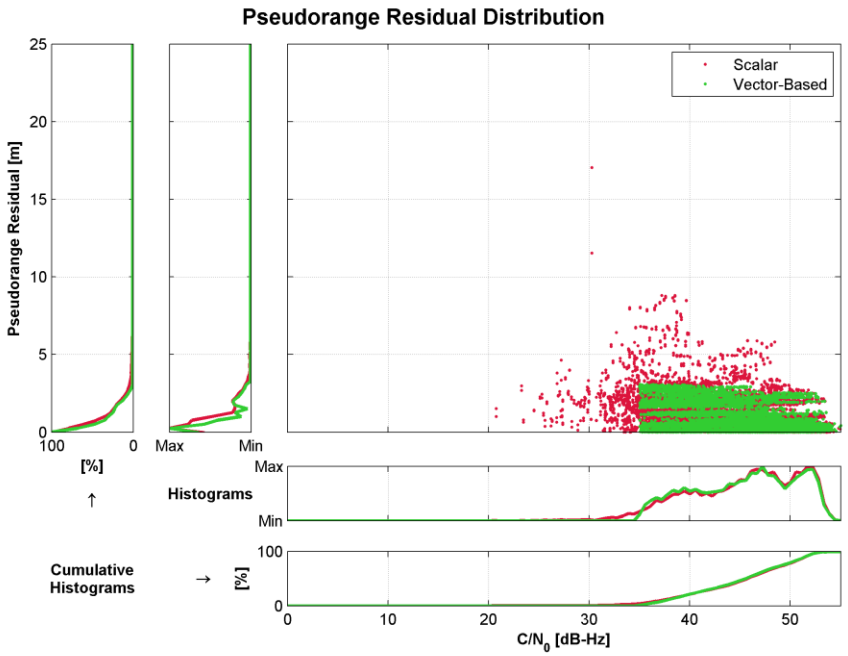

Figure 3.22: Outdoor Pseudorange Residual Distribution

The second subplot from the left shows a normalized histogram of the measurement residuals as a function of the residual value. This gives an indication of the distribution of the residuals as a function of its range; for example, if the measurements have a high precision, this will result in a histogram plot with a large spike, whereas if measurements have low precision, the histogram will show a broad distribution of different values. The histogram for each receiver shown is normalized based on the maximum number of residuals in a given residual bin. Thus, the histogram plot only provides an indication of the residual distribution over the time period being compared and cannot be used to directly compare the actual number of available observations within a bin between multiple receivers.

The third subplot (top-right) is a scatter plot of all available measurement residual values plotted as a function of the tracking statistic; pseudorange measurement residuals are plotted as a function of C/N_0 and Doppler measurement residuals are plotted a function of FLI. Note that in vector-based tracking, no residuals below a C/N_0 of 35 dB-Hz are provided; the reason for this is due to the measurement filtering required to allow the vector-tracking receiver to achieve best performance with regards to tracking robustness while operating indoors. Because pseudorange and Doppler measurements tend to have larger errors when the C/N_0 value is low, these measurements if left unfiltered will introduce velocity errors into the navigation solution that result in poor frequency estimates of the incoming GNSS signals being tracked in the vector-based GNSS receiver. These large frequency error variations may exceed the bandwidth of the tracking loops and therefore result in a complete loss of lock.

The forth subplot is similar to that of the second subplot whereby it shows a distribution of the measurement residuals as a function of the tracking statistic – again, C/N_0 is used for pseudorange measurements and FLI is used for Doppler measurements. Lastly, the cumulative histogram of the measurement residuals as a function of its tracking statistics is provided in the fifth subplot. Similar to the first subplot, the cumulative histogram for the tracking statistics gives an indication of the percentage of observations with a C/N_0 or FLI value above a certain range.

By examining Figure 3.22, it is possible to see that when the strength of the incoming signals are very strong – where the C/N_0 is equal or greater than 50 dB-Hz – scalar

tracking and vector-based tracking produces very similar pseudorange residuals. However, as the signals become weaker due to line of sight occlusion and multipath interference, vector-based tracking has the ability to greatly improve the precision of pseudorange observations as compared to scalar tracking. In fact, it is evident in Figure 3.22 that all pseudorange measurements generated by the vector-based receiver have an absolute precision that is better than 4 metres. On the other hand, pseudorange measurements generated by the scalar tracking receiver had a noticeable increase in the magnitude of their residuals. Similar to the pseudorange residual distribution shown on Figure 3.22, the absolute Doppler residual distribution presented on Figure 3.23 shows that the Doppler measurements provided by the vector-based receiver had noticeably smaller residuals as compared to the scalar tracking receiver. This is despite the fact that there are many more measurements with relatively low FLI values.

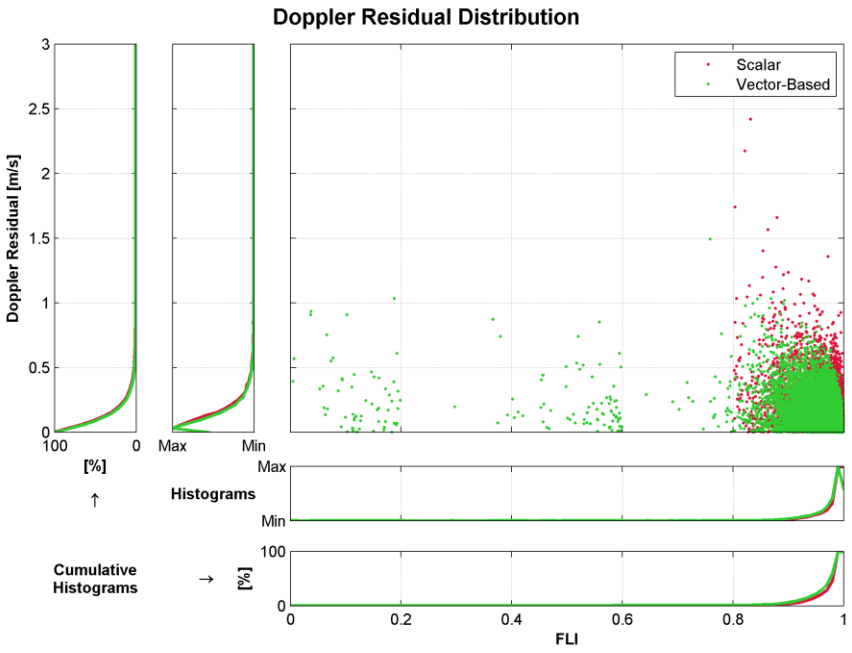

Figure 3.23: Outdoor Doppler Residual Distribution

When observing the pseudorange residual plots found on Figure 3.24, it is once again possible to see the benefits of vector-based tracking whereby the corresponding pseudorange residuals were much smaller than those generated by the scalar receiver while operating in the upstairs portion of the timber-framed house. However, the Doppler residuals shown on Figure 3.25 did not indicate dramatic improvement in measurement precision. Given this, it is interesting to note that for both pseudorange and Doppler measurements, the vector-based receiver was capable of generating measurements of very consistent precision down to a C/N_0 of 35 dB-Hz – even while operating inside a wooden house.

Recall from section 3.3.1.1 that as the user moved from the ground level portion of the house down to the basement level, the scalar receiver loses lock on many of the low lying satellites while the vector tracking was capable of tracking all satellites in view. With this in mind, it possible to see in Figure 3.26 and Figure 3.27 that the pseudorange and Doppler measurements generated by the scalar receiver resulted in measurement residuals of similar scale compared to the residuals from the vector-based receiver. However it is important to bear in mind that the scalar receiver had far fewer measurements available to compute a navigation solution from than the vector-based receiver – this is clearly shown in Figure 3.28 and Figure 3.29. As a result, the residuals obtained from the scalar receiver do not necessarily indicate that the measurements were of equal quality compared to that of the vector-based receiver. Note that although the Doppler observation availability is not shown, they are very similar to the pseudorange availability found on Figure 3.28 and Figure 3.29.

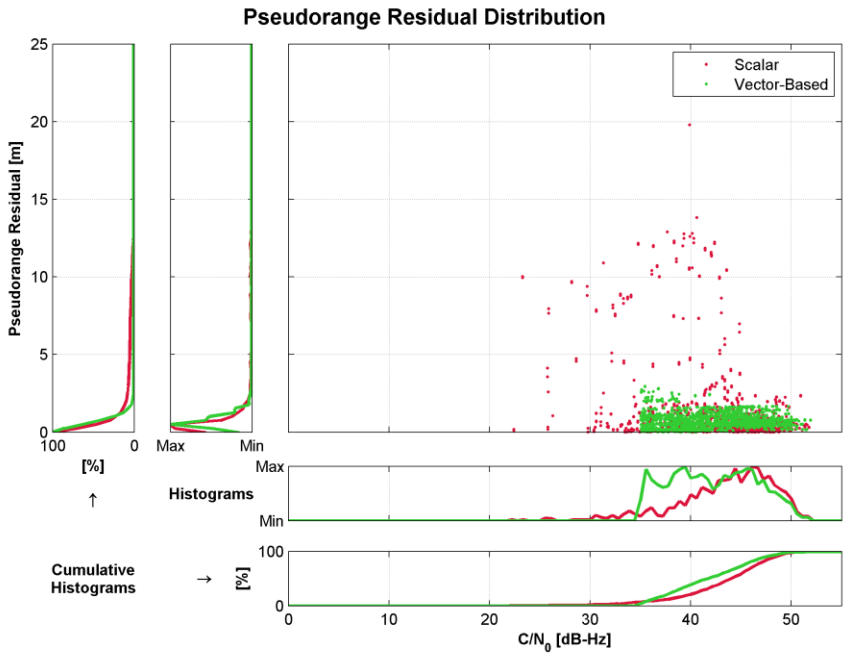

Figure 3.24: Indoor Pseudorange Residual Distribution (Upstairs)

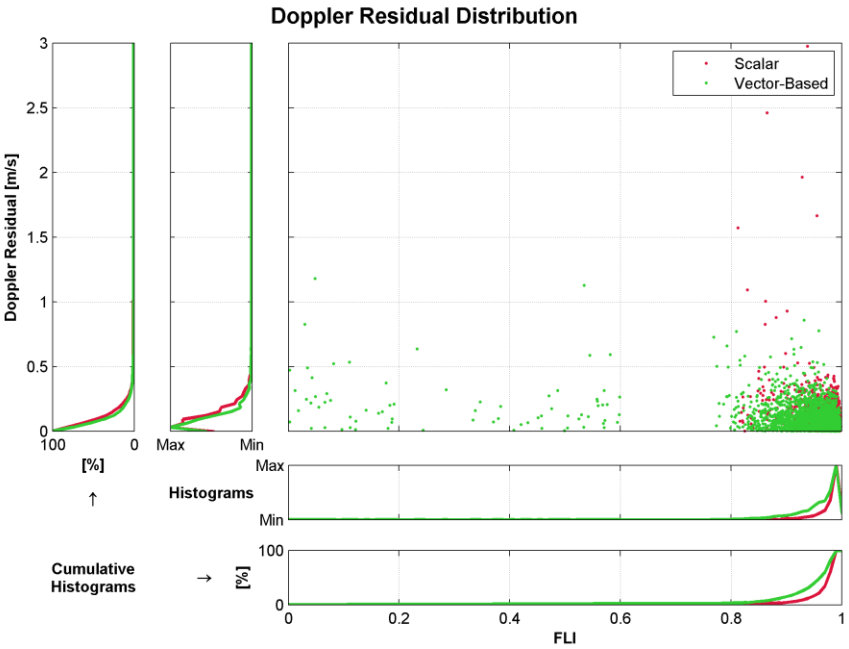

Figure 3.25: Indoor Doppler Residual Distribution (Upstairs)

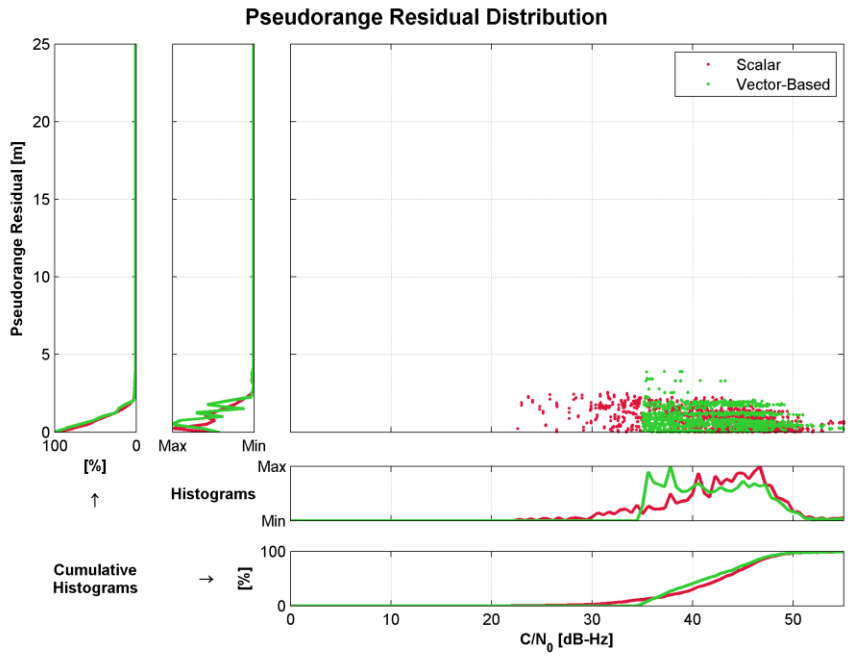

Figure 3.26: Indoor Pseudorange Residual Distribution (Descending to Basement)

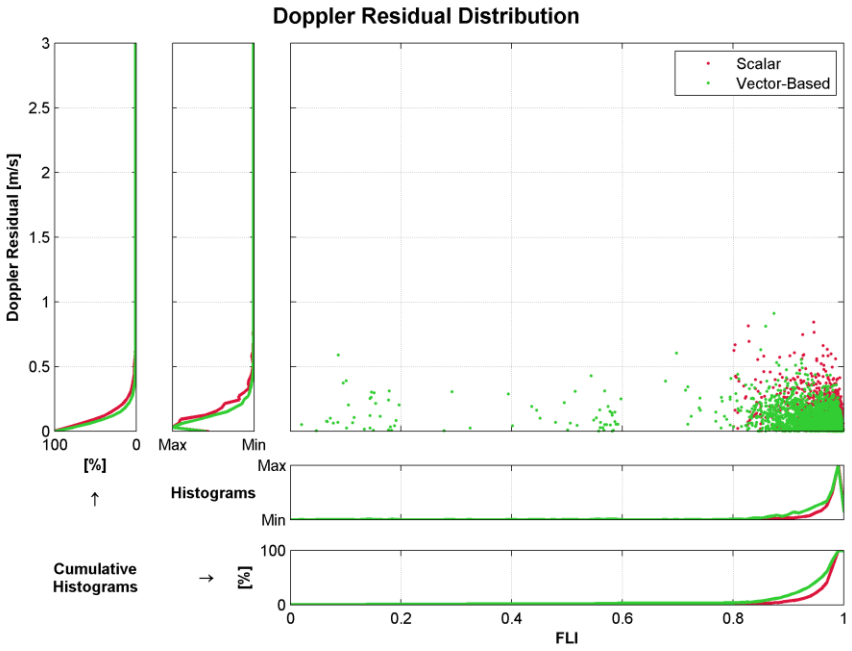

Figure 3.27: Indoor Doppler Residual Distribution (Descending to Basement)

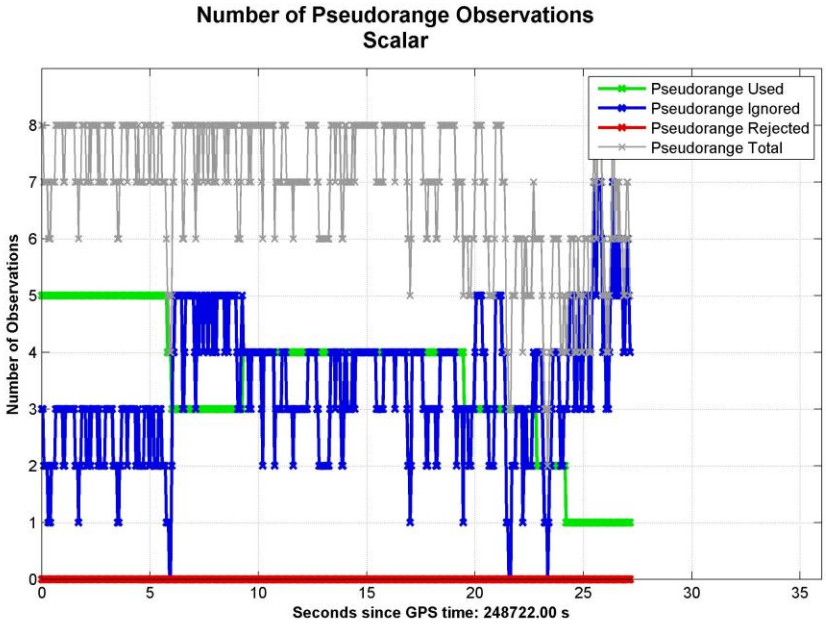

Figure 3.28: Observation Availability for Scalar Receiver (Descending to Basement)

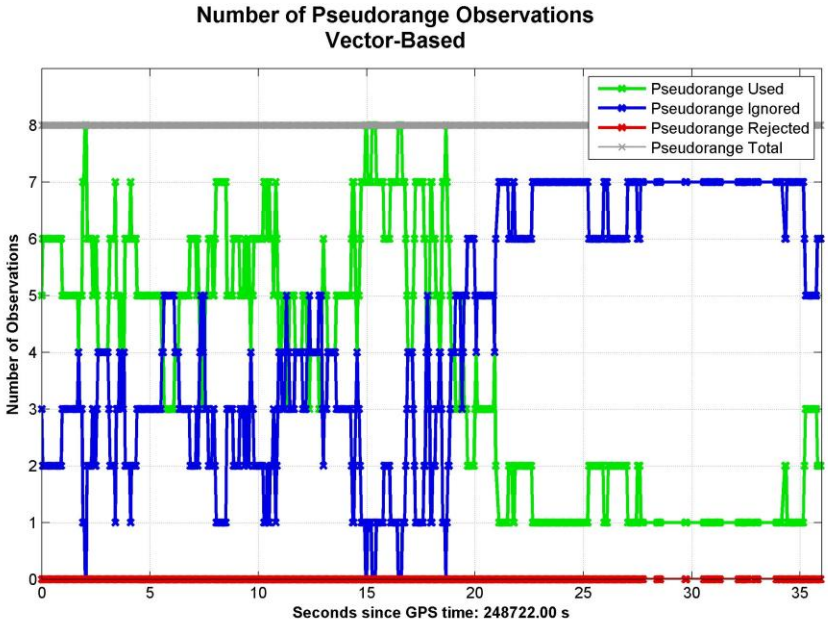

Figure 3.29: Pseudorange Availability for Vector Receiver (Descending to Basement)

Moving on to basement level of the house, Figure 3.30 and Figure 3.31 show the number of pseudorange observations generated by the two receivers while operating in the basement of the timber-framed house. Once again, although the availability of Doppler measurements was not shown, they are identical to that of the pseudorange availability for both receivers. Here, it is apparent that the vector-based receiver was able to generate many more usable pseudorange and Doppler observations as compared to the scalar receiver. The primary reason for the large number of ignored observations on the scalar receiver is due to the fact that navigation solution requires the tracking loop to have bit-sync before it will make use of the measurement. Likewise, the vector-based receiver ignores observations with a C/N_0 that is less than 35 dB-Hz; thus, although there are

many more pseudorange and Doppler measurements available to the vector-based receiver, they were not all used by the navigation solution.

The pseudorange and Doppler residual distribution shown on Figure 3.32 and Figure 3.33 confirms the results shown on Figure 3.28 and Figure 3.29; as the two receivers transitioned from the upstairs portion of the house down to the basement level. Once again, the vector-based receiver showed that the overall precision of the pseudorange was 5 metres or less whereas the scalar receiver produced measurement residuals that, at times, reached close to 20 metres. However, the Doppler residual for the vector-based receiver showed a noticeable increase in range compared to the scalar receiver. Whereas the Doppler residuals for the vector-based receiver was typically below 0.5 m/s in the upstairs portion of the house, Doppler residuals shown on Figure 3.33 had a range of over 2.0 m/s.

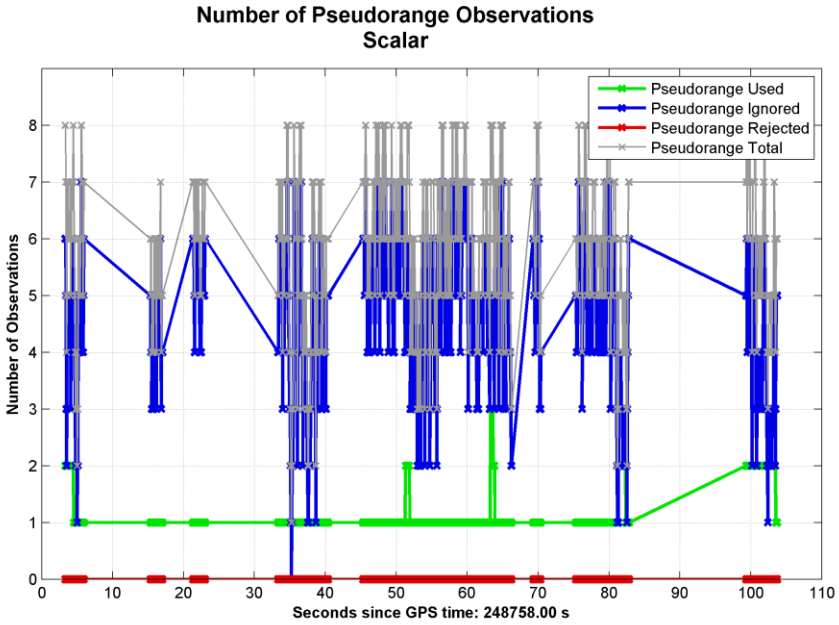

Figure 3.30: Pseudorange Availability for Scalar Receiver (Basement)

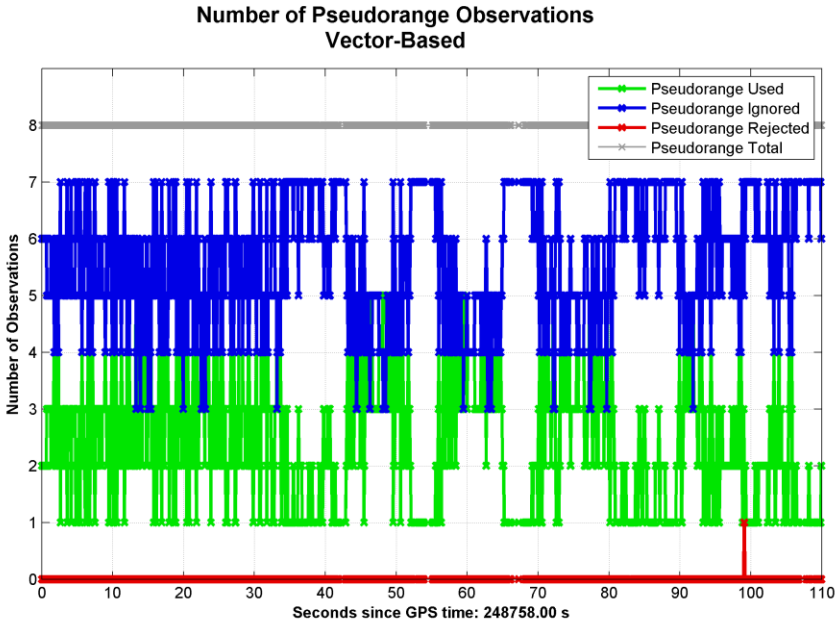

Figure 3.31: Pseudorange Availability for Vector-Based Receiver (Basement)

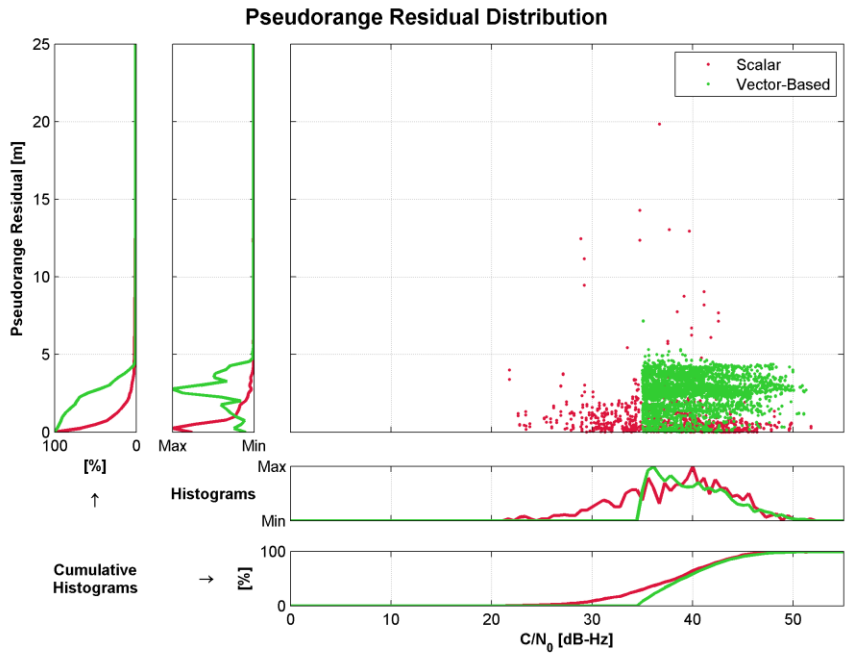

Figure 3.32: Pseudorange Residual Distribution (Basement)

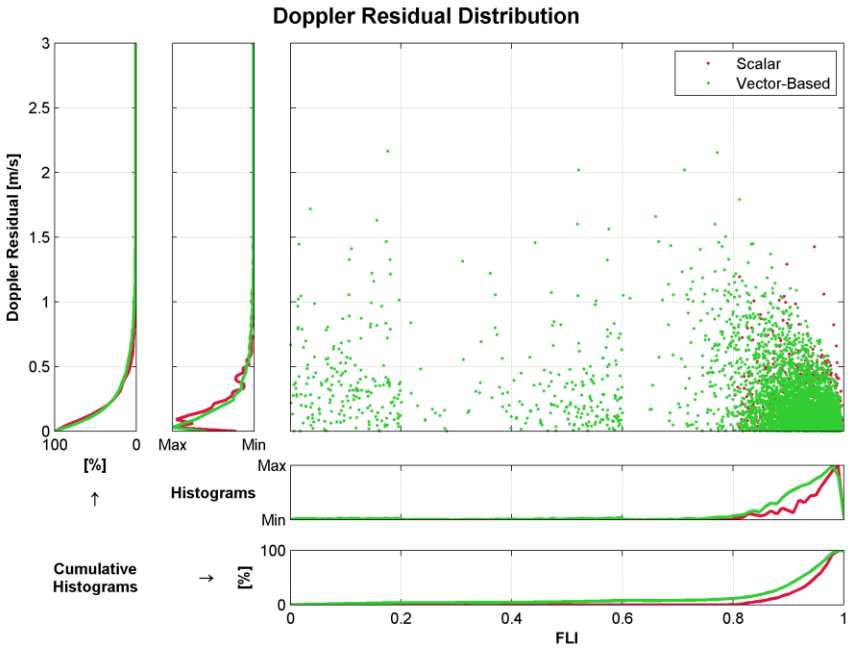

Figure 3.33: Doppler Residual Distribution (Basement)

3.3.2 Navigation Performance

In the following subsections, the availability and accuracy of the navigation solution from the scalar and vector-based receiver is examined. Similar to the evaluation of tracking performance and observation quality presented earlier in this chapter, analysis of the navigation performance for the two receivers is broken up into the four operating environments within a timber-framed house. The evaluation of the navigation performance is based on the solution availability and accuracy.

3.3.2.1 Navigation Solution Availability

In this section, the availability of navigation solution updates is compared between the scalar and vector-based receivers. Since both receivers have 100% availability while operating outside and on the ground floor of the timber-framed house, their plots are not presented in this section. Figure 3.34 show the availability of navigation solution updates as the scalar and vector-based receivers transition from ground level to the basement. The upper subplot in Figure 3.34 shows the availability of navigation solution updates over time while the lower two subplots give an indication of the overall availability over the entire period. Based on this figure, it is possible to see that as the receiver descends down to the basement, the scalar receiver loses the ability to generate navigation solution updates slightly earlier than the vector-based receiver. Moreover, while the vector-based receiver was able to provide intermittent solution updates over the final 14 seconds of this period, the scalar receiver was unable to generate any solution updates. This resulted in an increase of roughly 15% in availability for the vector-based receiver as compared to the scalar receiver.

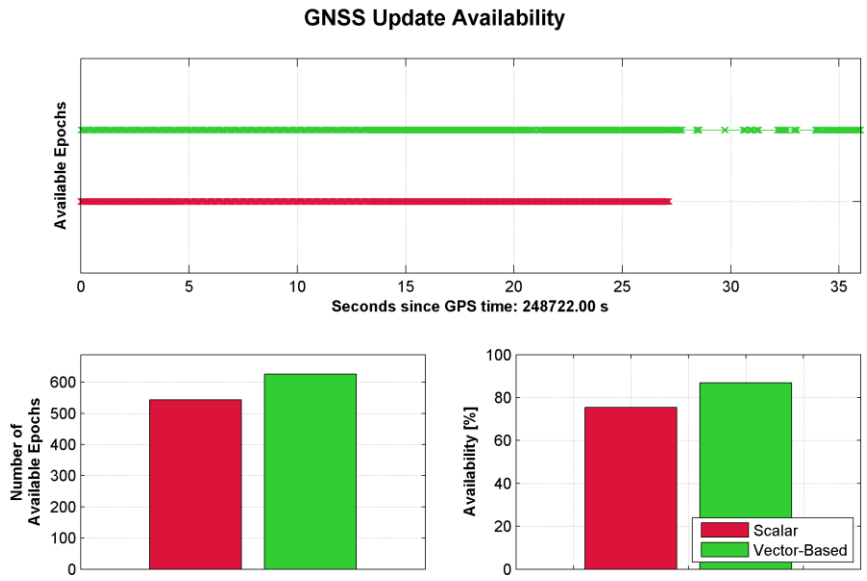

Figure 3.34: Navigation Solution Availability (Descending to Basement)

As the user enters the basement, the navigation solution availability for the two receivers become even more dissimilar; Figure 3.35 shows the solution availability of the two receivers for the period spent in the basement. Here, the vector-based GNSS receiver is capable of providing solution updates 90% of the time while the scalar receiver was only able to provide a navigation solution update slightly over 40% of the time. Comparing the two receiver architectures, it is possible to show that for environments found in the basement of a timber-framed house, the vector-based receiver can improve the navigation solution availability by approximately 100%. As impressive as this may be, the accuracy of the navigation solutions are also important; this is examined in the following subsection.

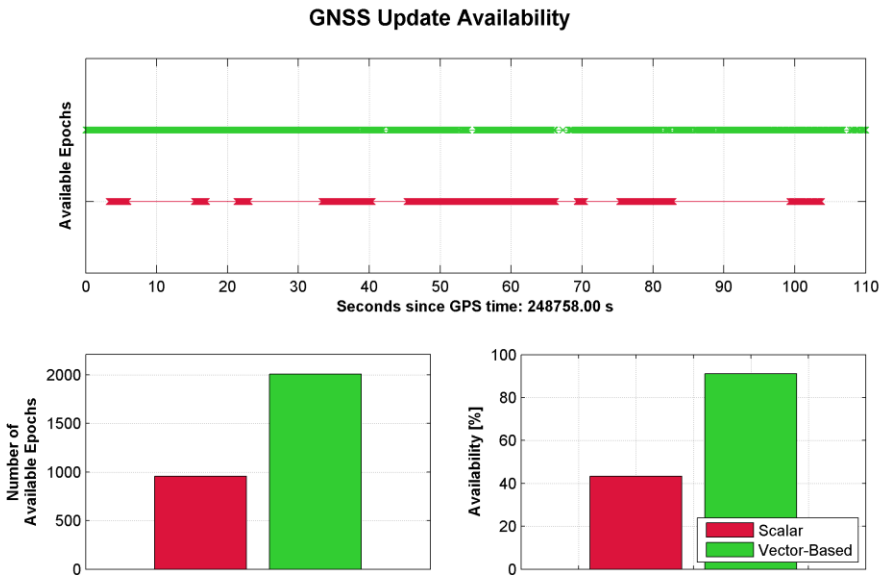

Figure 3.35: Navigation Solution Availability (Basement)Navigation Accuracy

The accuracy of the navigation solutions generated by a scalar and vector-based GNSS receiver are assessed in this section. Similar to prior subsections found in this chapter, the navigation accuracy for the two receivers are compared in four different operating environments found outside of, and within a traditional North American timber-framed house. In order to determine the position and velocity accuracy presented herein, the navigation solutions for the two receivers are compared to the reference navigation solution described in section 3.2.3.

Beginning with the outdoor environment, the position error over time and its statistics over the entire period are plotted for the northing, easting and vertical direction on Figure 3.36 and Figure 3.37. In an outdoor setting, the position error for both scalar and vector-

based receivers is quite similar and neither receiver appears to provide a clear improvement in overall positioning accuracy. However, upon viewing the velocity error statistic on Figure 3.38, it is possible to see that in general the vector-based receiver generated slightly more noisy velocity estimates as compared to the scalar receiver when operating outdoors; this is reflected in the higher standard deviation in the velocity errors.

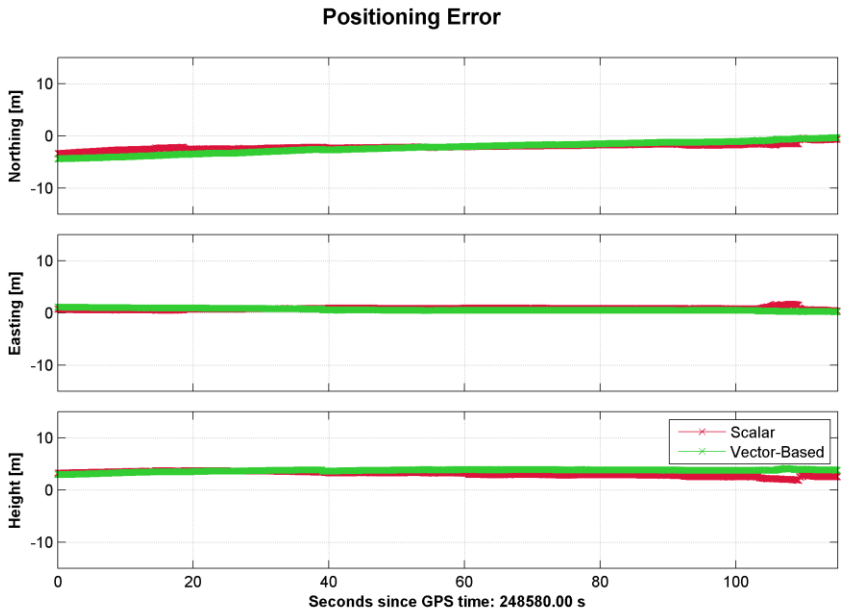

Figure 3.36: Position Error over Time (Outdoors)

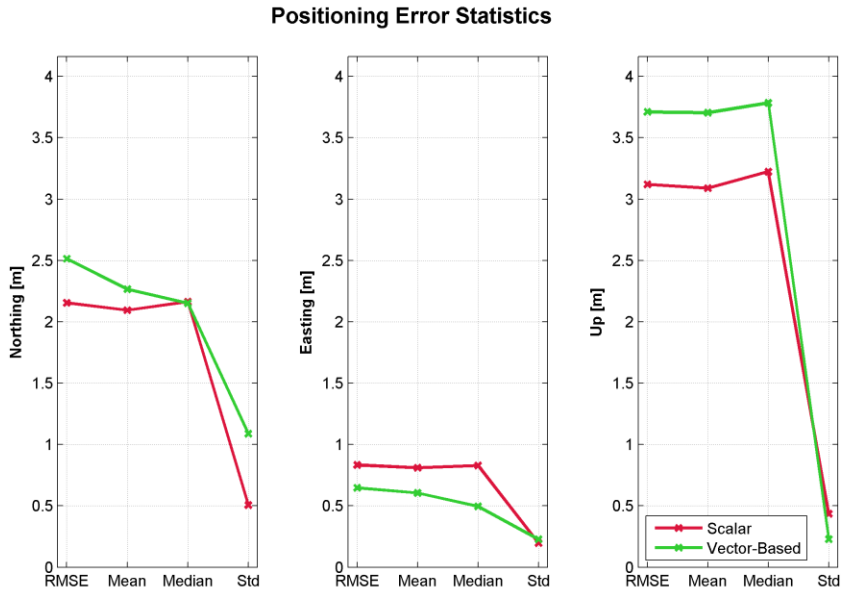

Figure 3.37: Position Error Statistics (Outdoors)

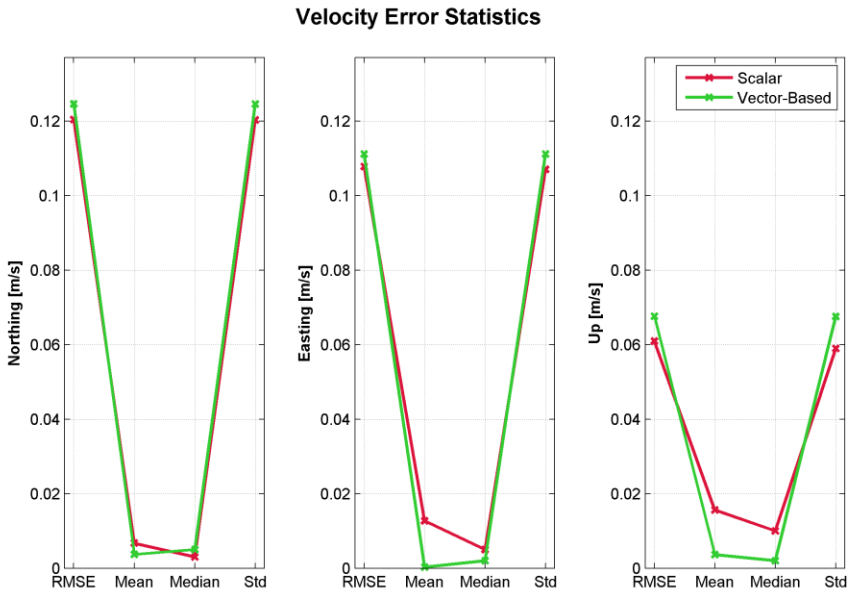

Figure 3.38: Velocity Error Statistics (Outdoors)

Upon moving indoors, the position and velocity accuracy for the vector-based receiver shows a clear improvement over the scalar receiver. This is most apparent in the easting direction where the positioning accuracy decreases dramatically between 6-12 seconds into the period shown on Figure 3.39. The large position errors observed during this period is also reflected in the position error statistics shown on Figure 3.40. Furthermore, contrary to the velocity errors observed in the outdoor environment, Figure 3.41 shows that the velocity errors of the vector-based receiver was noticeably lower in all directions as compared to the scalar receiver when operating on the ground level within the timber-framed house.

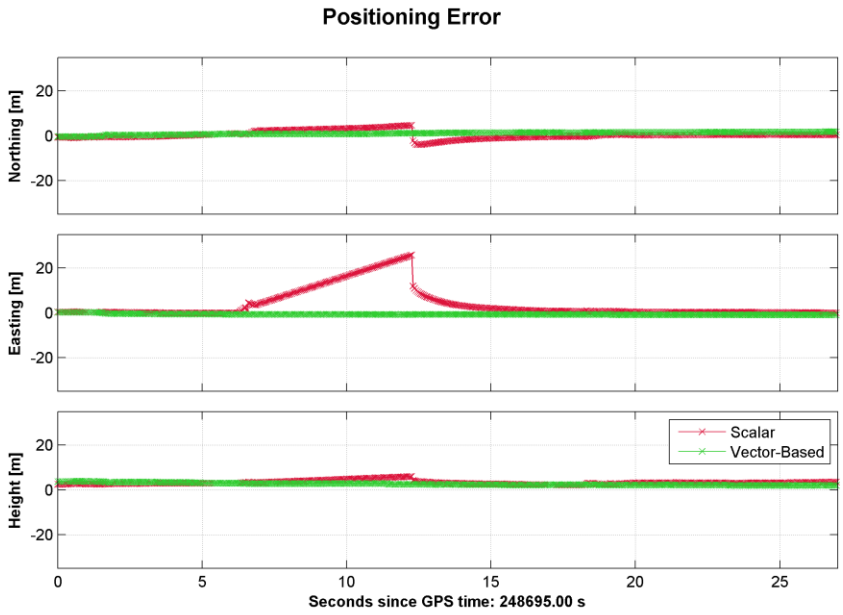

Figure 3.39: Position Error over Time (Upstairs)

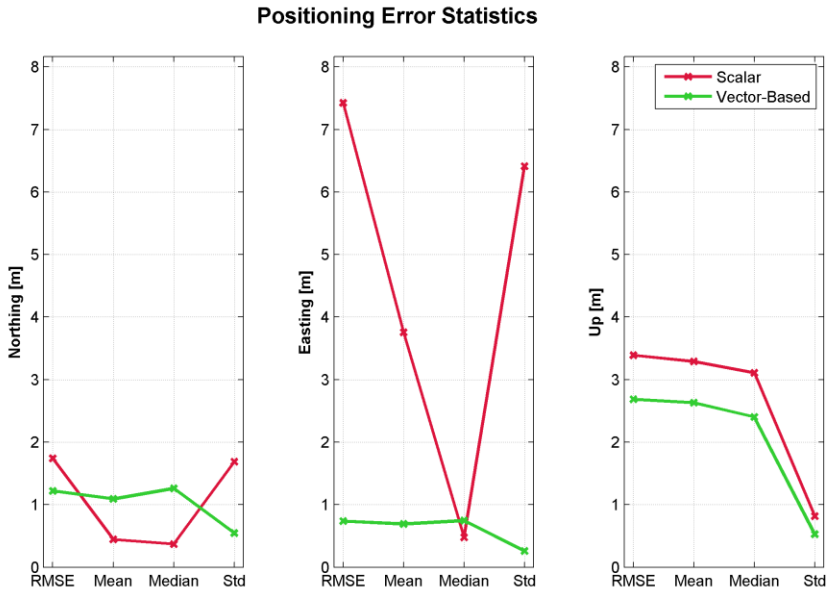

Figure 3.40: Position Error Statistics (Upstairs)

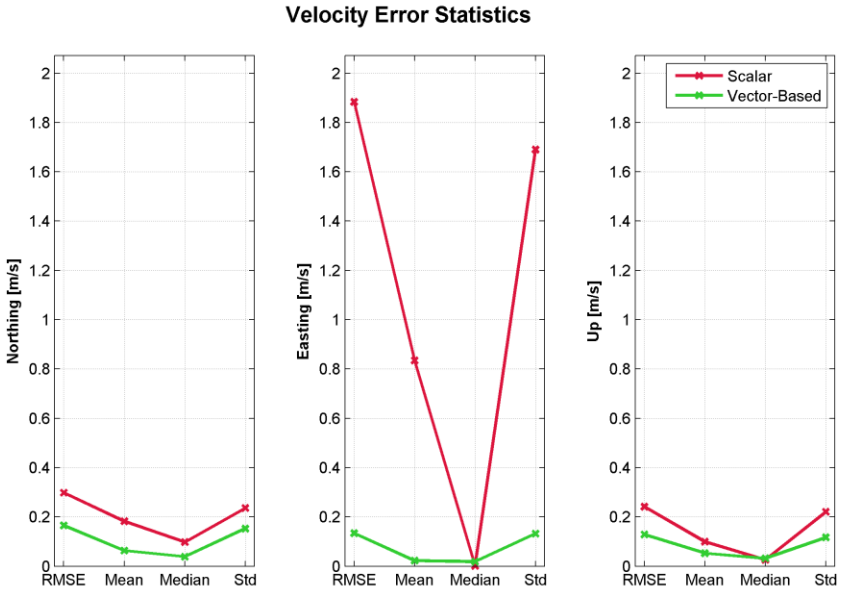

Figure 3.41: Velocity Error Statistics (Upstairs)

Figure 3.42 through Figure 3.44 shows the position and velocity error as the two receivers continue on and descend down to the basement. Here, the vector-based receiver architecture continues to demonstrate its effectiveness in not only providing a navigation solution during periods where the scalar receiver could not, but also in providing a more accurate navigation solution over the scalar receiver. Although the horizontal position accuracy between the two receivers is similar, the vertical positioning accuracy for the vector-based receiver showed a marked improvement. Furthermore, the velocity accuracy of the vector-based receiver was also found to be better than that of the scalar receiver during this period.

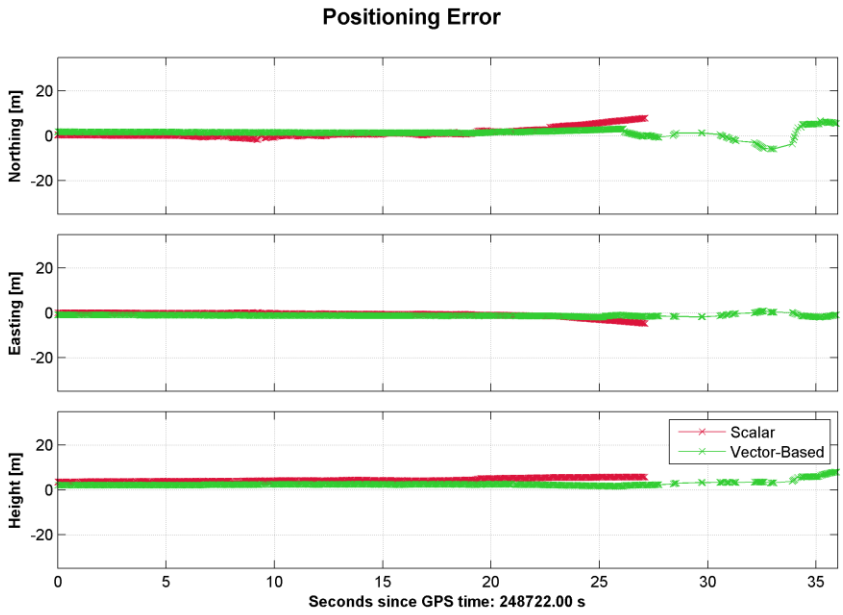

Figure 3.42: Positioning Error over Time (Descending to Basement)

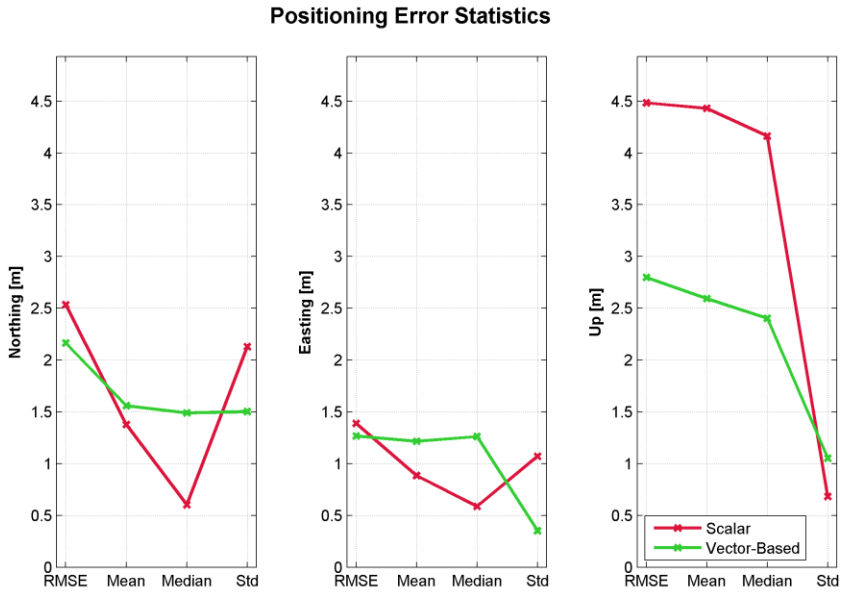

Figure 3.43: Positioning Error Statistics (Descending to Basement)

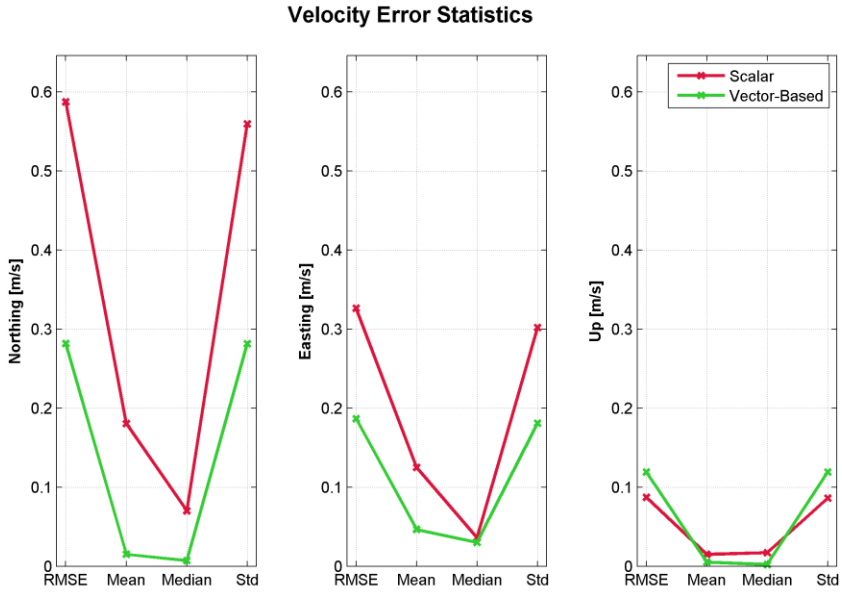

Figure 3.44: Velocity Error Statistics (Descending to Basement)

The position and velocity error for the scalar and vector-based receiver operating at the basement of the timber-framed house is shown on Figure 3.45 through Figure 3.47. It is immediately apparent from Figure 3.45 and Figure 3.46 that the positioning accuracy of the vector-based receiver greatly surpasses that of the scalar receiver. While in the basement, the vector-based receiver was able to maintain a positioning accuracy of better than 10 metres in the horizontal direction and better than 20 metres in the vertical direction. In contrast, the RMSE of the scalar receiver was greater than 90 metres in the northing direction. Once again, the vector-based receiver also had noticeably more accurate velocity estimates compared to that of the scalar receiver – this is clearly shown on Figure 3.47.

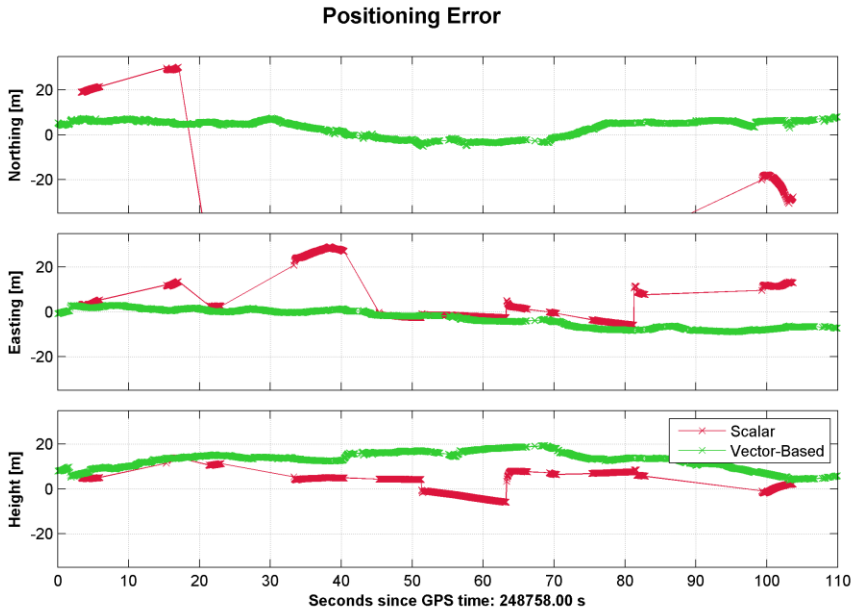

Figure 3.45: Position Error over Time (Basement)

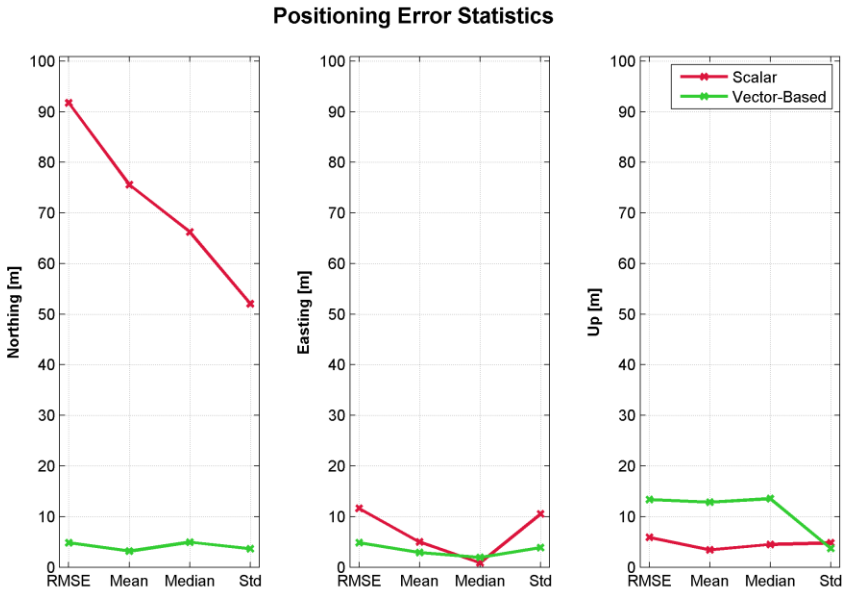

Figure 3.46: Position Error Statistics (Basement)

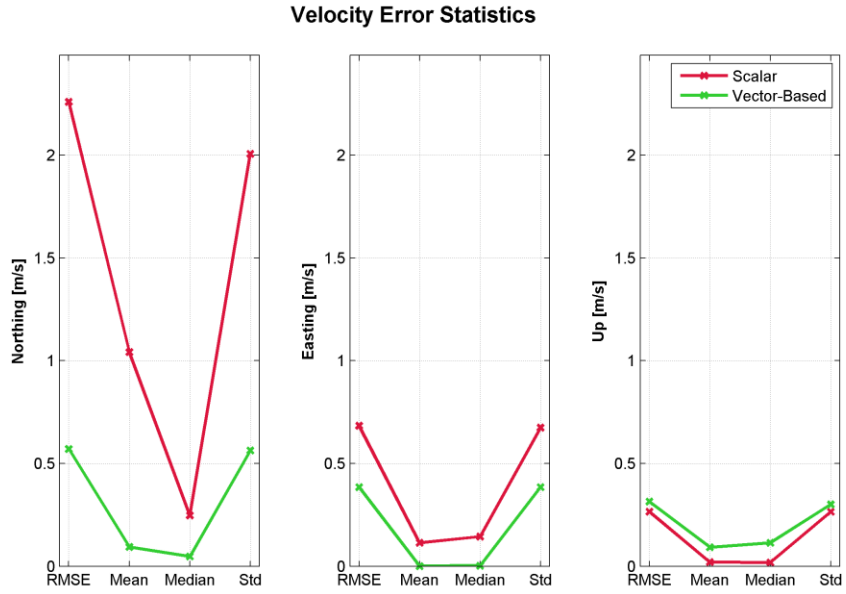

Figure 3.47: Velocity Error Statistics (Basement)

3.4 Conclusion

Results presented in this chapter demonstrate the benefits of employing a vector-based GNSS receiver architecture while operating in challenging signal environments like those found within a traditional North American timber-framed house. As discussed earlier in Section 2.3.6, the primary benefits of a vector-based receiver architecture is as follows:

- 6dB improvement in interference and jamming mitigation (Benson 2007)
- Increased signal tracking sensitivity to below 10 dB-Hz (Pany & Eissfeller 2006)
- Ability to bridge signal outages without the need for signal reacquisition (Pany & Eissfeller 2006)
- Ability to minimize the effects of signal dynamic stress caused by receiver motion (Hamm & Bevly 2005)

Although the effects of jamming was not investigated in this work, the results presented so far confirm that a vector-based GNSS receiver can provide improved tracking sensitivity, effective mitigation of brief signal outages, and improved tracking performance for dynamic receiver motion as compared to a scalar receiver.

By moving the scalar and vector-based GNSS receivers from outdoors, through the ground level portion of the house and down to the basement, it was possible to observe the operating limits of a traditional scalar tracking GNSS receiver. This provided an opportunity to observe the improvement in tracking sensitivity, observation quality, navigation availability and navigation accuracy that a vector-based GNSS receiver can achieve over a traditional scalar tracking receiver. However, the timber-house

environment used in this chapter was not capable of taking the vector-based receiver to its operating limits.

In the following chapters, a more challenging urban environment consisting of an urban canyon and a structure constructed out of concrete and glass will be used to explore the limits of the vector-based tracking receiver. Using this environment, DGPS and UWB augmentation techniques will be added to the vector-based GNSS receiver to examine how the performance of a vector-based GNSS receiver can be further improved using such augmentation techniques.

Chapter Four: Augmentation of a Vector-Based GNSS Receiver

4.1 Overview

This chapter covers the development of the navigation filter used to integrate DGPS corrections and UWB range measurements into the original vector-based receiver architecture. Also included is a discussion on the tuning of the Kalman filter used for determining the navigation solution. This is then followed by a thorough description of the environment and equipment setup used to test the augmented vector-based receiver.

4.2 Navigation Filter Development

For the work discussed herein, two major changes have been made to the navigation filter of GSNRx-vb^{TM} – a vector-based software GNSS receiver developed by the PLAN Group at the University of Calgary. These changes include the ability to incorporate DGPS corrections from a nearby GNSS receiver and the integration of UWB range measurements to nearby radios. The methodologies used and the algorithm development performed for this work is discussed in the subsections below.

4.2.1 Differential GNSS Corrections

The incorporation of differential corrections within a GNSS navigation solution is primarily done to remove systematic errors such as troposphere delay, ionosphere errors, satellite position errors and satellite clock errors observed by a standalone receiver. Removing systematic errors from GNSS measurements results in a more accurate navigation solution; as a result, the prediction of the line of sight signal parameters may also be improved in the vector-based receiver. Moreover, it should be mentioned that the

accuracy improvement when using differential GNSS corrections is most noticeable in the vertical direction.

When measurements from two different systems, such as GNSS and UWB, are used independently, they will naturally converge to two unique navigation solutions due to uncompensated systematic measurement errors. In the case of GNSS and UWB measurements, since the two systems operate independently from each other, their measurements are not generated at the same instances in time. Thus, in order to use measurements from both systems in a tightly-coupled navigation solution, the measurements from each system must be combined asynchronously. There is a drawback to this however; since uncompensated systematic errors in the measurements from each unique system may steer the navigation filter to different positions for a given epoch, alternating between GNSS and UWB measurements over short periods may cause transitory spikes in the velocity estimates. Since UWB range measurements are not time synchronized with GNSS observations, the navigation solution can only update the navigation solution when UWB ranges are available. If large systematic biases in the GNSS observations exist, the navigation solution will also be biased; on the other hand if UWB observations are free of the GNSS-specific systematic biases, an update of the navigation solution using the UWB observations may cause the navigation solution to jump. The resulting velocity errors in the navigation solution have the same effect as a frequency prediction error when the navigation solution is used to update a vector-based tracking as will be shown in Section 5.2.1. These velocity errors in the navigation

solution can have a noticeable (negative) impact in the signal tracking performance of a vector-based receiver.

For this work, the method used to generate GNSS corrections is similar to the methods used for Real-Time Kinematic (RTK) applications where the objective is to estimate the carrier-phase ambiguities to achieve sub-metre level positioning accuracy. In such scenarios, measurement corrections are generated by setting up a reference GNSS receiver at a known position. Because the position of the reference receiver is known, only the clock offset needs to be estimated. The resulting observation residuals from the navigation solution in the reference receiver then consist of measurement errors due to both systematic errors such as tropospheric delay, ionosphere errors, satellite clock and position errors, as well as random errors such as receiver noise and multipath. Unlike more sophisticated corrections-based algorithms such as those employed for Wide Area Augmentation Service (WAAS) (Federal Aviation Administration 2008), the reference receiver used in this work does not attempt to estimate or isolate the systematic errors from the observed residuals. Thus, the corrections generated by the reference receiver include random processes such as receiver noise and multipath that do not contribute to the reduction of systematic measurement errors, but rather, may contribute to an increase in random errors for nearby receiver that make use of the corrections.

To generate GNSS corrections for nearby receivers, a GNSS antenna located in an outdoor environment is used for obtaining pseudorange measurements. Signals from the antenna are fed through a low-noise amplifier (LNA) and an RF front-end in order to

amplify, sample, and digitize the incoming signals. A vector-based software GNSS receiver was then used to track the incoming signals and estimate the measurement errors in the observations; this receiver is referred to as the *reference* receiver. Nearby receiver(s) that make use of the measurement corrections generated by reference receiver is/are referred to as the *rover* receiver(s).

As discussed in Chapter 2, pseudorange measurements can be modelled in the form

$$\rho_r^s = R_r^s + \varepsilon_{orbit}^s \cdot u_r^s + \delta_{tropo}^s + \delta_{iono}^s + \delta_{multipath,r}^s + c(\delta T_{satellite}^s + \delta T_{receiver,r}) + \varepsilon_{noise,r} \tag{4.1}$$

where ρ_r^s is the observed pseudorange between receiver r and satellite s, R_r^s is the geometric range between the receiver and satellite, $\varepsilon_{orbit}^s \cdot u_r^s$ is the absolute orbital positioning error, ε_{orbit}^s, projected onto the line-of-sight unit vector u_r^s from the receiver to the satellite, δ_{tropo}^s and δ_{iono}^s are the delay caused by the troposphere and ionosphere $\delta_{multipath,r}^s$ is multipath delay, c is the speed of light, $\delta T_{satellite}^s$ and $\delta T_{receiver,r}$ are the satellite and receiver clock errors, and $\varepsilon_{noise,r}$ is the receiver noise (Conley et al 2006a). By collecting the error terms, with exception of the receiver clock error, equation (2.20) can be rewritten in the form

$$\rho_r^s = R_r^s + c\delta T_{receiver,r} + \varepsilon_{measurement\ errors,r}^s \tag{4.2}$$

where $\varepsilon^{s}_{measurement\ errors,r}$ is the sum of all measurement errors observed between receiver r and satellite s. Since the reference receiver is statically positioned at a known location and the satellite position and velocity can be determined using the broadcast ephemeris, both the geometric range and range rate between the reference receiver and all satellites being tracked can be computed directly. Therefore, the only states that needs to be estimated is the receiver clock offset and drift. To estimate the clock terms, an extended Kalman filter similar to the one discussed in Chapter 2 is used. The primary difference in this case is that the state vector for the navigation solution, shown in equation (4.3), only contains $c\delta T_{receiver,r}$ and $c\delta \dot{T}_{receiver,r}$ representing the receiver clock offset and drift, respectively.

$$x = \begin{bmatrix} c\delta T_{receiver,r} \\ c\delta \dot{T}_{receiver,r} \end{bmatrix} \tag{4.3}$$

Based on the system model shown in equation (4.2), a first-order Taylor series expansion for the pseudorange and Doppler measurements observed at a predetermined location and velocity can be expressed as

$$\begin{aligned} \rho^{s}_{r} - R^{s}_{r} &\approx c\delta T_{receiver,r} \\ \dot{\varphi}^{s}_{r} - \dot{R}^{s}_{r} &\approx c\delta \dot{T}_{receiver,r} \end{aligned} \tag{4.4}$$

and the partial derivative of the pseudorange and Doppler observation becomes

$$\begin{aligned} \partial\rho_r^s &\approx 1 \\ \partial\dot{\varphi}_r^s &\approx 1 \end{aligned} \tag{4.5}$$

where $\delta\rho_r^s$ and $\delta\dot{\varphi}_r^s$ are the partial derivative of the pseudorange and Doppler observation between receiver r and satellite s. From equation (4.5), the design matrix H can be written as:

$$\begin{aligned} &\begin{bmatrix} \delta\rho_r^1 \\ \vdots \\ \delta\rho_r^n \end{bmatrix} = \begin{bmatrix} 1 \\ \vdots \\ 1 \end{bmatrix} \begin{bmatrix} \Delta c dT \end{bmatrix} \\ &\delta\rho_r = H_\rho \Delta x_\rho \\ &\begin{bmatrix} \delta\dot{\varphi}_r^1 \\ \vdots \\ \delta\dot{\varphi}_r^n \end{bmatrix} = \begin{bmatrix} 1 \\ \vdots \\ 1 \end{bmatrix} \begin{bmatrix} \Delta c d\dot{T} \end{bmatrix} \\ &\delta\dot{\varphi}_r = H_{\dot{\varphi}} \Delta x_{\dot{\varphi}} \end{aligned} \tag{4.6}$$

The transition matrix $\Phi_{k,k+1}$ for predicting the clock offset cdT and drift $cd\dot{T}$ in the state vector $\hat{x}$ over the time interval ΔT is expressed as:

$$\begin{aligned} &\begin{bmatrix} cdT_{k+1}^- \\ cd\dot{T}_{k+1}^- \end{bmatrix} = \begin{bmatrix} 1 & \Delta T \\ 0 & 1 \end{bmatrix} \begin{bmatrix} cd\hat{T}_k \\ cd\hat{\dot{T}}_k \end{bmatrix} \\ &\hat{x}_{k+1}^- = \Phi_{k,k+1} \hat{x}_k \end{aligned} \tag{4.7}$$

Weighting of the pseudorange and Doppler observations is performed based on the satellite elevations

$$R = \sigma_o^2 \begin{bmatrix} \frac{1}{\sin(\varepsilon^1)} & 0 & 0 \\ 0 & \ddots & 0 \\ 0 & 0 & \frac{1}{\sin(\varepsilon^n)} \end{bmatrix} \tag{4.8}$$

where R is the observation weight matrix, ε^n is the elevation corresponding to the nth satellite observation and σ_o^2 is the a priori variance of the observations. Here, the standard deviation of pseudorange and Doppler observations are assumed to be 5 metres and 0.2 Hz respectively.

The oscillator frequency noise error model (NovAtel Inc. 2005) used for the clock states is given by

$$S_y(f) = \frac{S_r}{f^2} + \frac{S_f}{f} + S_w \tag{4.9}$$

where $S_y(f)$ is the clock's power spectrum, S_w, S_f, and S_r represent the power spectral density values of the oscillator white frequency noise, flicker frequency noise,

and random walk frequency noise, and f is the sampling frequency. The corresponding process noise matrix for this oscillator model is given by

$$Q = \begin{bmatrix} q_{11} & q_{12} \\ q_{21} & q_{22} \end{bmatrix} = \begin{bmatrix} \frac{S_w \Delta t}{2} + 2S_f \Delta t^2 + \frac{2\pi^2 S_r \Delta t^3}{3} & S_f \Delta t + \pi^2 S_r \Delta t^2 \\ S_f \Delta t + \pi^2 S_r \Delta t^2 & \frac{S_w}{2\Delta t} + 4S_f + \frac{8\pi^2 S_r \Delta t}{3} \end{bmatrix} \quad (4.10)$$

where q_{11} represent the increase in variance on the clock offset, q_{12} and q_{21} represent the increase in clock offset and clock drift covariance, and q_{22} represent the increase in variance on the clock drift due to errors in the state prediction model. The spectral density values used represent the characteristics of a Voltage-Controlled Temperature-Compensated Crystal Oscillator and are shown on Table 4.1.

Table 4.1: Spectral Density Values for Oscillator Frequency Noise

Voltage Controlled Temperature Compensated Crystal Oscillator (VCTCXO) Noise Model	
S_w	1.0^{-21} $(\text{Hz}/\sqrt{\text{Hz}})$
S_f	1.0^{-20} $(\text{Hz}^2/\sqrt{\text{Hz}})$
S_r	1.0^{-20} $(\text{Hz}^3/\sqrt{\text{Hz}})$

Upon estimating the receiver clock terms for a given epoch, the pseudorange residuals are used to form the pseudorange observation corrections for nearby receivers. By inspecting equation (4.2), it becomes apparent that, once the geometric range R between a receiver

and satellite is known and the receiver clock offset has been estimated, what remains in the residuals are the measurement errors. These measurement errors include the troposphere delay, ionosphere errors, satellite position error, multipath, and receiver noise.

It is important to bear in mind that any error components that are common between all pseudorange measurements will be absorbed into the receiver clock offset term and will not appear in the residuals from the reference receiver. For instance, all pseudorange observations will, to some degree, experience a troposphere delay but low elevation satellite observations will experience a larger delay. As such, the amount of troposphere delay that is common between all satellites will not appear in the corrections; however, the extra troposphere delay found on low elevation satellite observations are not absorbed in the clock offset term but will appear in the residuals and correspondingly, the pseudorange corrections generated by the reference receiver.

4.2.2 Ultra Wide-band Augmentation

As discussed in Chapter 2, UWB range measurements can be used to augment GNSS observations in an effort to improve the accuracy of the navigation solution. Note that in order to augment a GNSS navigation solution with UWB range measurements, the GNSS navigation solution must first be computed to initialize the navigation filter. There are several reasons for this, the first is because the UWB range measurement are time tagged using GPS time and thus a GNSS solution is required to determine the receiver's time so that incoming UWB range measurements can be time aligned with the navigation

solution. Secondly, due to the limitations of the MSSI UWB radios used for this research, range measurements can only be made between one radio pair at any given time. Because of this, no single measurement epoch will contain the number of UWB range measurements required to perform a least squares adjustment and obtain the receiver position while the receiver is in motion; therefore a GNSS solution is required.

Within the modified vector-based software receiver used, UWB range measurements are treated similarly to GNSS pseudorange measurements in that a UWB range measurement is always associated with the position of the radio that is being ranged to – the responder radio location. The responder radio position plays the same role as that of the ephemeris which allows a GNSS receiver to determine the position of a satellite at the time of transmission for any given observation. With regards to the modelling of systematic errors specific to UWB range measurements, a scale factor and bias of each ranging pair is determined beforehand and a correction is applied to the observations before they are used by the navigation filter. This correction is shown below

$$R_{corrected} = S \cdot (R_{uncorrected} + B) \tag{4.11}$$

where $R_{corrected}$ is the corrected range observation, S is the scale factor, $R_{uncorrected}$ is the uncorrected range measurement, and B is the ranging bias. To determine the scale factor and bias terms, observed UWB range measurements were plotted and compared with the ranges computed using the receiver's reference trajectory and the responder radios'

position. A scale factor and bias term for each radio pair was then chosen to match the observed range measurements to that of the computed reference ranges.

As mentioned earlier in this chapter, UWB range measurements are not assumed to be synchronized with GNSS measurements within the vector-based software receiver. Therefore, GNSS and UWB measurements are processed in an asynchronous manner by the extended Kalman filter that is used to update the navigation solution. This allows GNSS and UWB measurements to be used without any need to interpolate UWB observations so that they can be time synchronized with GNSS measurement epochs. This aspect is important since prolonged UWB outages can greatly reduce the accuracy of the interpolated UWB observations and lead to gross errors in the navigation solution.

By making use of UWB measurements in a vector-based GNSS receiver, the navigation solution accuracy can be improved in several ways. First, the addition of UWB ranging measurements increases the frequency of navigation solution updates; this means that when there are periods where GNSS measurements are not available, the navigation solution can still be updated using UWB measurements. Second, the use of UWB ranging measurements can improve the accuracy and reliability of the navigation solution since the accuracy of UWB ranges measurements are typically better than that of pseudorange measurements while in high multipath environments. Furthermore, depending on the relative position between nearby UWB radios and the receiver of interest, the geometry of UWB range and GNSS pseudorange measurements can be enhanced. Due to the vector-based architecture, the improvement in navigation solution accuracy, reliability,

and update frequency afforded by the augmentation of UWB measurements allows the NCO to generate local replica GNSS signals that better match the incoming line of sight signals. This, in turn, improves the GNSS signal tracking sensitivity and measurement availability.

4.2.3 Observation Pre-filtering

One challenge of navigation in degraded signal environments is a need to determine whether a measurement is of sufficient quality. In GNSS receivers, a classical approach is to reject satellites below a given elevation since low elevation satellites tend to have larger errors due to troposphere delay, ionosphere errors and multipath. However, since tracking statistics are available, C/N_0 and FLI values can be used to gauge the code and frequency tracking performance of the tracking loop (Aminian 2011). This, in turn, can provide an indication of the quality of the pseudorange and Doppler measurements. An example of this is shown in Figure 4.1 where one can see a clear correlation between the C/N_0 and the size of pseudorange residuals observed by a GNSS receiver operating in the basement of a timber-framed house. As the C/N_0 of observations decreases, the spread in observation residuals tend to grow on the scalar receiver.

What is also apparent in Figure 4.1 is that the vector-based receiver does not have any residuals with a C/N_0 that is less than 35 dB-Hz. This is due to the observation pre-filtering whereby the navigation filter within the receiver will not make use of pseudorange observations with a C/N_0 below 35 dB-Hz. By applying such pre-filtering

techniques, it is possible to reduce the risk of updating the navigation solution with observations that may introduce errors due to undetected blunder observations.

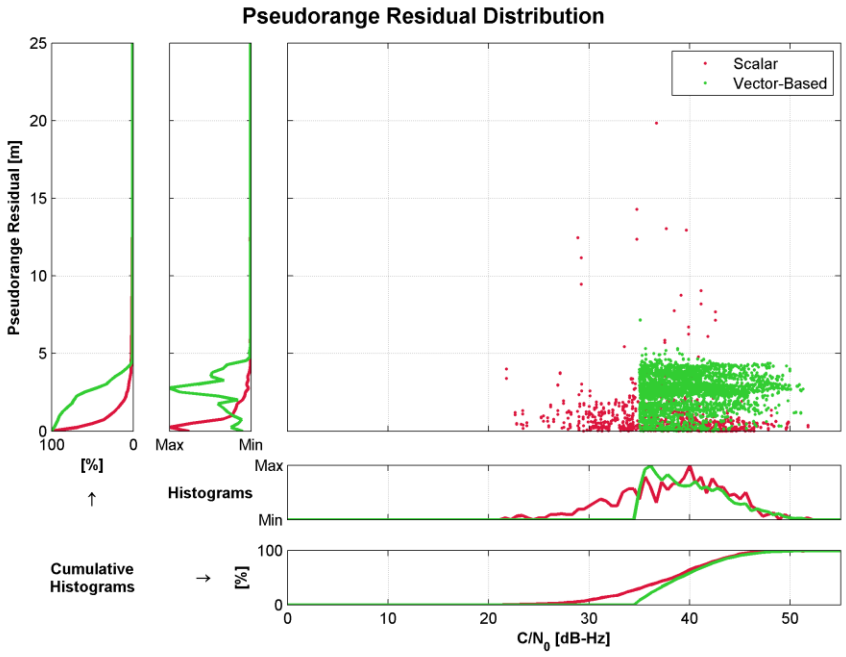

Figure 4.1: Pseudorange Residual Distribution (Timber House Basement)

Unlike GNSS observations where C/N_0 and FLI values can be used as a measure determining the quality of a measurement, the MSSI radios used for obtaining UWB measurements did not provide any Signal to Noise Ratio (SNR) or Received Signal Strength Indication (RSSI) readings that are typically used as a measure of quality for radio transmissions. However, the MSSI radios do make up to 16 individual range measurements between a single radio pair for every UWB measurement epoch. Because of this, the variance in the range measurements that are common to a given epoch can be

used to detect the presence of poor quality observations. To this end, a method of prefiltering poor quality or unreliable measurements was devised.

To ensure that UWB range measurements used in the navigation filter were reliable, the following criterions must be met:

1. At least two range measurements must be made for any given epoch so that the variance of all range measurements made for an epoch can be computed
2. The standard deviation between all available range measurements in a single epoch must be less than 0.50 metres
3. The maximum range observation cannot exceed 45 metres to ensure that gross measurement errors are removed

Once a set of UWB range measurements have met the above criterions, all available range measurements corresponding to a given epoch are averaged to form a single range observation. This, in turn, is fed to the extended Kalman filter and is used to update the navigation solution of the receiver. Similar to a traditional vector-based GNSS receiver, when new UWB measurements are available, the navigation solution is updated and this new navigation solution is used in updating the local signal generation for all the GNSS tracking loops.

4.2.4 Kalman Filter Tuning

A key operating principle of Kalman filters is that, in order to function properly, uncertainty from the state prediction model must be weighed with uncertainty in new

observations. The state prediction model – also commonly referred to as a dynamics model – take state information from past epochs and uses it to predict the states for a future epoch. Inherently, errors in the dynamics model mean that the predicted states are never completely accurate; therefore the increased uncertainty in the states due to errors in prediction is accounted for by adding a process noise model to the filter. This process noise increases the uncertainty of the predicted states by inflating the variance terms in the state variance-covariance matrix. Correspondingly, when new observations are available, information provided by the observations are weighted based on their quality by means of an observation variance-covariance matrix. This observation variance-covariance matrix determines the amount of information that an observation can contribute in the estimation of the states.

Kalman filter tuning is a balancing act that weighs the confidence in the dynamics model used to predict a navigation solution into the future, and the amount of influence that new observations have in changing the navigation solution during a Kalman filter update. Since the process noise model describes the increase in uncertainty for a navigation solution's prediction, it needs to accurately reflect the variability in motion that a receiver experiences during its normal operation. The process noise model for the state vector used for the work herein is a random walk velocity model shown below

$$Q = \begin{bmatrix} \frac{S_{\dot{E}}\Delta t3}{3} & 0 & 0 & \frac{S_{\dot{E}}\Delta t^2}{2} & 0 & 0 & 0 & 0 \\ 0 & \frac{S_{\dot{N}}\Delta t3}{3} & 0 & 0 & \frac{S_{\dot{N}}\Delta t}{2} & 0 & 0 & 0 \\ 0 & 0 & \frac{S_{\dot{U}}\Delta t3}{3} & 0 & 0 & \frac{S_{\dot{U}}\Delta t^2}{2} & 0 & 0 \\ \frac{S_{\dot{E}}\Delta t^2}{2} & 0 & 0 & S_{\dot{E}}\Delta t & 0 & 0 & 0 & 0 \\ 0 & \frac{S_{\dot{N}}\Delta t^2}{2} & 0 & 0 & S_{\dot{N}}\Delta t & 0 & 0 & 0 \\ 0 & 0 & \frac{S_{\dot{U}}\Delta t^2}{2} & 0 & 0 & S_{\dot{U}}\Delta t & 0 & 0 \\ 0 & 0 & 0 & 0 & 0 & 0 & q_{11} & q_{12} \\ 0 & 0 & 0 & 0 & 0 & 0 & q_{12} & q_{22} \end{bmatrix} \quad (4.12)$$

where $S_{\dot{E}}$, $S_{\dot{N}}$ and $S_{\dot{U}}$ are the spectral density values for the east, north and up velocity, ΔT is the time interval in which the states are being predicted forward since the last Kalman filter update, q_{11}, q_{12}, q_{21} and q_{22} represent the elements of a VCTCXO noise model found in equation (4.10). For the results presented in this research, the horizontal and vertical velocity spectral density value used is $1\,\mathrm{m/s^2/\sqrt{Hz}}$ and $0.5\,\mathrm{m/s^2/\sqrt{Hz}}$, respectively. These values describe the variability in velocity typical for pedestrian motion.

One critical aspect of the navigation filter tuning in a vector-based receiver is that, unlike a scalar tracking receiver, the navigation solution of a vector-based receiver has a direct influence on the performance of the GNSS signal tracking loops. In the case of the scalar

receiver, if the navigation filter is left loosely constrained, the only primary consequence of this is that the navigation solution will become less precise and appear noisier. The tracking loops on a scalar receiver remain stable since each loop functions independently from the rest of the system. In a vector-based receiver however, a loosely constrained navigation filter will negatively impact the tracking performance of the receiver as a whole due to an increase in both positioning, velocity, and clock estimation error; these errors translate into poorly predicted Doppler and code-phase estimates used in the NCO. As a result, the stability of all tracking loops are compromised and the receiver may lose lock on all signal being tracked. Therefore, in a vector-based receiver, it is imperative that the Kalman filter process noise models accurately reflect the motion that is expected for the intended application.

4.3 Testing Methodology

The following subsection describes the environment and equipment used to test the GNSS receiver architecture developed for this research. Results obtained from the testing environment described below are presented in Chapter 5.

4.3.1 Test Environment

The data used for evaluating UWB and DGPS aiding techniques in vector-based GNSS receivers was collected on July 6th, 2011 at the University of Calgary campus and is shown in Figure 4.2. This test environment consists of two areas which are discussed in greater detail in sections 4.3.1.1 and 4.3.1.2:

1) An outdoor area denoted using a yellow box

2) A light-indoor environment denoted using a red box

The green line shown on Figure 4.2 represents the reference trajectory for the receiver of interest that is being evaluated. As can be seen from this figure, the GNSS receiver is first initialized outside in order to acquire the necessary ephemeris information needed to obtain its position. Once the receiver position is available, the vector-tracking capabilities of the receiver can then be enabled to predict the incoming signal based on the relative motion of the receiver and the available satellites. Following this, the receiver is brought indoors to evaluating the performance of UWB and DGPS aiding under a light-indoor environment.

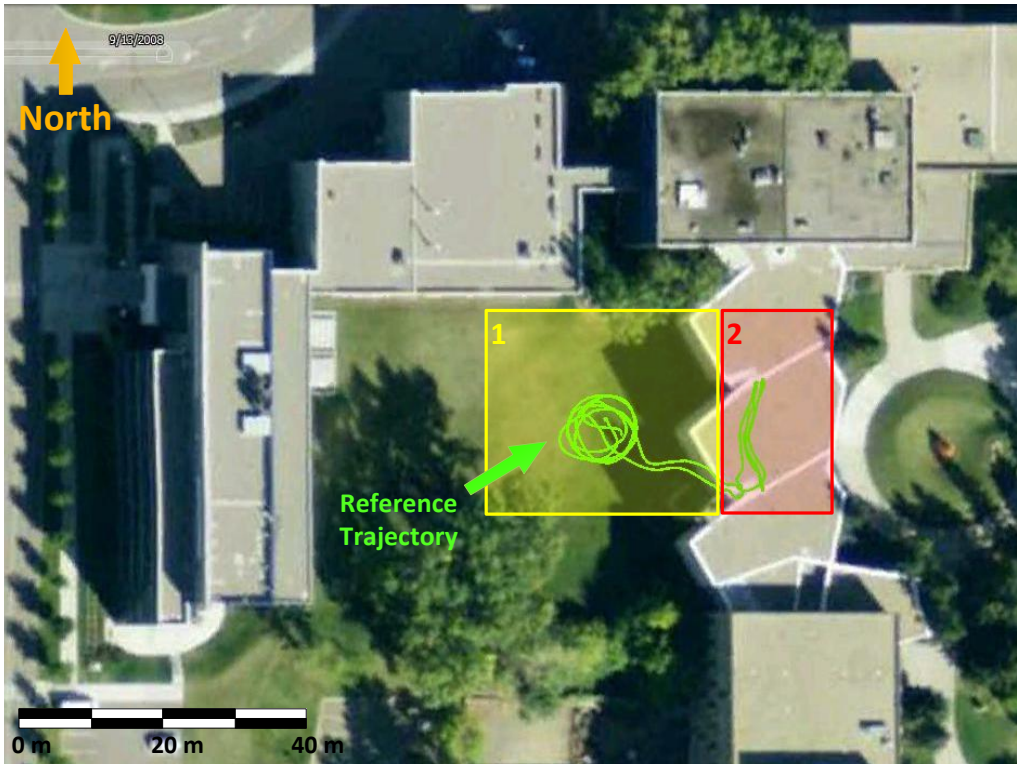

Figure 4.2: Urban Test Environment

4.3.1.1 Outdoor High-Multipath Environment

The outdoor test area shown in Figure 4.2 is located in a courtyard between the four story Calgary Centre for Innovative Technology (CCIT) building positioned to the west of the courtyard and the three story University of Calgary's Schulich School of Engineering building's E-block positioned on the east side of the courtyard. To the north of the courtyard is a two story link that connects the CCIT building to the Engineering building; located to the south are several large, mature, deciduous trees with summer foliage.

As can be seen on Figure 4.3, the CCIT building represents a formidable challenge for GNSS receivers for two reasons. The metallic panelling on the outside of the CCIT building has the potential to generate very strong specular multipath signals; moreover, the building also masks a significant portion of the sky – approximately 30 degrees from the horizon. Also, shown on the left portion of Figure 4.3 are several large, mature trees which are located directly south of the courtyard. These trees serve to attenuate GNSS signals for low lying satellites that traverse the southern sky.

Figure 4.4 shows the link that connects the CCIT building with the engineering building located to the north of the courtyard. Although there are no GPS satellites that are positioned directly to the north for the courtyard due to the location of Calgary, the two story link can serve to generate significant multipath signals for satellites located to the south of the courtyard.

Figure 4.3: South-West Facing View of CCIT Building

Figure 4.4: North-West Facing View of CCIT Building

Figure 4.5 below shows an east facing view of the Engineering building from the courtyard test area. From this figure, it is possible to see that the building presents several

key challenges for GNSS receivers. One of the main challenges is the sky obstruction that the building presents; similar to the CCIT building, the Engineering Building's E-block creates an elevation mask of approximately 30 degrees directly to the east of the courtyard. Moreover, flat concrete surfaces also serve to create strong, specular multipath signals that can result in large pseudorange observation errors. Lastly, the irregular, yet right-angled geometry of the Engineering Building's E-block can serve to generate complex multipath signals that are not strictly limited to GNSS satellites located in the eastern sky, but across a broad range of azimuths.

Figure 4.5: East Facing View of Engineering Lounge

It should also be noted that a GNSS antenna is mounted on the yellow tripod found on Figure 4.3 and Figure 4.5; the GNSS signals from this antenna is used to generate DGPS corrections discussed later in this chapter. Figure 4.4 shows a separate tripod that has

both a GNSS antenna as well as a UWB radio used for aiding the mobile receiver. The GNSS antenna is used in combination with a survey grade GNSS receiver to obtain a reference position for the UWB radio. A second tripod (not shown) with a similar setup is also placed in the courtyard to provide UWB range measurements from a different location.

From the figures shown in this section, it is apparent that the courtyard environment presents two major challenges for GNSS navigation; the tall buildings that encompass the courtyard masks approximately 30 degrees of the sky in the east and west direction, these buildings also generate significant multipath signals from a broad range of directions.

4.3.1.2 Light-Indoor Environment

The indoor testing environment was performed in the Engineering Lounge at the University of Calgary Schulich School of Engineering building's E-block and is highlighted in yellow on Figure 4.2. This location was chosen due the presence of large west-facing windows that allow the UWB ranging radios located outside to range with the receiver of interest while it is indoors.

Although the Engineering Lounge has large windows that may allow for UWB and non-line of sight GNSS signals to enter with relatively low attenuation, the level directly above the Engineering Lounge includes several large lecture halls and a large hallway. Because of this, any direct line-of-sight GNSS signals that penetrate to the ground floor are expected to be extremely weak. This presents a significant challenge for vector-based

GNSS receivers since the vector-tracking loops tend to ignore potentially stronger multipath signals while it attempts to track the line-of-sight signal which, in this scenario, is severely attenuated. Because of the strong attenuation due to the upper levels of the Engineering building, this environment is considered to be a light-indoor area for GNSS positioning.

It is also important to note that as the receiver moves from the outdoor courtyard area into the Engineering Lounge, this transition from an outdoor to an indoor environment is not clearly defined. As can be seen on Figure 4.5 and Figure 4.6, a large overhang exists above the Engineering Lounge entrance. Also shown on Figure 4.6 is a yellow tripod located to the right of the image; a UWB radio is mounted on this tripod to provide UWB ranging measurements from an indoor location. The position of the UWB radio shown on Figure 4.6 was obtained by surveying the point using a total station.

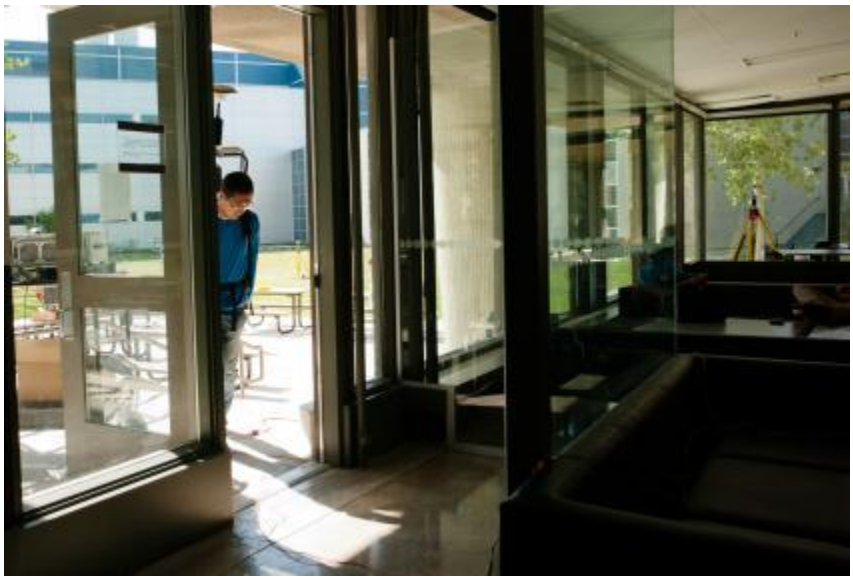

Figure 4.6: Engineering Lounge Entrance

Figure 4.7 and Figure 4.8 provides a different view of the Engineering Lounge's interior; here it is possible to see the large windows positioned to the west and east of the lounge. What is less apparent is a final metal mesh screen located directly above the stone barrier situated in the middle of the lounge. These metal screens, along with the large stone barrier have the potential generate additional multipath errors for any signals that penetrate the Engineering Lounge.

Figure 4.7: Engineering Lounge (1 of 2)

Figure 4.8: Engineering Lounge (2 of 2)

To summarize the challenges that the light-indoor environment presents to GNSS receivers, the primary challenge is the lack of strong line-of-sight GNSS signals in the area. Furthermore, any non-line-of-sight signals that enter the test area can contain significant pseudorange errors that can induce large positioning errors to the GNSS receiver.

The purpose of testing a vector-based receiver in the environment described in this section is to assess the extent to which DGPS corrections and UWB ranging can improve a vector-based GNSS receiver's tracking sensitivity, navigation solution availability and positioning accuracy while operating in such challenging environments. As was shown in the residential testing environment presented in Chapter 3, although a timber framed house is capable of taxing a traditional scalar tracking GNSS receiver, a vector-based

GNSS receiver was able to track strongly attenuated signals even in the basement of the house. In order to assess the operating limits of a vector-based receiver, an environment with higher signal attenuation and stronger multipath is needed. To this end, the equipment setup used in this test is presented in the following subsection below.

4.3.2 Equipment Setup

This section describes the equipment used for collecting GNSS and UWB data in the urban environment described in section 4.3.1. The equipment used for the testing of the UWB and DGPS aided vector-based receiver can be broken up into four components; these components include three static stations and a mobile station. The location of the three static stations is shown on Figure 3.7; the trajectory of the mobile station is shown in green. The UWB/DGPS aided vector-based receiver (the focus of this research) is considered as a part of the mobile station.

Figure 4.9: UWB and DGPS Stations

The focus of this research is on the tracking and navigation performance of the rover receiver that is mounted on a metal-framed backpack and provides a platform for determining pedestrian motion both indoors and out. The metal-framed backpack used for mounting hardware components such as the NovAtel GNSS antenna, MSSI UWB radio, and NovAtel SPAN inertial navigation system can be seen in Figure 4.3 through Figure 4.8. This is referred to as the mobile station; static GPS and/or UWB radios placements shown as Stn. 1, 2, and 3 on Figure 3.7 are referred to as static stations.

4.3.2.1 Mobile Station

The mobile station used for logging data for the UWB/DGPS aided vector-tracking receiver consists of two main components. The open-framed backpack shown on Figure 4.7 holds a GNSS antenna, a UWB radio, and a NovAtel inertial navigation system used for obtaining a reference navigation solution. Due to the weight and size of the RF front-end being used, the National Instruments RF front-end along with the necessary RAID storage array and oscillator is placed separately on a stationary cart.

Figure 4.10 shows the equipment schematic of the mobile station. First, the RF signal from the GNSS antenna is fed through a low-noise amplifier to boost the incoming signal. This is necessary for long RF cable runs to the RF front-end placed on the cart. Next, the signal is split using an RF splitter where the signal is sent to the NovAtel inertial navigation system used for obtaining a reference navigation solution. The NovAtel inertial navigation system consists of a NovAtel SPAN-SE ultra-tight GNSS receiver and a tactical grade NovAtel UIMU-LCI inertial measurement unit. The second

RF output is sent to the National Instruments RF front-end used to down convert, and sample the incoming signal; this process is performed with the aid of an external BVA double-ovenized crystal oscillator (D-OCXO) and the resulting digitized signal is stored on a RAID storage array. The IF sample stored on the RAID array are then used to evaluate the UWB/DGPS aided vector-tracking algorithm.

In order to obtain UWB range measurements, a UWB radio is fixed beneath the GNSS antenna on the open-frame metal backpack. UWB obtained by the radio are stored on a netbook computer and time-tagged using the CPU time on the computer. In order to ensure that the CPU time is accurate, the time obtained from NovAtel SPAN-SE receiver is used to synchronize the netbook's CPU time with GPS time.

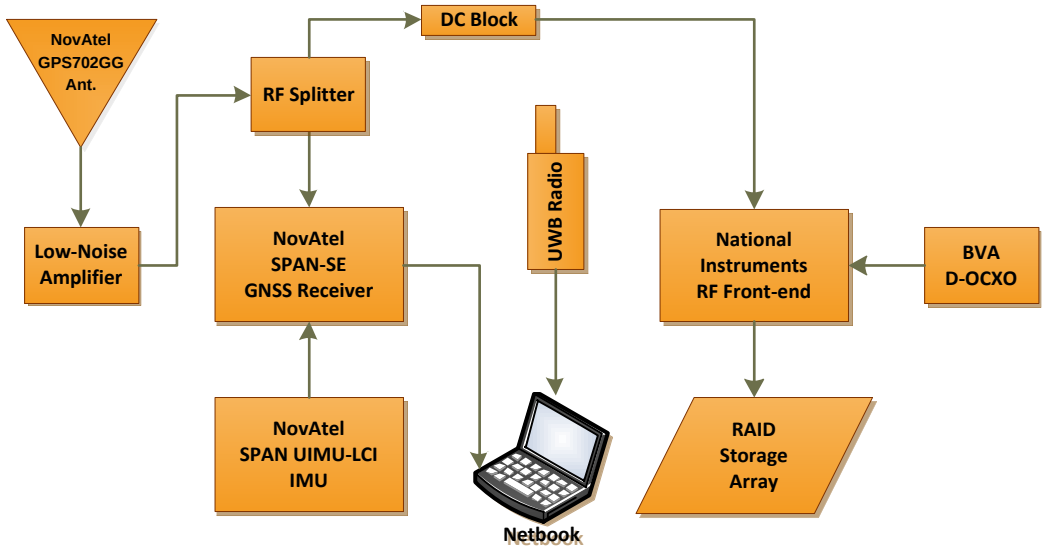

Figure 4.10: Mobile Station – Equipment Schematic

Next, a set of static reference receiver was used to provide UWB ranging measurements to the rover receiver along with DGPS corrections.

4.3.2.2 Static Station 1 for Outdoor DGPS Corrections

The equipment schematic for static station one is provided in Figure 4.11. Here, station one acts as a static reference GPS receiver for generating DGPS corrections; this process is described in section 4.2.1. To do this, the output of the GNSS antenna is first connected to a low-noise amplifier which is necessary for long cable runs. After the signal power is boosted by the low-noise amplifier, the signal is split using an RF-splitter and fed to two key components.

The first component is a survey grade NovAtel OEMV3 GNSS receiver used to survey the reference coordinates of the antenna. Here, the NovAtel OEMV3 receiver is used to collect pseudorange, Doppler and carrier phase GNSS observations for determining the precise position of the reference GPS receiver antenna.

The second component is a National Instruments RF front-end used for down conversion, sampling, and analog-to-digital conversion of the incoming RF signal; these processes are governed using an ovenized crystal oscillator (OCXO). After this, the IF samples from the RF front-end is stored on a hard drive array. DGPS corrections are generated from the pseudorange residuals after post-processing the IF samples using fixed coordinates obtained from the reference station coordinates.

The NovAtel OEMV3 GNSS receiver at station one is used collect GPS and GLONASS pseudorange, Doppler, and carrier phase measurements that are later post-processed using NovAtel's GrafNet software to generate the precise coordinates of the receiver

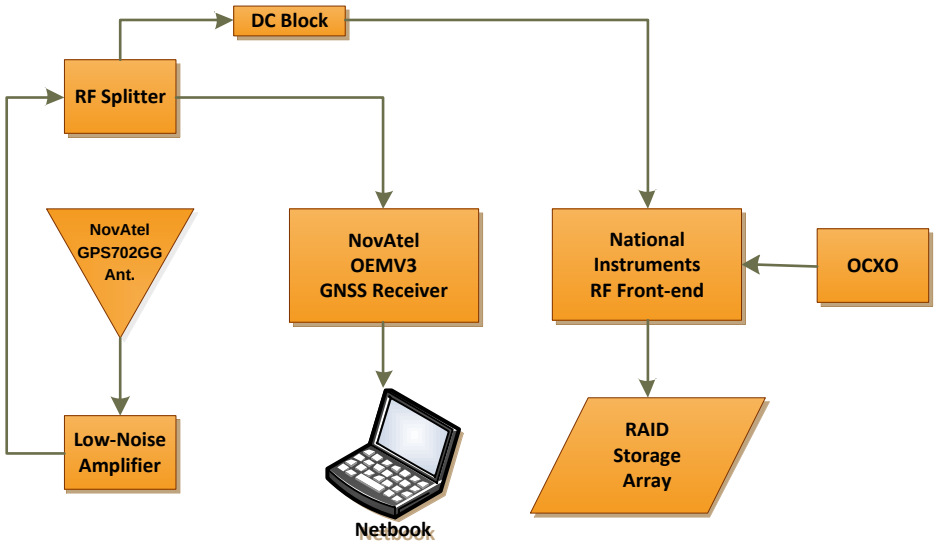

Figure 4.11: Static Station 1 – Equipment Schematic

It should be noted that, in general, DGPS reference stations are best positioned in an open-sky, low multipath environment such as that found on a rooftop; this is done to minimize the effect of multipath errors being passed on to a the mobile receivers that make use of the differential corrections. However, due to limitations in equipment logistics, it was not possible to setup a DGPS reference station with an RF front-end connected to a rooftop GNSS antenna. Because of this, the DGPS corrections generated by Static Station 1 had a detrimental effect on the DGPS aided vector-base receiver results shown in Chapter 5. Under ideal circumstances, differential GNSS corrections should always have positive impact on receiver performance rather than a negative impact.

4.3.2.3 Static Station 2 for UWB Ranging

Static station 2 shown on Figure 4.12 is located at the corner of a concrete pad, near the entrance to the engineering lounge.

Figure 4.12: Static Station 2 – Outdoor UWB Radio

The station consists of a UWB radio used for outdoor ranging and a survey grade NovAtel GNSS receiver used for determining the radio position. The equipment schematic for this station is provided in Figure 4.13.

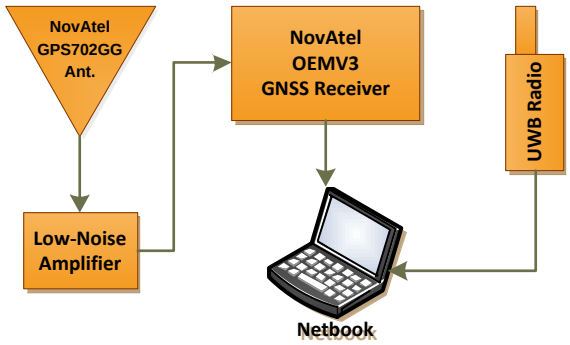

Figure 4.13: Static Station 2 – Equipment Schematic

Similar to station one, a NovAtel OEMV3 GNSS receiver was used in combination with a NovAtel GPS702GG antenna to collect GPS and GLONASS pseudorange, Doppler, and carrier phase measurements to visible satellites. The location of the station was then computed using NovAtel's GrafNet post-processing software to obtain reference coordinates with a centimetre level accuracy.

4.3.2.4 Static Station 3 for Indoor UWB Ranging

Static station 3 shown on Figure 4.14 consists of a UWB radio and a netbook. The equipment schematic of the setup is shown on Figure 4.15. Note that the GNSS antenna shown in Figure 4.14 was not used for the purpose of this test. Once again, the MSSI UWB radio shown in the figures was used to provide range measurements to the mobile station. The reference coordinates of the radio was obtained with a total station using conventional surveying.

Figure 4.14: Static Station 3 – Indoor UWB Radio

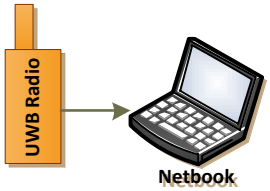

Figure 4.15: Static Station 3 – Equipment Schematic

4.3.3 Reference Navigation Solution

In order to obtain a high accuracy reference trajectory for the rover receiver, GNSS and inertial measurements from the NovAtel SPAN-SE GNSS receiver and SPAN UIMU-LCI inertial measurement post-processed using a tightly-coupled navigation solution. The SPAN-SE is capable of logging GPS and GLONASS observations which are combined with GNSS observations from a NovAtel OEMV3 receiver setup on the roof of the CCIT building. By combining the observations from both receivers, a double differenced fixed carrier phase ambiguity solution can be obtained while the rover receiver operates outside. A sky plot of all GNSS satellites above the horizon during the period of the data collection is shown on Figure 4.16.

When the receiver enters the indoor environment only pseudorange and Doppler observations are available and the accuracy of the reference trajectory depends mainly on quality of the UIMU-LCI inertial measurement unit. In order to achieve metre level accuracy indoors, the NovAtel inertial navigation system was first initialized with a 15 minute static period outdoors, followed by two minutes of figure-8 maneuvers to achieve a fine IMU alignment. After the IMU had obtained fine alignment, the inertial system was brought indoors to complete the indoor portion of the test. After several minutes of indoor testing, the inertial system was brought outdoors once again and figure-8 maneuvers were performed for another two minutes; these maneuvers were followed by another 10 minute static period to facilitate the reverse GNSS/INS processing in NovAtel's Waypoint Inertial Explorer software.

By processing the GNSS/INS data in both forward and reverse direction and subsequently combining the two trajectories, a reference trajectory with an accuracy better than 1.0 metre in position and 12 centimetres per second in velocity was achieved while indoors. Outdoors, the positioning accuracy was better than 15 centimetres. A sky plot of all available GNSS satellites during the data collection period is shown on Figure 4.16.

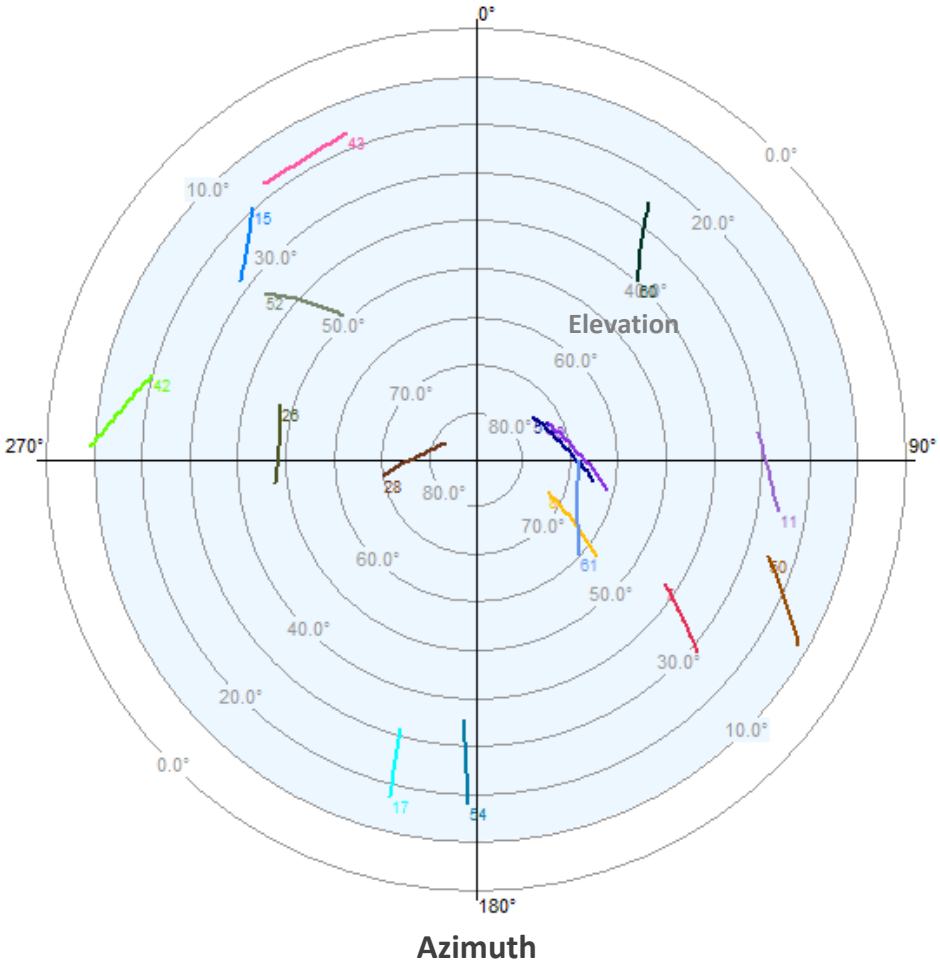

Figure 4.16: Sky Plot for Data Collection Period

4.4 Summary

This chapter described the method used in generating differential GPS corrections from a static reference station. It also discusses a method integrating UWB range measurements with a vector-based GNSS receiver. To ensure both GNSS and UWB measurements are of sufficient quality prior to using them in the navigation solution update, an observation pre-filtering strategy for both GNSS and UWB observations was discussed. This was followed by a description of the Kalman filter tuning parameters needed for pedestrian applications using a vector-based GNSS receiver.

The chapter also presents a description of the test environment and equipment needed to evaluate the effectiveness of adding DGPS corrections and UWB range measurements to a vector-based GNSS receiver. Finally, the procedure used to obtain a reference navigation solution is discussed; this reference navigation solution is used for evaluating the performance of the vector-based GNSS software receiver developed in this work. The results of the performance evaluation are presented in Chapter 5.

Chapter Five: UWB and DGPS Aided Vector-tracking

5.1 Overview

The focus of this chapter is on the aiding of vector-tracking loops with UWB and DGPS for improving the performance of GNSS receivers in light-indoor environments. In this chapter, the results of a thorough analysis on the impact of aiding vector-based GNSS receivers with UWB and DGPS corrections is presented; the results of this analysis is separated between two primary areas: GNSS signal tracking performance and navigation performance.

5.2 Performance Analysis of a UWB and DGPS Aided Vector-Based GNSS Receiver

The subsections presented herein compare the GNSS signal tracking and navigation performance of a vector-based GNSS receiver aided by UWB and DGPS corrections. In the same manner in which the performance between scalar-tracking, Kalman filter tracking, and vector-tracking receivers were compared in Chapter 3, the following subsections examines the effects of augmenting a vector-based GNSS receiver through UWB range observations and DPGS corrections. The tracking loop and navigation filter parameters used in the vector-based GNSS receivers being compared are found in Table 5.1 and Table 5.2 respectively. Similar to the data collection described in Chapter 3, the actual oscillator used to drive the RF front-end was a high-end double-oven crystal oscillator (D-OCXO). By modeling the oscillator as a VCTCXO, it is possible to approximate the performance that one may expect from a low-cost receiver that uses a much more economical VCTCXO instead. On the contrary, if a less stable VCTCXO was

used to drive the RF front-end, it would not be possible to evaluate the effect of using a high quality D-OCXO using the same dataset; for this reason, a D-OCXO was chosen for the data collection.

Table 5.1: Tracking Loop Parameters for Vector-Based GNSS Receiver

General Tracking Parameters	
Sampling Rate (MSPS)	5.00
Sampling Type	Complex
Number of Correlators	3
Maximum Coherent Integration (ms)	20
Standard Tracking Parameters	
Code Loop Filter Order	1
Frequency Loop Filter Order	2
Frequency Loop Filter Bandwidth (Hz)	8.00
Phase Loop Filter Order	3
Phase Loop Filter Bandwidth (Hz)	15.00
Kalman Filter Tracking Parameters	
Amplitude Standard Deviation $(\mathrm{dB}/\sqrt{\mathrm{Hz}})$	1.00
Code Carrier Divergence $(\mathrm{m}/\sqrt{\mathrm{Hz}})$	0.04
Line of Sight Spectral Density $(\mathrm{m/s^2}/\sqrt{\mathrm{Hz}})$	4.00
Frequency Error Threshold	5.00
Oscillator H-Parameter h_0 $(\mathrm{Hz}/\sqrt{\mathrm{Hz}})$	1.00E-21
Oscillator H-Parameters h_{-1} $(\mathrm{Hz^2}/\sqrt{\mathrm{Hz}})$	1.00E-20
Oscillator H-Parameters h_{-2} $(\mathrm{Hz^3}/\sqrt{\mathrm{Hz}})$	1.00E-20

Table 5.2: Navigation Filter Parameters for Vector-Based GNSS Receiver

Navigation Filter Parameters	
GPS Measurement Rate (Hz)	20
GPS Pseudorange Standard Deviation (m)	5.00
GPS Doppler Standard Deviation (m/s)	0.20
Observed UWB Range Measurement Rate (Hz)	10.00

Simulated UWB Range Measurement Rate (Hz)	1.00
UWB Range Standard Deviation (m)	2.00
C/N_0 Mask (dB-Hz)	30.00
Elevation Mask (degrees)	10.00
Horizontal Velocity Spectral Density $(m/s/\sqrt{Hz})$	1.00
Vertical Velocity Spectral Density $(m/s/\sqrt{Hz})$	0.50
Oscillator H-Parameter h_0 $(Hz/\sqrt{Hz})$	1.00E-21
Oscillator H-Parameters h_{-1} $(Hz^2/\sqrt{Hz})$	1.00E-20
Oscillator H-Parameters h_{-2} $(Hz^3/\sqrt{Hz})$	1.00E-20

As mentioned in Section 4.3.2.2, the location of Static Station 1 – from which DGPS corrections were generated – was not ideally situated to provide differential GNSS corrections with little to no multipath errors. This was due to the limitations in the equipment logistics; with this in mind, negative impacts on receiver performance discussed in the following sections of this chapter should be attributed to the placement of the DGPS reference receiver in a strong multipath environment. In other words, the negative impacts of DGPS corrections presented in this chapter is strictly due to the circumstances of the test environment used and is not representative of differential GNSS corrections in general.

5.2.1 Navigation Filter Tuning for a Vector-based GNSS Receiver

In determining suitable spectral density values for the velocity states on a vector-based GNSS receiver, it was found that the spectral density of the velocity states had a large impact on the tracking performance of the receiver for weak signal environments. This point is illustrated in Figure 5.1 where the two vector-based GNSS receivers are compared using the same dataset but with different spectral density parameters. The

tightly-constrained receiver shown in green uses the same spectral density values for the velocity states as shown in Table 5.2; in contrast, the loosely-constrained vector-based GNSS receiver had spectral density values as shown on Table 5.3.

Table 5.3: Navigation Filter Parameters for Loosely-constrained Vector-Based GNSS Receiver

Navigation Filter Parameters	
Horizontal Velocity Spectral Density $(m/s/\sqrt{Hz})$	5.00
Vertical Velocity Spectral Density $(m/s/\sqrt{Hz})$	2.50

By comparing the 66^{th} percentile C/N_0 and FLI values for the two receivers on Figure 5.1, it can be seen that the impact of using higher spectral density values for the velocity states had little effect on the tracking performance on strong signals. However, for weaker signals as found on PRN 11 and 24, the difference in tracking performance between the tightly-constrained (green) and loosely-constrained (red) receiver is quite pronounced. For the results shown on Figure 5.1, PRN 11 and 24 were low lying satellites that were partially obstructed by the surrounding buildings whereas all other satellites had direct line of sight with the receivers of interest. What this shows is that, unlike a scalar receiver where a loosely constrained navigation filter will result in noisier position estimates but have no impact on the tracking performance, the tuning of the navigation filter on a vector-based GNSS receiver has a large influence of the tracking performance on weak signals.

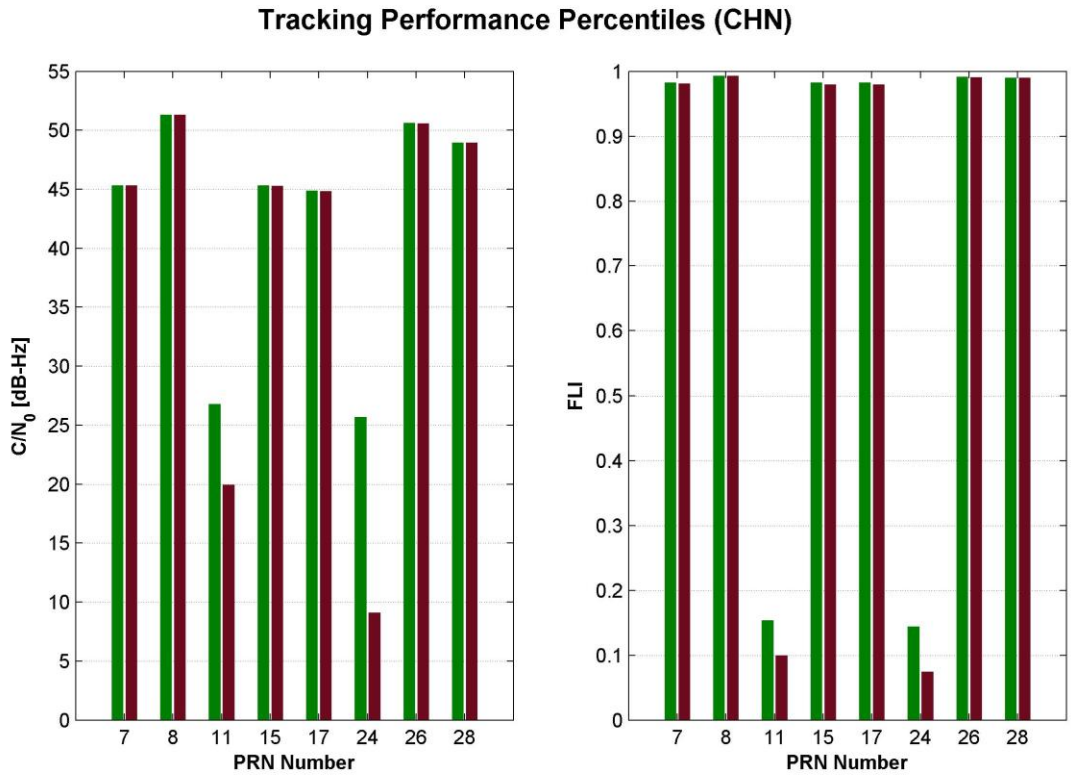

Figure 5.1: Comparison of 66th Percentile C/N_0 and FLI values for a Tightly-constrained (green) and Loosely-constrained Vector-based GNSS Receiver Operating in a High-multipath Signal Environment

5.2.2 UWB Range Observations

Before examining the effects of using UWB ranges for aiding a vector-tracking receiver, the specific characteristics of UWB measurements used in this work needs to be discussed. First, it should be noted that, in this chapter, both observed and simulated UWB ranges were used to aid the vector-tracking receiver. There are two key differences between the observed and simulated UWB ranges used in this work. The single biggest difference between the two is that observed UWB ranges between radio pairs are made asynchronously – this means that, although there are multiple UWB radio pairs, for any given UWB measurement epoch where range observations are available, only range measurements between a single radio pair can be made. In contrast, for simulated UWB measurements, ranges between radios are generated synchronously – this means that for simulated UWB range measurements between the mobile station and all static stations are provided at every measurement epoch. The primary objective in simulating synchronous, error-free UWB measurements is to provide a best-case scenario whereby error-free UWB measurements are made available at regular intervals for aiding the vector-tracking loop. In such a scenario, it is possible to evaluate the maximum benefit that UWB range augmentation can provide to a vector-based GNSS receiver.

It is also important to be aware that each range measurement between a pair of UWB radios taken at a single epoch actually consists of a set of individual range measurements (up to 16 in all for the MSSI radios used) and are observed over a period of less than 0.10 seconds. These individual range measurements are useful in identifying the observation quality since metrics such as received signal strength are not available. An example of

how a set of individual range measurements can be used to identify observation quality is to compute the standard deviation between the individual range measurements for a given epoch. By doing so, it is possible to filter out observations that may be corrupted with large random errors due radio noise and multipath. Moreover, it is possible to average a set of individual measurements in order to reduce the impact of random noise in the range observations.

In the receiver performance analysis presented herein, the raw UWB range measurement sets (up to 16 measurements per epoch) was filtered using the method shown on Figure 5.2. In order to ensure the reliability of the measurement, at least two individual range measurements are required for each range measurement set between any given radio pair. The standard deviation of the range measurements set belonging to a given radio pair is then computed. If the standard deviation of the set of range measurements is greater than 2.0 m, the measurement set are discarded. Otherwise, the mean range is computed using the set of individual range measurements. Finally, a threshold of 45 m was set as the maximum allowable range; if the mean range for a given epoch is greater than this threshold, the measurement is discarded.

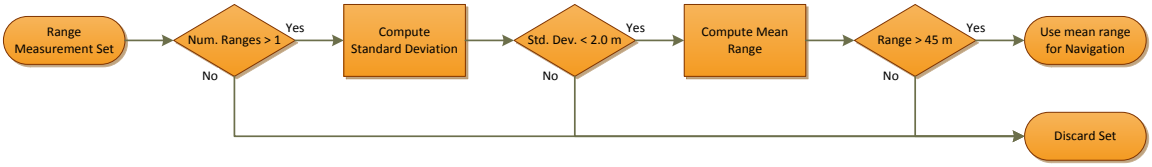

Figure 5.2: UWB Measurement Pre-filtering

The above UWB range pre-filtering is used for two primary reasons. The standard deviation between measurements gives an indication of possible blunders that may exist in a given measurement set. These blunders are likely caused by multipath signals that are reflected off nearby objects; if a measurement set was averaged without any means of blunder detection, large biases may be injected into the Kalman filter by means of corrupted range measurements. Moreover, the UWB radios used cannot differentiate between individual ranging pulses used in taking multiple range measurements in a set. This is a problem in that if two measurement pulses are sent by a radio but a response was not received for the first pulse but a response was received on the second pulse, there are instances whereby the radio will treat the second response as belonging to the initial pulse. In such case, a large ranging bias would be added to the initial range measurement. For this reason, a threshold of 45 m was chosen to ensure that ranges with unusually large biases are rejected. In all, 43.7% of the observed range measurements obtained during the course of the data collection were rejected during the pre-filtering of observations.

For simulated UWB range measurements, since these measurements are generated using the reference trajectory, they can be treated as being free of measurement noise, biases, and scale factor; this is in contrast to observed UWB measurements which contain all three. In observed UWB range measurements, corrections for ranging bias and scale factor errors are also applied before the observations are used. A unique set of bias and scale factor correction terms applied for each radio pair; therefore, the primary error source in the observed UWB ranges is measurement noise. The bias and scale factor correction terms for each radio pair were obtained by plotting and comparing the

observed pre-filtered range measurements with the true range between the reference trajectory of the moving receiver (rover) and the reference (pre-surveyed) coordinates of the static UWB radio positions. By adjusting the bias and scale factor terms for the pre-filtered range observations and comparing the difference between the corrected ranges with the true reference range, it was possible to obtain a nominal correction bias and scale factor term for each radio pair used during the test period. To this end, it is important to stress that the correction terms are nominal values for the entire period and that the correction terms cannot compensate for the exact bias and scale factor in any given epoch as these terms are correlated with the received signal strength. As a result, residual biases and scale factor errors still exists in the corrected UWB ranges.

5.3 GNSS Signal Tracking Performance

The following subsections show the effects of adding UWB ranging and DGPS corrections to a vector-based GNSS receiver. More specifically, the impacts of these augmentation techniques are examined in the context of high-multipath urban outdoor environments and indoor environments with strong signal attenuation. The assessment of the receiver performance is separated into two key areas; first, GNSS tracking performance is examined to ascertain the sensitivity and robustness of the vector-tracking loops under these conditions. This is followed by an assessment of the quality of GNSS observations generated by the tracking loops. Based on this information, the second key area of the receiver performance analysis focuses on the navigation solution availability and accuracy which, not only is influenced by the GNSS measurement quality and

availability, but also have a direct influence on the signal tracking performance in a vector-based GNSS receiver.

In this analysis of the vector-tracking performance using UWB and DGPS aiding, receiver performance is evaluated using real world data. As such, tracking sensitivity and robustness cannot be established in an absolute sense where signal power levels at which a given receiver will cease to maintain lock can be determined. However, the results presented herein do allow for a relative performance comparison that provides insight into how different GNSS augmentation techniques may impact a vector-based GNSS receiver.

5.3.1 Tracking Sensitivity and Robustness

The following discussion compares the tracking sensitivity and robustness of a vector-based GNSS receiver. As mentioned previously, the results in this chapter are separated into two challenging signal environments, a high-multipath outdoor urban environment, and an indoor environment with strong attenuation of GNSS signals. Given the limitations of the use of real-world UWB data mentioned in Section 0, further comparisons are made between results using real-world UWB range measurements and simulated UWB range measurements. The primary purpose of using simulated UWB range measurements is to determine the best possible performance gains that can be achieved under an ideal setting.

5.3.1.1 High-Multipath Outdoor Urban Environment

To properly assess the impact of using UWB ranging and DGPS corrections on a vector-based GNSS receiver in a high-multipath outdoor urban environment, the tracking statistics for an unaided vector-based GNSS receiver is presented in Figure 5.3. These tracking statistics comprise of the Carrier-to-Noise Density (C/N_0) and Frequency Lock Indicator (FLI) which provide an indication of the code and frequency tracking accuracy for a given receiver channel. The figures presented for the high-multipath outdoor environment was obtained using data collected with pedestrian motion. In Figure 5.3, it is possible to see a large drop in C/N_0 and FLI values across all satellites approximately 80 seconds into the dataset; although this last portion of the dataset was obtained while the receiver was still positioned outdoors, it represents a transition between an outdoor and an indoor environment whereby the receiver moves under a large overhanging feature of the Engineering building. During this period of time, the Engineering building masked many of the satellites that previously had line-of-sight with the receiver – thus, a large drop in signal power exists during the last 10 seconds of the dataset shown.

As can be seen in Figure 5.4, except for satellite PRNs 11 and 24, the tracking performance of most satellites does not change with DGPS and UWB augmentation. The unaffected PRNs are primarily satellites with direct line-of-sight to the receiver and therefore have relatively strong signal power compared to PRN 11 and 24. These two satellites were located on the eastern portion of the sky and experienced periodic occlusions by the Engineering building as the receiver moved towards the building.

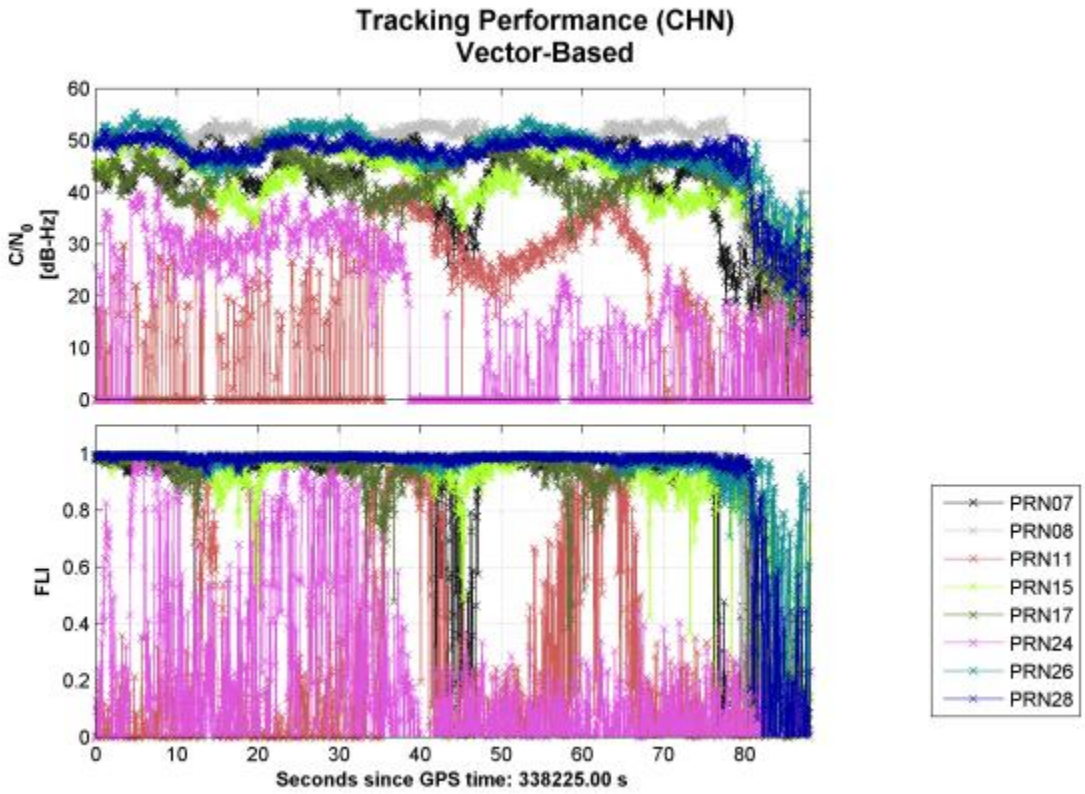

Figure 5.3: Tracking Performance for an Unaided Vector-Based GNSS Receiver in a High-Multipath Outdoor Urban Environment

When assessing the impact of adding UWB ranging and DGPS corrections on PRN 11 and 24, it was found that in a high-multipath environment, the UWB augmented vector-based GNSS receiver had the best tracking performance while DGPS corrections led to degradation in tracking performance compared to the unaided vector-based receiver. From Figure 5.4, it was found that the addition of DGPS corrections resulted in a drop in C/N_0 of 6-8 dB on PRN 11, and 7-12 dB on PRN 24.

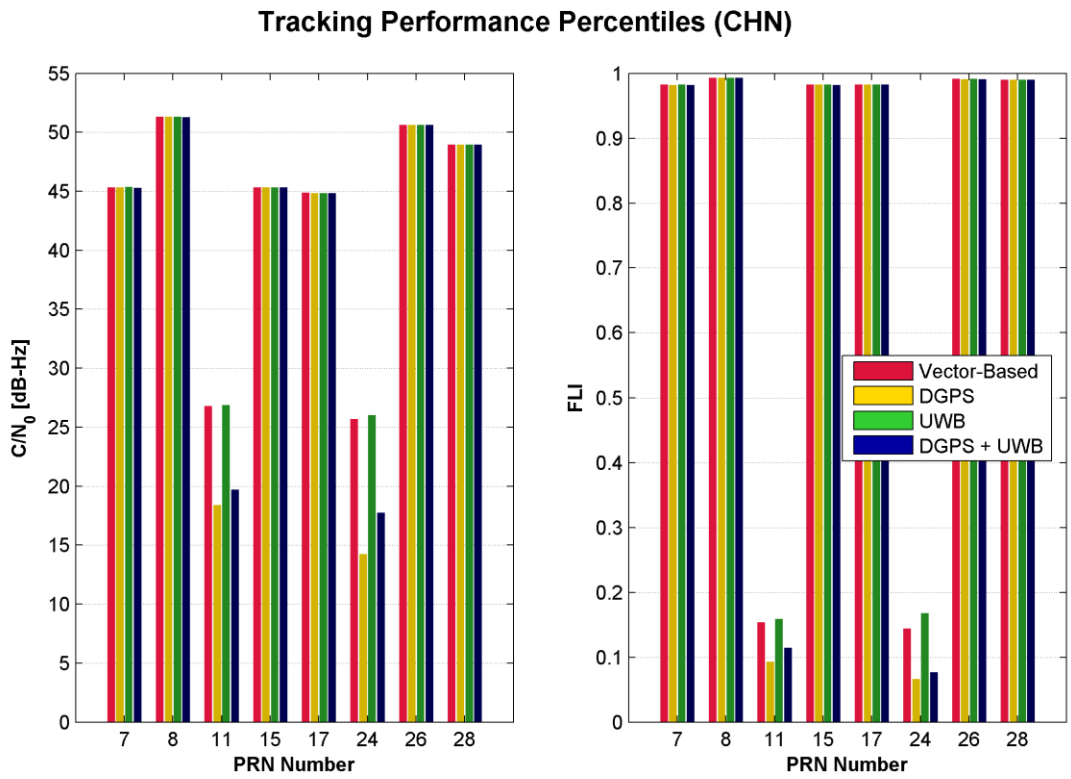

Figure 5.4: Outdoor Tracking Performance using Real-World UWB ranges and DGPS Corrections at the 66th Percentile

Since the reference receiver used for generating DGPS corrections was also located in a high-multipath environment, multipath errors in the DGPS corrections contribute additional pseudorange measurement errors in the mobile receiver. Because pseudorange measurements are used in a Kalman filter to compute a navigation solution, any sudden changes in position due to Kalman updates between GPS measurement epochs and UWB measurement epochs will also result in errors in the velocity estimates; these velocity errors then translate into an NCO frequency error within a vector-tracking loop and

degrade tracking performance. When transitioning between a GPS measurement epoch with biased pseudorange measurements from multipath and a relatively unbiased UWB measurement epoch, the sudden change in position will induce errors in the velocity states. Similar to how a noisy navigation position solution caused by an increase in spectral density for the velocity states will lead to degraded tracking performance as discussed in Section 5.2.1, jumping between biased and unbiased measurement updates can also lead to degraded tracking performance on a vector-based GNSS receiver.

The fact that UWB augmentation improved tracking performance on a vector-based GNSS receiver is not entirely surprising since the UWB range measurements help to strengthen the navigation accuracy of the vector-based GNSS receiver. By improving the positioning accuracy of the navigation filter within the vector-based GNSS receiver, the velocity estimates were also improved through Kalman filtering. This, in turn, leads to more robust tracking of weak signals.

At this point it should be made clear that the improvement in tracking sensitivity and robustness due to UWB range augmentation on a vector-based GNSS receiver is demonstrated for an outdoor environment with partial sky obstructions. In other words, there are still sufficient satellites observations to allow the vector-based GNSS receiver to accurately estimate the receiver clock drift terms that are needed to update the NCO. The next section will look at how a vector-based GNSS receiver behaves with UWB ranging and DGPS corrections under much more challenging conditions where all signals are attenuated in an indoor environment.

5.3.1.2 Indoor Urban Environment

Compared to high-multipath outdoor environments, indoor GNSS signal tracking brings on a new set of challenges due to the weak power of the received GNSS signals. In such scenarios, a low C/N_0 may not necessarily indicate poor tracking performance for a given receiver channel as low C/N_0 values may be caused by low received signal power due to signal attenuation rather than correlation loss. To determine the effects of UWB and DGPS aiding on the tracking performance of a vector-based GNSS receiver, the 66^{th} percentiles of the C/N_0 and FLI values are compared between the vector-based GNSS receivers. An unaided vector-based receiver is used as a point of reference for performance comparison.

Based on the 66^{th} percentile indoor tracking statistics shown on Figure 5, it can be seen that for stronger signals such as on PRN 7, 15, and 26, the addition of DGPS corrections or UWB range measurements resulted in a small improvement in C/N_0 (2-3 dB-Hz). However, DGPS corrections and UWB range measurements had little effect on other weaker signals. Moreover, on PRN 7, 8, 24, 26, and 28, it was found that combining DGPS corrections with UWB range measurements resulted in a noticeable degradation of the overall tracking performance as compared to the unaided vector-based receiver (3-6 dB-Hz). This is clearly seen when comparing the C/N_0 values on the various receivers. This is similar to what was found in the high multipath outdoor environment described in Section 5.3.1.1. When comparing the FLI values, it can also be seen that combining both DGPS correction with UWB range measurements resulted in marginally lower FLI values on the affected satellites. Lower FLI values on a vector-based receiver indicate

that the NCO had more trouble predicting the frequency of the incoming signal accurately.

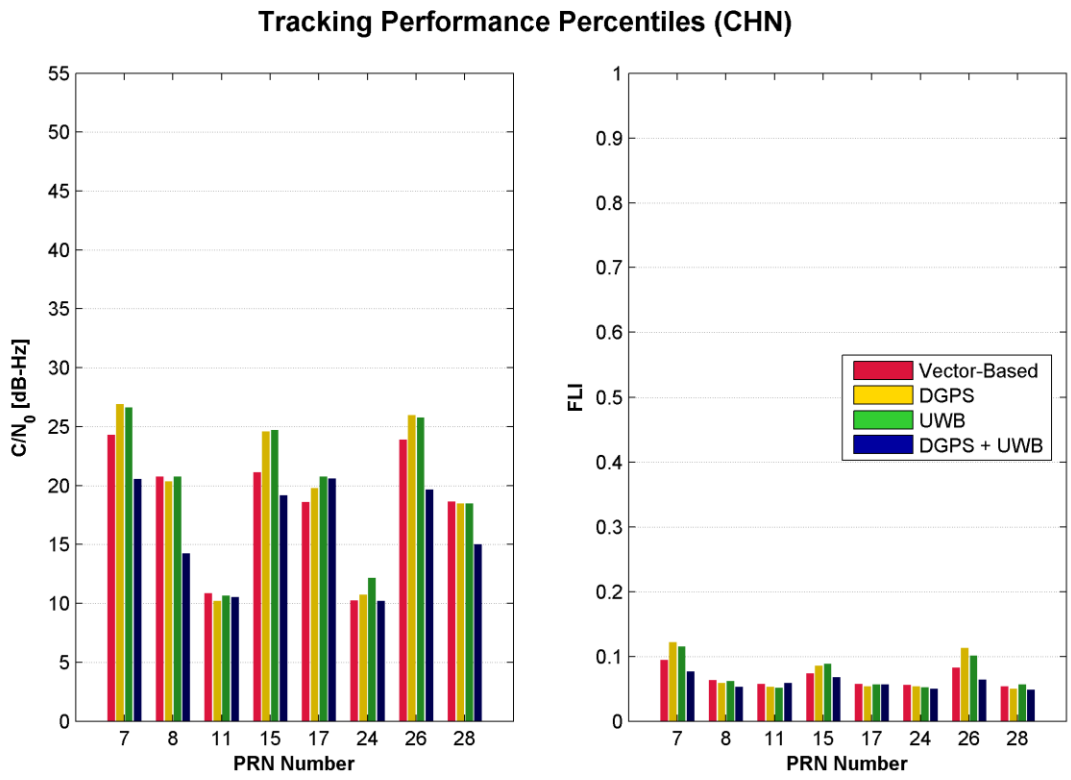

Figure 5.5: Indoor Tracking Performance using Real-World UWB ranges and DGPS Corrections at the 66th Percentile

At this point, the impact of UWB range measurement availability should be compared. The introduction of velocity errors when transitioning between biased DGPS measurement updates and relatively unbiased UWB range measurements are more pronounced when the availability of UWB range measurements are sporadic. The reason

the DGPS corrected pseudorange measurements are considered as being biased is due to the presence of multipath errors that change very slowly relative to the update rate of the navigation filter – on the order of minutes for multipath errors from a static receiver compared to the 50 Hz update rate of GNSS measurements and 10 Hz update rate of UWB measurements. During an extended outage of UWB measurements, a combined DGPS and UWB navigation solution will naturally be very similar to that of a DGPS-only solution. Once a UWB measurement becomes available, the Kalman update for the UWB measurement epoch will cause the navigation solution to move away from a biased DGPS-only navigation solution and back towards a relatively unbiased UWB augmented navigation solution; this transition leads to the introduction of velocity errors in the navigation solution. However, if UWB measurements are made available to the navigation filter at short, uninterrupted intervals, velocity errors caused by large differences between a biased DGPS measurement updates and an unbiased UWB measurement update will result in the reduction of velocity errors in the navigation solution. This is clearly shown in the analysis of the indoor navigation solution accuracy in Section 0 below.

With the impact of UWB measurement availability in mind, one would therefore expect an improvement in tracking performance when combining DGPS corrected pseudorange measurements with a regular, uninterrupted source of UWB range measurements. This improvement is shown on Figure 5.6 which compares the tracking performance between a vector-based GNSS receiver using real-world (red) and simulated UWB range measurements (green). In the figure shown, a consistent improvement in tracking

sensitivity for the combined DGPS and UWB aided vector-based GNSS receiver can be seen when going from using intermittently available real-world UWB measurements to using simulated UWB range measurements that were updated at regular 5 Hz intervals. Here, it can be seen that all the satellites with exception to PRN 11, 17 and 24 showed a noticeable increase in C/N_0 and, to a lesser degree, FLI. These improvements shows that the vector-based receiver using regularly spaced, simulated UWB range measurements was better able to estimate the incoming signal frequency of the incoming signals.

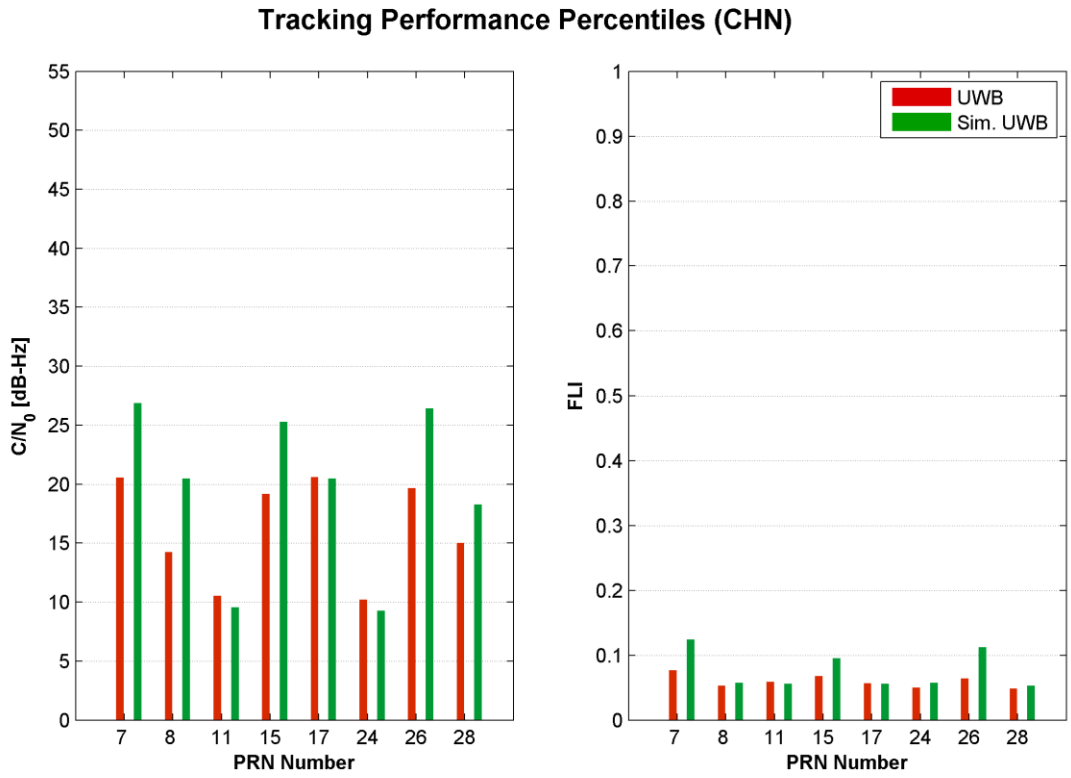

Figure 5.6: Indoor Tracking Performance comparing Simulated and Real-World UWB ranges and DGPS Corrections at the 66th Percentile

Based on the comparison of tracking performance between vector-based GNSS receivers using DGPS corrections and/or UWB range measurements it was found that an improvement in tracking sensitivity can be realized when either DGPS corrections or UWB range measurements are used. However, it was also found that measurement biases from slowly changing multipath errors introduced through DGPS corrections can reduce tracking sensitivity when these measurements are combined with relatively unbiased but intermittently available UWB range measurements. This is caused by velocity errors introduced when unbiased range measurements are used to update a biased navigation solution. With this being said, when unbiased UWB range measurements are made available to the receiver at regular intervals, an improvement in tracking performance can be realized.

5.3.2 Measurement Quality

While an increase in tracking performance may improve availability of GNSS measurements, it does not guaranty increased measurement accuracy that, in turn, affects the accuracy of the navigation solution. To this end, it is important to examine the effect that UWB ranging and DGPS corrections may have on the precision of GNSS observations. Similar to Section 3.3.1.1, the distribution of pseudorange residuals are compared in both an outdoor high-multipath environment as well as in an indoor weak signal environment.

5.3.2.1 High-Multipath Outdoor Environment

Figure 5.7 shows the distribution of pseudorange residual magnitudes as a function of the C/N_0 using DGPS corrections and UWB augmentation on a vector-based GNSS receiver in a high-multipath outdoor environment.

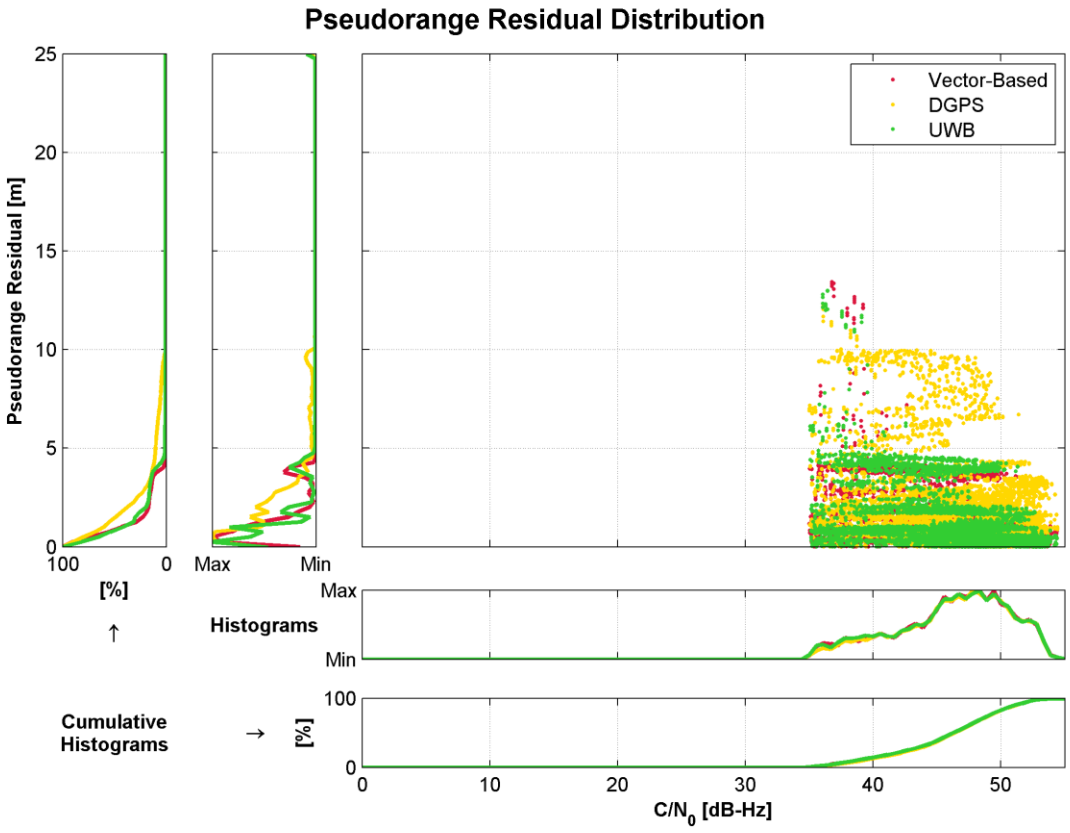

Figure 5.7: Comparison of Pseudorange Residual Magnitude Distributions for Vector-Based GNSS Receiver with DGPS Corrections and Real-World UWB Ranges

(High-Multipath Outdoor Urban Environment)

As expected, because the reference GNSS receiver was located in a high multipath environment, random errors such as receiver noise and multipath from a reference GNSS receiver also contributes to the measurement errors in the mobile receiver. Accordingly, the receiver using DGPS corrections has a greater range of the pseudorange residuals as shown in the cumulative histogram on the far left subplot in Figure 5.7. Meanwhile, the residual distributions for the standalone and UWB augmented receivers are very similar. Since the number of usable UWB range observations was very low due to the challenging environment, the UWB augmented solution is very similar to the stand-alone vector-based results. It should also be noted that the histograms of the C/N_0 values for all used observations between the three receiver configurations are almost identical.

In order to better appreciate the impact of using UWB range observations, simulated UWB ranges were used to generate the results on Figure 5.8; here, the results of using simulated UWB range observations were compared with those of real-world UWB data. Also included in the figure are the pseudorange residual distributions for a vector-based receiver augmented with both DGPS and simulated UWB range measurements. By comparing the three sets of results, it can be seen that all the pseudorange observations from the receiver using simulated UWB ranges (shown in magenta) had residuals below 2.5 metres, whereas a large portion of the pseudorange residuals on the receiver using real-world UWB observations had a significant number of residuals in the 4 metre level (shown in green); this suggests that a noticeable portion of the pseudorange observations contain biases, possibly due to errors in the real-world UWB observations. Moreover, when examining the pseudorange residuals of the receiver when both simulated UWB

ranges and DGPS corrections were used, it was found that, despite the addition of UWB ranging, DGPS corrections reduced the precision of the corrected pseudorange observations and resulted in a lower precision of the observations as in the case in Figure 5.7 where only DGPS corrections added to the vector-tracking receiver.

While examining the C/N_0 distribution, it is interesting to note that between all three receiver configurations, the C/N_0 of all observations considered by the navigation filter (both used and rejected) had nearly identical distributions. This suggests that although using different methods for receiver augmentation may not make a large impact on the tracking statistics on a given receiver, it still has a significant impact on the quality of the pseudorange observations.

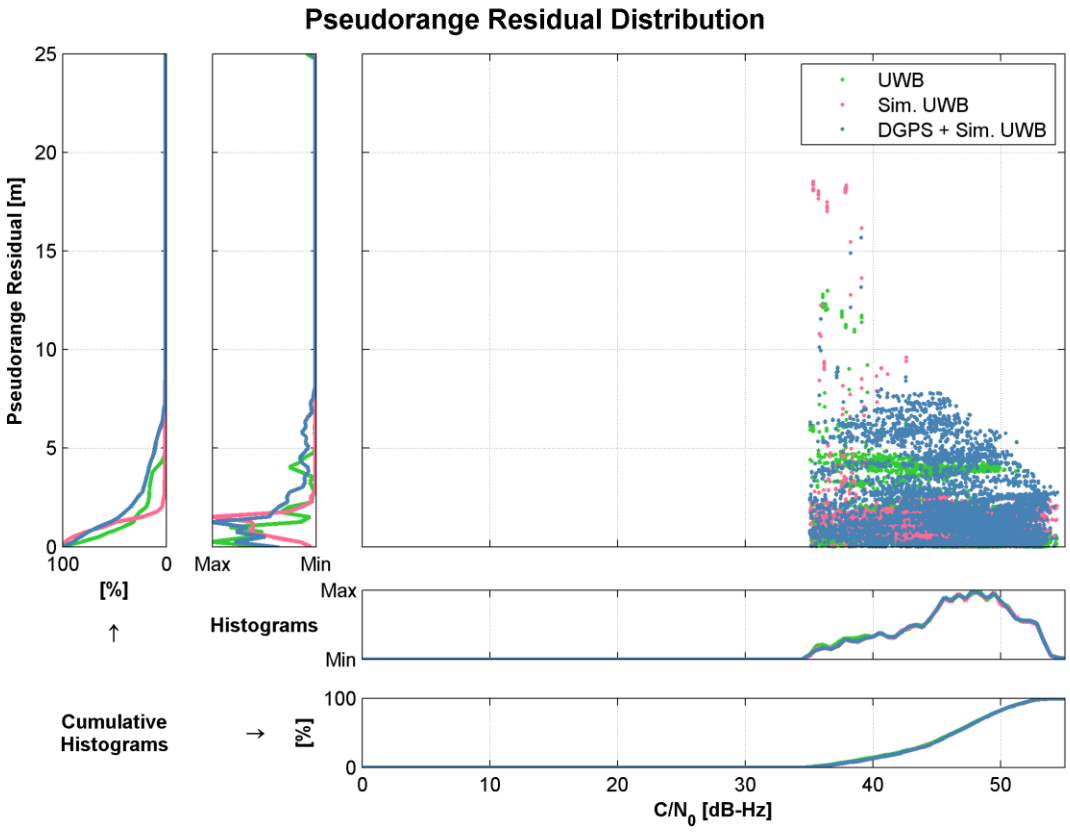

Figure 5.8: Comparison of Pseudorange Residual Magnitude Distributions for Vector-Based GNSS Receiver with Simulated UWB Ranges (High-Multipath Outdoor Urban Environment)

When comparing Doppler residuals, it was found that all vector-based GNSS receivers, both aided and unaided had similar results in the distribution of their Doppler residuals; because of this, the residuals are not shown.

5.3.2.2 Indoor Urban Environment

Similar to the pseudorange distribution plots found in Figure 5.7 and Figure 5.8, Figure 5.9 and Figure 5.10 shows the residual distribution for the same set of vector-based GNSS receivers operating in an indoor weak signal environment. What is most noticeable in Figure 5.9 and Figure 5.10 is the greatly reduced number of available pseudorange observations due to the weak signal environment. However, as is the case for the high-multipath environment, the C/N_0 for GNSS observations appear to be nearly identical between the various combination of UWB and DGPS receiver augmentation methods discussed.

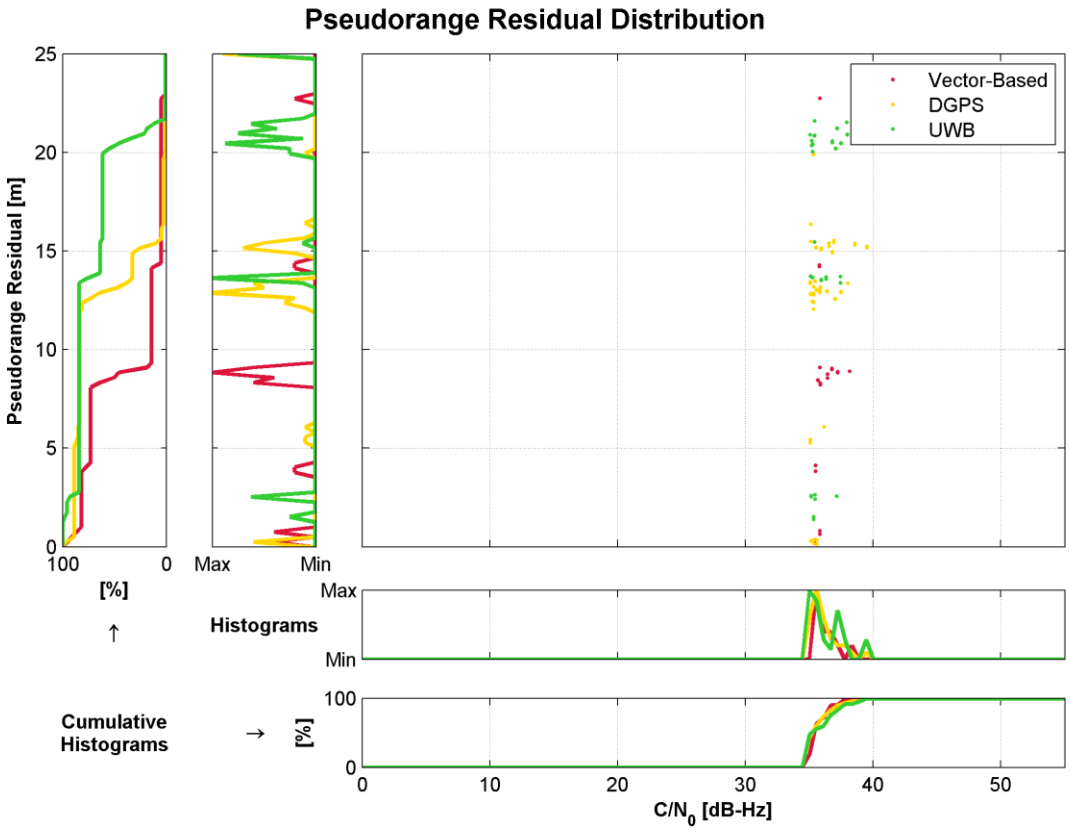

Figure 5.9: Comparison of Pseudorange Residual Magnitude Distributions for Vector-Based GNSS Receiver with DGPS Corrections and Real-World UWB Ranges

(Indoor Weak Signal Environment)

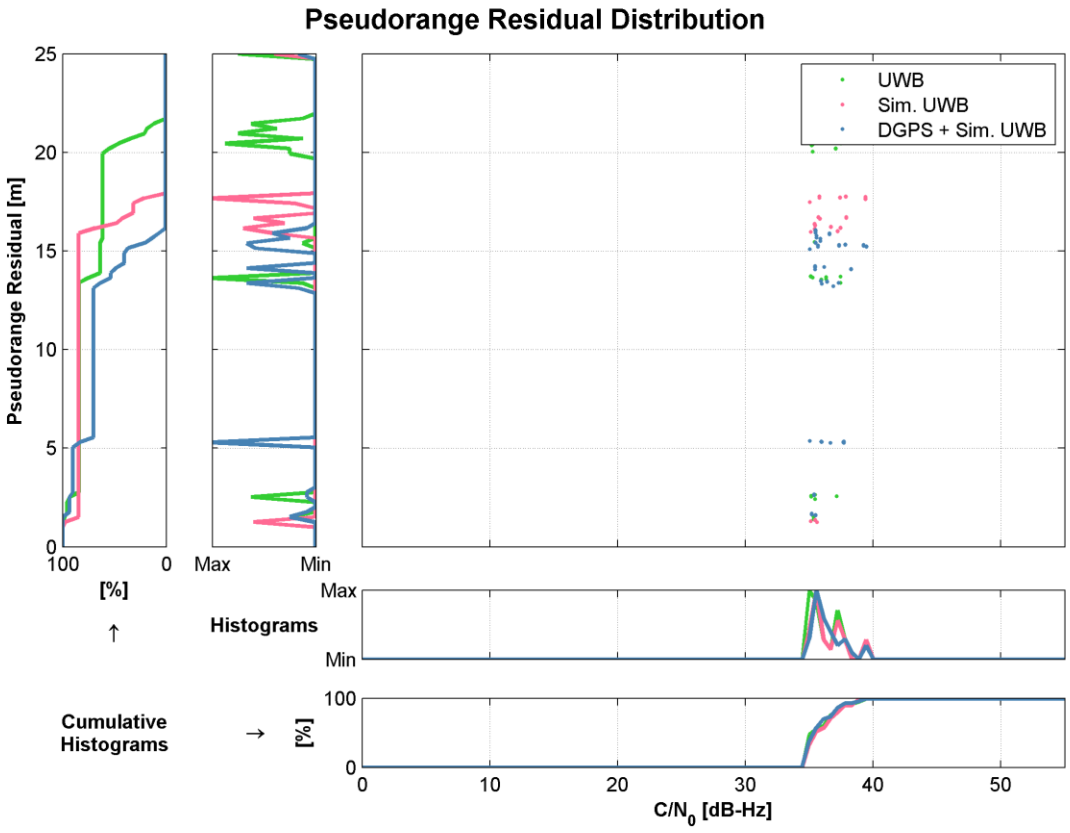

Figure 5.10: Comparison of Pseudorange Residual Magnitude Distributions for Vector-Based GNSS Receiver with DGPS Corrections and Simulated UWB Ranges (Indoor Weak Signal Environment)

Moreover, the different receiver augmentation methods also resulted in noticeably dissimilar residual distributions as is the case for the results shown for the high-multipath outdoor environment. Unlike the results shown for the outdoor environment however, where the navigation solutions are computed based on 6 to 7 satellites at every epoch, the residual distributions from the indoor results cannot be used to directly compare the quality of the residuals since, at any given time, only a single satellite observation was

available to the various receivers evaluated. Because of the strong correlation between the receiver clock bias and position states, without enough measurements to reliably determine the position of the receiver indoors, large pseudorange residuals may arise due to a number of factors which include poor receiver clock bias estimates, large receiver positioning errors as well as errors in the pseudorange. With this being said, the indoor RMS position errors for the vector-based GNSS receiver aided with simulated UWB measurements range between 5 and 15 metres; meanwhile, RMS position errors of over 30 metres was found when real-world UWB measurements. These statistics are discussed with greater detail in Section 0. Meanwhile, the receiver clock bias with its first-order trend removed is shown for the UWB-only and DGPS+UWB aided receivers using both real-world and simulated UWB range measurements in Figure 5.11. On this figure, it is evident that the receiver clock bias has been poorly estimated; discrepancies between the real-world UWB-only results and the simulated UWB and DGPS aided results are well over 10 metres while a false frequency lock in the simulated UWB-only solution resulted in an even greater discrepancy approximately 79 seconds into the indoor test period. This undetected/uncorrected false frequency lock led to a large error in the receiver clock drift estimate for the remainder of the indoor period.

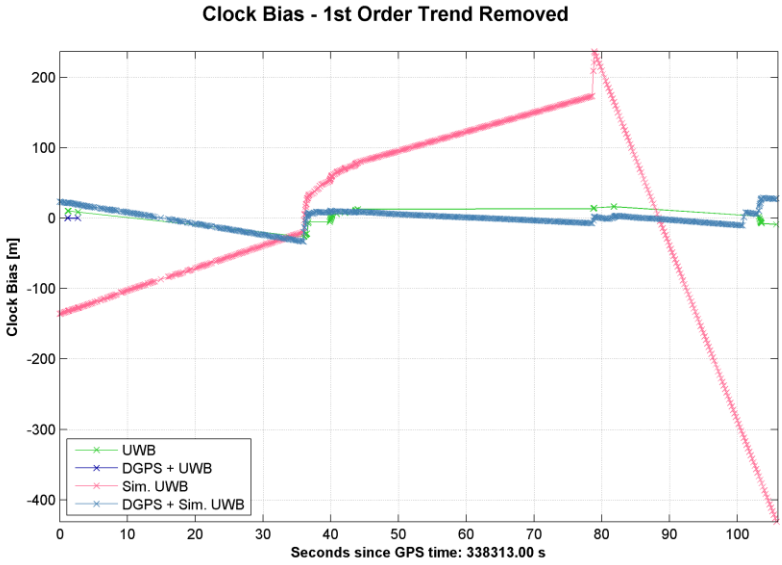

Figure 5.11: Receiver Clock Bias on UWB and DGPS-Aided Vector-based GNSS Receiver in Indoor Environments

As neither the receiver clock bias nor position can be reliably estimated, the pseudorange residuals shown on Figure 5.9 and Figure 5.10 cannot be used to gauge the precision or accuracy. In spite of this limitation however, since a tightly-coupled GNSS/INS reference navigation solution is available, it is possible to determine the errors in the positioning and velocity estimates for the various receivers while operating indoors; this is shown in the following section.

5.4 Navigation Performance

Having evaluated the impact of using DGPS corrections and UWB range measurements in a vector-based GNSS receiver and evaluating its effects on tracking performance and measurement precision, it is important to analyze its effect on over navigation accuracy and availability. These two areas of navigation performance are discussed separately in the following subsections.

5.4.1 Navigation Solution Availability

Depending on the intended navigation application, the availability of a navigation solution may be more important than its accuracy. This is particularly true for consumer applications where a user may not require sub-metre level positioning accuracy but does require a position estimate even in the most challenging of signal environments. In this section, the availability of a navigation solution for vector-based GNSS receivers using different methods of receiver augmentation is discussed. Note that percentage of position availability are based on the percentage of GNSS measurement epochs where a measurement update was available regardless of the measurement type used for the position update; in other words, if no GNSS measurements were available on a GNSS measurement epoch but a UWB range measurement was available to compute a navigation solution, the UWB position update is still counted towards the final availability percentage. Since the GNSS measurement rate was set as 20 Hz, there are a total of 20 GNSS measurement epochs for every second of data shown for the period of interest.

5.4.1.1 High-Multipath Outdoor Urban Environment

The availability of navigation updates for a vector-based GNSS receiver operating in a high-multipath outdoor urban environment is shown on Figure 5.12 and Figure 5.13. When using DGPS corrections and/or real-world UWB range measurements, results for the vector-based GNSS receivers shown on Figure 5.12 are comparable in performance. In the last 5 seconds of the dataset, it was found that the availability of navigation updates on all receivers decreased due to the large overhang near the entrance to the Engineering Lounge which occluded many satellites that were initially in view. When examining Figure 5.13, it can be seen that using simulated UWB measurements which were generated at a rate of 5 Hz improved the availability by a marginal, but noticeable amount. This improvement is primarily due to the continuous availability of simulated UWB measurements whereas the availability of real-world UWB measurements was relatively sparse in between. Although in the outdoor environment this difference is relatively minor, the indoor results much more noticeable and is discussed in Section 5.4.1.2.

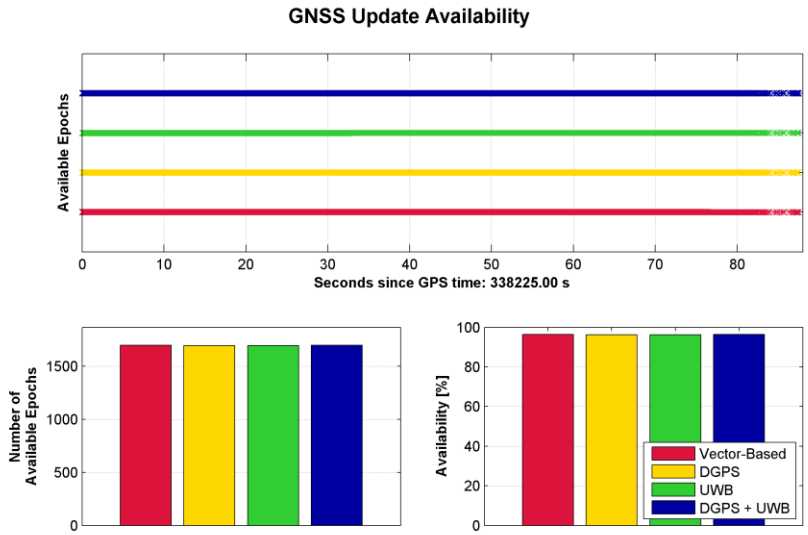

Figure 5.12: Availability of Navigation Updates with DGPS and UWB Augmentation for High-Multipath Outdoor Urban Environment

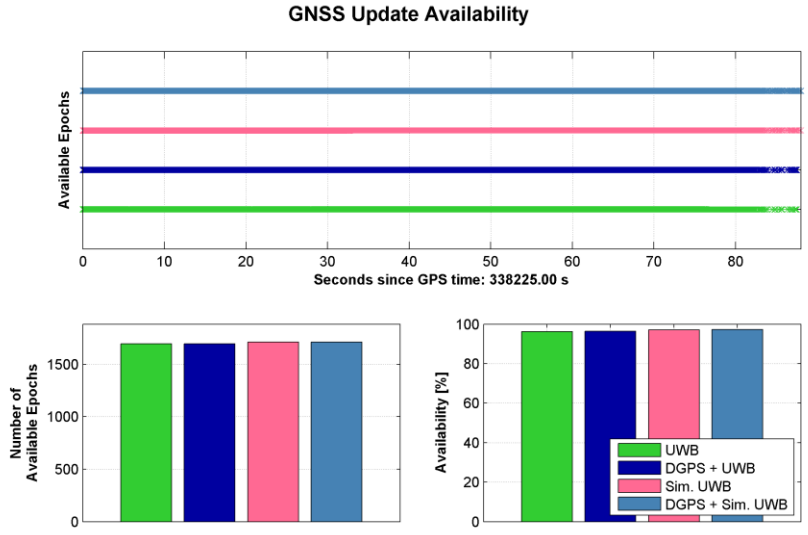

Figure 5.13: Availability of Navigation Update with DGPS and Simulated UWB Augmentation for High-Multipath Outdoor Urban Environment

5.4.1.2 Indoor Urban Environment

Figure 5.14 and Figure 5.15 shows the indoor navigation solution availability for the vector-based GNSS receivers discussed in Section 5.4.1.1. Once again, the vector-based GNSS receivers using DGPS corrections and real-world UWB measurements are first presented in Figure 5.14; this is then followed by the vector-based GNSS receivers using simulated UWB measurements shown on Figure 5.15.

Upon comparing the availability of navigation updates on the vector-based receivers shown on Figure 5.14, the most notable finding is that the availability of the DGPS-only vector-based GNSS receiver has a much higher availability than the UWB augmented DGPS receiver. This comes as a surprise since a receiver using DGPS corrections not only has larger pseudorange measurement errors, but also greater positioning errors as seen in Section 5.4.2. However, upon inspecting the velocity error statistics for the indoor period (Figure 5.21), it was found that the vector-based GNSS receiver using only DGPS corrections also had noticeably lower velocity errors compared to the stand-alone and DGPS+UWB vector-based receivers. Since GNSS signal tracking performance is more sensitive to frequency tracking errors and any velocity errors from the navigation solution on a vector-based receiver will lead to frequency tracking errors, this stands to explain the marginal increase in the availability of navigation solution updates for the vector-based receiver using DGPS corrections.

Meanwhile, when comparing the solution availability of the UWB augmented GNSS receiver with the stand-alone vector-based receiver, it was found that the UWB

augmented receiver had a slightly greater availability. This is primarily due to the fact that the UWB measurements allowed the GNSS receiver to update its navigation solution even in the absence of available GNSS measurements. Moreover, like the DGPS assisted vector-based GNSS receiver discussed earlier, the UWB augmented receiver also had noticeably smaller velocity errors which resulted in marginally better tracking performance indoors.

Lastly, the receiver making use of both DGPS corrections and UWB measurements showed the poorest performance. The most likely explanation for this is due to the discrepancy between the corrected GNSS pseudorange observations and the UWB range measurements. The frequency tracking performance of a vector-based GNSS receiver is dependent on three factors: the frequency stability of onboard oscillator, the accuracy of the velocity estimate in the navigation solution, and the accuracy of the receiver clock drift estimate. Although for the test setup, the oscillator used was a very high quality double-ovenized crystal oscillator, the velocity estimates of the navigation solution depended on the quality of the GNSS and UWB measurements. Although the receiver velocity can be directly observed using GNSS Doppler measurements, it can also be estimated using pseudorange and range measurements within a Kalman filter; because of this, if there large discrepancies exists between GNSS pseudorange measurements and UWB range measurements due to multipath or receiver noise from DGPS corrections, significant jumps in the receiver's estimated position over a short interval have the potential to induce significant velocity errors into the navigation solution.

Moreover, in an optimally tuned Kalman filter where the measurement variance and spectral density of the states, as represented by R and Q matrices, are accurately determined, the lack of Doppler observations combined with poor velocity estimates should not induce large errors in the receiver clock drift estimate. However, in order to maintain tracking stability under the operating conditions presented in this analysis, it was found that the navigation solution must be highly constrained in order to maintain reliable and robust vector-tracking in open-sky environments. This leads to an inherent over-constraint in the random-walk velocity model used for this analysis; thus the Kalman filter used was not tuned to capture the full range of receiver dynamics, rather, it was tuned to maximize tracking sensitivity and stability. With this in mind, it is also important to note that the receiver clock drift can only be directly observed with GNSS Doppler measurements; for the Kalman filter used in this analysis, changes in receiver clock bias over time will allow the filter to estimate the clock drift. However, this leads to less accurate and noisier clock drift estimates due to errors in pseudorange measurements. Because there is a strong correlation between the receiver clock drift and velocity states, in light-indoor environments where only one or two Doppler measurements are available, there may not be a sufficient number of Doppler measurements to separate the receiver clock drift and velocity components. Under these unique situations, large velocity errors generated by pseudorange or ranging errors may lead to gross errors in the receiver clock drift estimates and cause a vector-based GNSS receiver to lose lock on all channels, thereby reducing the navigation solution availability indoors.

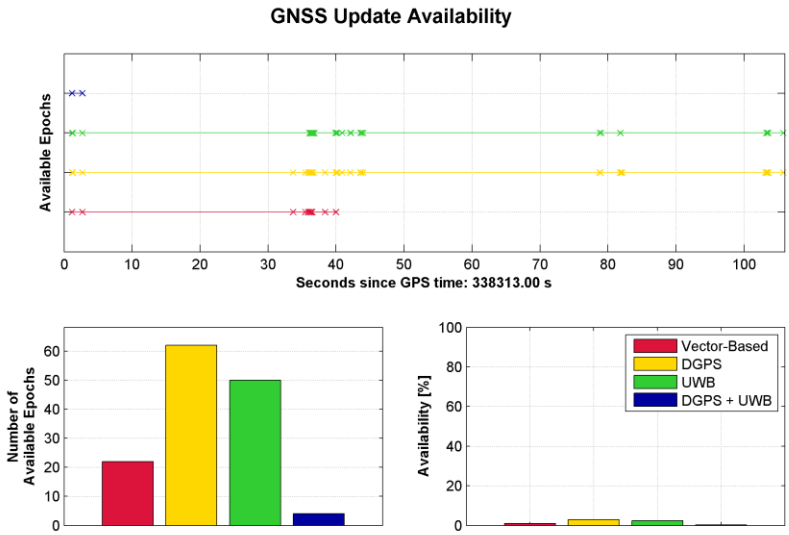

Figure 5.14: Availability of Navigation Update with DGPS and UWB Augmentation for Indoor Urban Environment

Despite the poor performance of a combined DGPS and UWB solution using real-world UWB range measurements, it was found in Figure 5.15 that combining of DGPS corrections and simulated UWB measurements yielded a marginal improvement in the navigation solution availability as compared to using only simulated UWB range measurements. The two primary differences between the real-world and simulated UWB measurements is the measurement availability and the ranging accuracy. For the real-world UWB data, measurements are susceptible to large ranging errors due to multipath; these errors result in a large standard deviation for a set of range measurements that are made for a single measurement epoch which results in discarded measurement epochs during the pre-filtering UWB measurements. In the case of the indoor scenario, few tens

of UWB measurement epochs were available which accounted for the very low navigation solution availability. On the other hand, simulated UWB range measurements were available throughout the entire duration of the indoor test; this resulted in a significantly greater number of navigation solution updates. Because of the regular availability of UWB range measurements, the navigation filter is capable of constraining the velocity estimate for the receiver. By taking advantage of better constrained velocity estimates, the receiver can make more accurate estimates of the clock drift during periods where the availability of Doppler measurements are limited. In turn, this improves the robustness of the vector-based tracking loops.

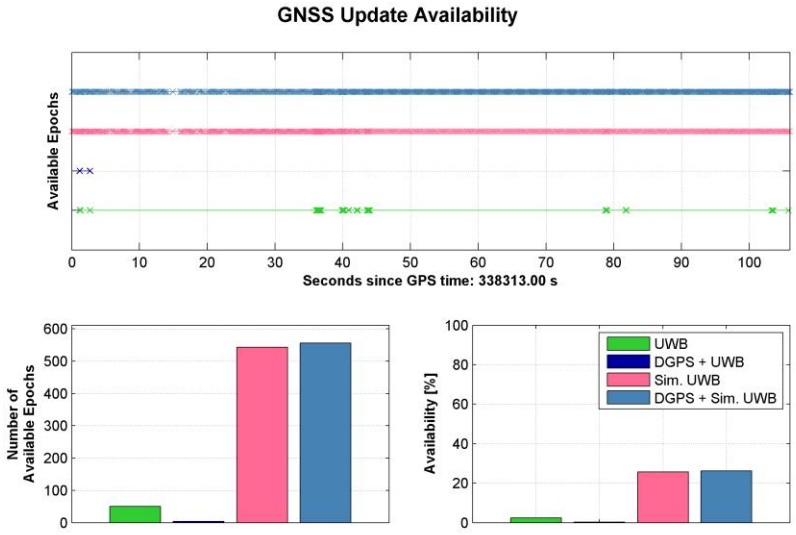

Figure 5.15: Availability of Navigation Update with DGPS and Simulated UWB Range Augmentation for Indoor Urban Environment

5.4.2 Navigation Accuracy

In this subsection, the effects of vector-based GNSS receiver augmentation using DGPS corrections and UWB range measurements are examined in the context of positioning and velocity estimation accuracy. Like the previous subsections that examine tracking performance and navigation solution availability, the navigation solution accuracy is assessed separately for two different environments – a high-multipath outdoor urban environment, and an indoor urban environment with strong GNSS signal attenuation.

5.4.2.1 High-Multipath Outdoor Environment

Figure 5.16 and Figure 5.17 shows the positioning error statistics for the vector-based GNSS receivers operating in a high-multipath area using observed and simulated UWB range measurements respectively. Upon examining Figure 5.16, the most noticeable effect of vector-based GNSS receiver augmentation is the increase in horizontal positioning error due to the addition of DGPS corrections and a noticeable decrease in vertical positioning error. As expected, the addition of DGPS corrections to pseudorange measurements noticeably reduced systematic biases and resulted in an improvement in the vertical positioning accuracy due to the reduction of tropospheric range delay and ionosphere errors. Another expected outcome of adding DGPS corrections is the increase in stochastic errors due to the linear combination of two random processes.

What is not immediately apparent is the cause of the large increase in the mean horizontal positioning error coupled with a rather small increase in the horizontal positioning error's standard deviation. The primary reason for this is due to the incorporation of additional multipath errors introduced through the DGPS corrections. Since multipath errors change slowly, on the order of minutes for a static receiver, the pseudorange errors introduced by the DGPS corrections also change slowly over time. Moreover, the total duration of the data collection was only several minutes in total, the multipath errors introduced through DGPS corrections appear and act as measurement biases rather than stochastic errors such as measurement noise. As the rover receiver is kinematic, the Kalman filter states must be allowed to change quickly over time; as such, slowly changing multipath errors introduced by the DGPS corrections from the static reference receiver cannot be filtered out by the rover's navigation filter.

Another observation from Figure 5.16 is the minor increase in receiver positioning error due to the addition of UWB range measurements; this effect is primarily attributed to random errors, uncompensated scale factor and biases in the UWB range measurements, and imperfections in the time synchronization between UWB and GNSS measurements.

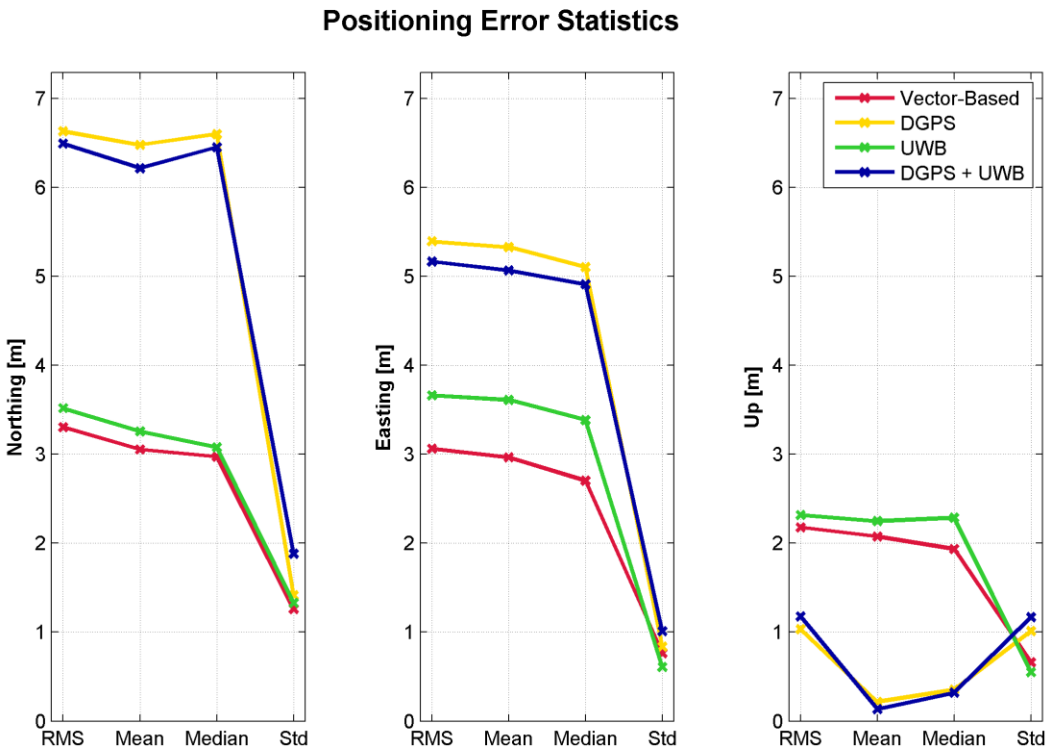

Figure 5.16: Positioning Error Statistics for a High-Multipath Urban Environment using DGPS Corrections and Real-World UWB Range Measurements

Figure 5.17 compares the positioning error statistics for vector-based GNSS receivers using real-world and simulated UWB range measurements. What is immediately apparent in this figure is that, under best case scenarios where error free UWB range measurements are available continuously, the horizontal positioning error of a vector-based GNSS receiver can be greatly improved. For the test scenario presented, since all three simulated UWB radios were located at a similar elevation as that of the mobile station, the simulated UWB ranges alone do not allow the mobile receiver to accurately estimate its height. As a matter of fact, because the UWB range measurements allow the navigation filter to greatly improve the positioning accuracy and positioning uncertainty in the horizontal direction, the GNSS observations that are available are primarily used to estimate the receiver height. Because the GNSS measurements tend to have relatively large measurement errors from multipath and receiver noise, these errors are forced into the vertical component of the positioning estimate at each GNSS measurement update. Once again, since the navigation solution on a vector-based GNSS receiver needs to be constrained with a low spectral density value to ensure stability in the GNSS tracking loops, measurement errors that contribute to a positioning error appear as a bias over time, thereby increasing the mean error rather than the standard deviation.

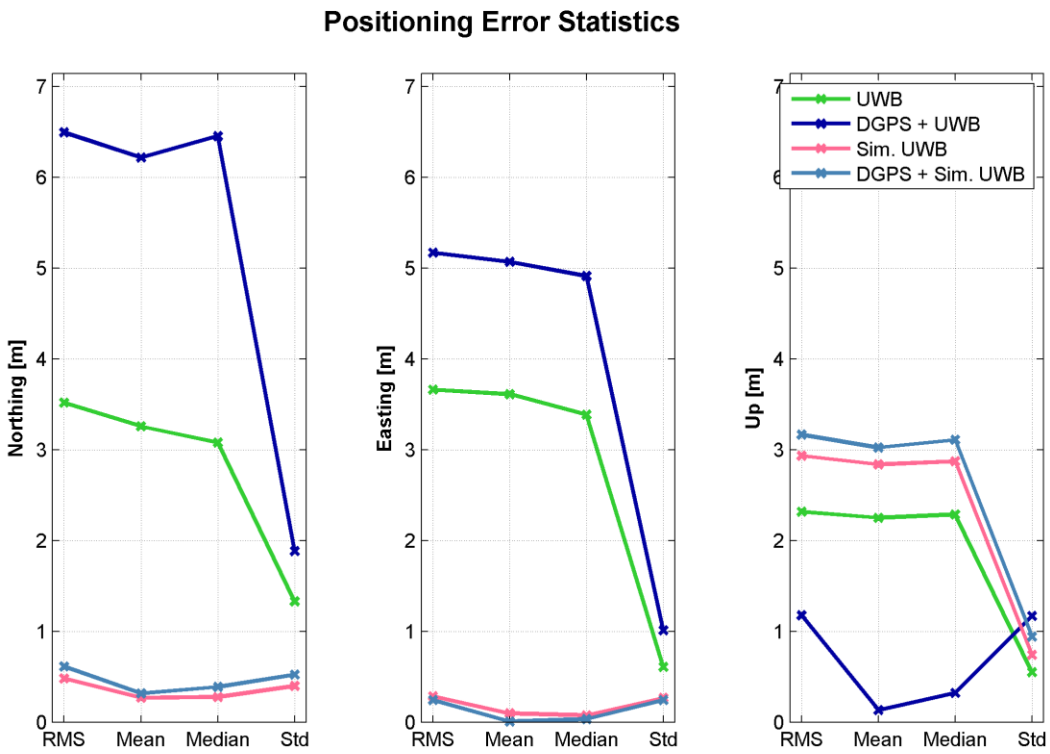

Figure 5.17: Positioning Error Statistics for a High-Multipath Urban Environment using DGPS Corrections and Simulated UWB Range Measurements

Another important note to make on the combination of DGPS corrections with simulated UWB range measurements is that using DGPS corrections may not necessarily improve positioning accuracy. Even though the DGPS corrections can reduce systematic biases caused by satellite position errors, ionosphere errors, and troposphere delay, when applying DGPS corrections to a vector-based GNSS receiver that require a highly constrained navigation solution in a high-multipath environment, the increase in

stochastic errors from DGPS corrections can have a more negative effect on positioning accuracy than the positive effects that a reduction of systematic bias may bring.

Having examined the positioning error statistics, the velocity error statistics for the mobile receiver is shown on Figure 5.18 and Figure 5.19. In Figure 5.18 where real-world UWB measurements are used, the stand-alone and UWB augmented vector-based receivers had very similar performance. This is partly due to the fact that the availability of UWB measurements was fairly limited and thus did not have a large effect on the velocity accuracy of the receiver. When DGPS corrections were used in combination with UWB ranges however, a noticeable increase in velocity errors can be seen. This accounts for the poorer tracking performance of the vector-based GNSS receiver making use of both DGPS corrections and UWB ranges discussed in Section 5.3.1.1.

When using simulated UWB range measurements, it was found that that the improvement in ranging accuracy and availability helped to improve the horizontal velocity accuracy, especially when DGPS corrections were used. Like the positioning error where only an improvement was observed in the vertical direction, the same can be said about the velocity error statistics; once again, this is due to the geometry of the simulated UWB radio setup where the UWB radios were located at approximately the same height as the mobile receiver.

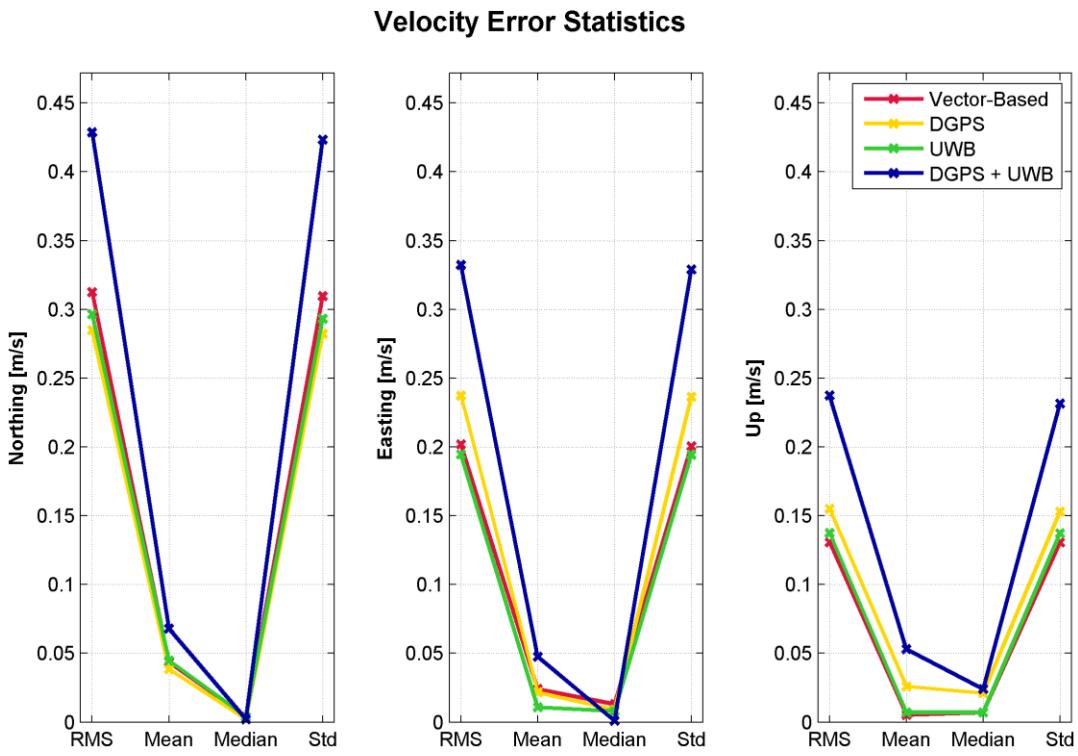

Figure 5.18: Velocity Error Statistics for a High-Multipath Urban Environment using DGPS Corrections and Real-World UWB Range Measurements

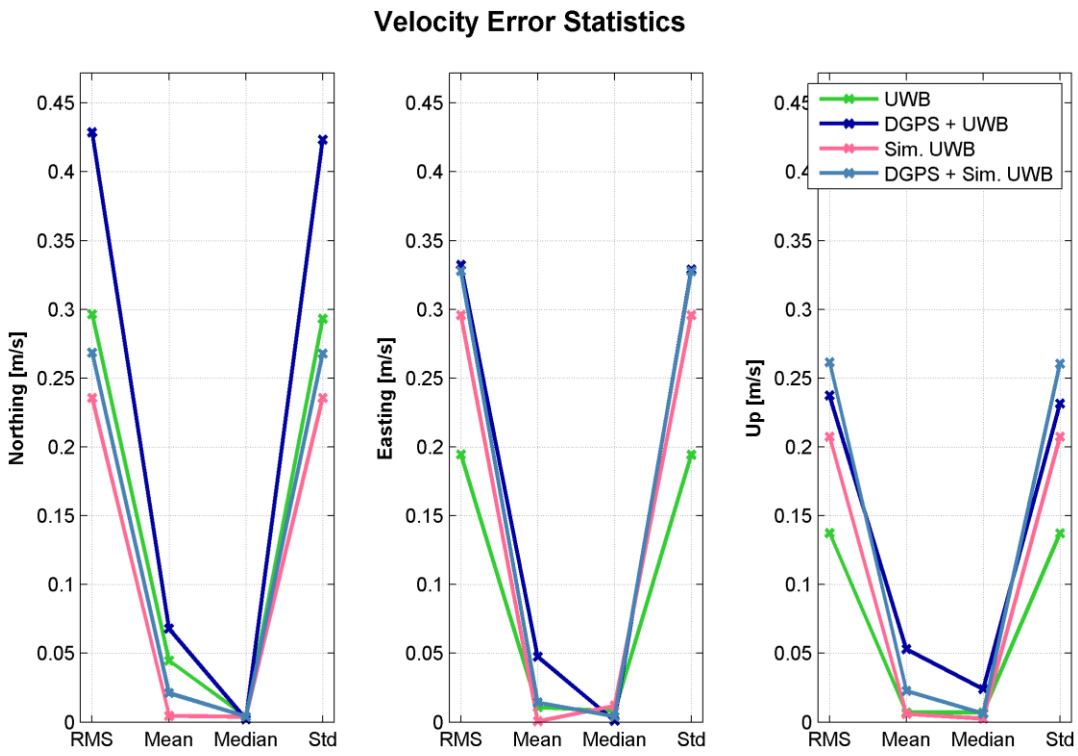

Figure 5.19: Velocity Error Statistics for a High-Multipath Urban Environment using DGPS Corrections and Simulated UWB Range Measurements

5.4.2.2 Indoor Urban Environment

Positioning and velocity error statistics that show the effects of DGPS corrections and UWB range augmentation is shown from Figure 5.20 to Figure 5.23. Based on the results shown on Figure 5.20, the use of DGPS corrections in an indoor environment had the most detrimental impact on the positioning accuracy of a vector-based GNSS receiver. However, DGPS corrections had little impact on the velocity error which is shown in Figure 5.21; this is primarily due to the fact that Doppler observations are unaffected by the DGPS corrections which are only applied to pseudorange measurements.

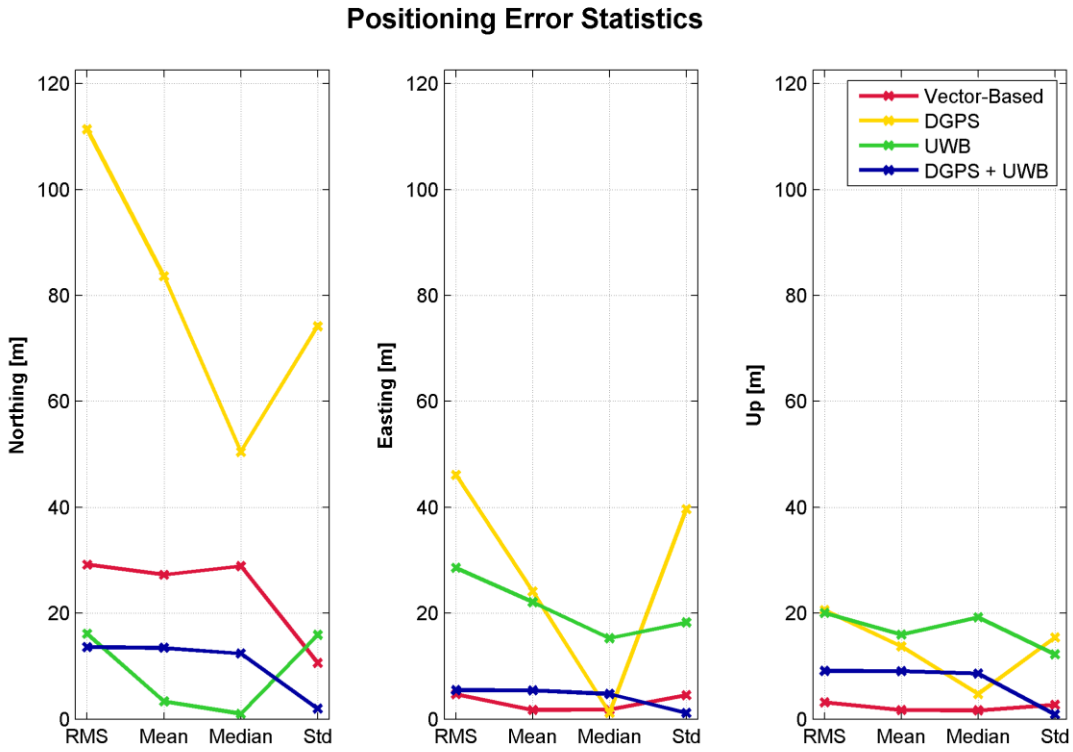

Figure 5.20: Positioning Error Statistics for Indoor Urban Environment using DGPS Corrections and Real-World UWB Range Measurements

When UWB range measurements are combined with DGPS corrections, the positioning error of the solution appeared to improve significantly. However, it must be noted that the navigation solution using both DGPS corrections and UWB measurements had the lowest availability. In fact, it must be pointed out that a position solution was only available for the first 5 seconds in the indoor dataset when DGPS corrections and UWB measurements were used together. Recalling Figure 5.14, it is possible to see that the position availability when using both real-world UWB range measurements and DGPS corrections was drastically less than using only DGPS corrections or UWB ranges as a means of receiver aiding. With this in mind, the positioning and velocity error statistics shown for the receiver using real-world UWB range measurements and DGPS corrections while operating in an indoor environment are based on very few available epochs and do not provide a clear indication of the actual navigation accuracy for the DGPS and UWB augmented receiver. A similar note can be made regarding the navigation error statistics for stand-alone vector-based GNSS receiver as well as the vector-based receiver making use of real-world UWB range measurements.

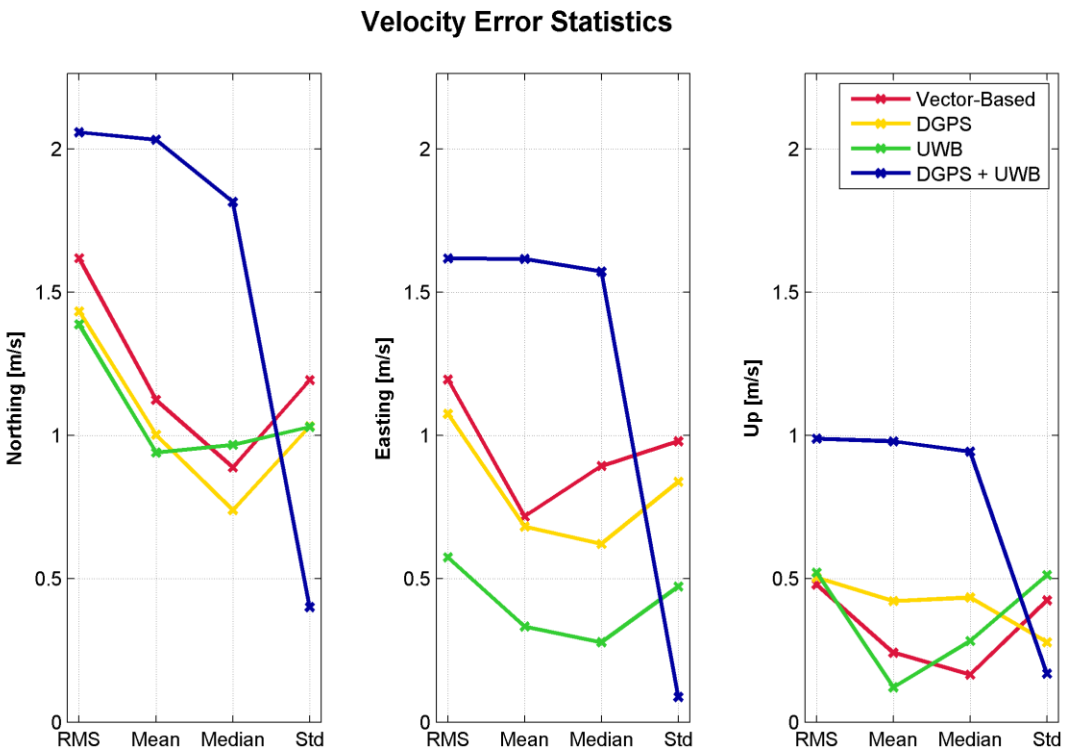

Figure 5.21: Velocity Error Statistics for Indoor Urban Environment using DGPS Corrections and Real-World UWB Range Measurements

While making use of simulated UWB range measurements that provided continuous availability of error free range measurements, the vector-based GNSS receivers showed a noticeable improvement in the positioning and velocity accuracy which was expected. Here, it was found that the inclusion of DGPS corrections to the UWB augmented vector-based GNSS receiver made a minor impact on the positioning error in the northing direction. The primary reason for this difference is that while the receiver was indoors, only one satellite measurement was available at any given time and it was found that when using DGPS corrections, the receiver was able to reject a pseudorange observation that contained a 35 metre blunder. In contrast, the very same blunder which was not rejected in the simulated UWB augmented GNSS receiver produced a large error in both the velocity and position estimate and led to the reduced performance of the UWB-only receiver. It should be noted that the DGPS corrected pseudorange measurements were weighted differently compared to uncorrected pseudorange measurements; the DGPS corrected pseudoranges had an a priori variance two times greater than that of uncorrected pseudorange measurements in order to account for the increase in receiver noise.

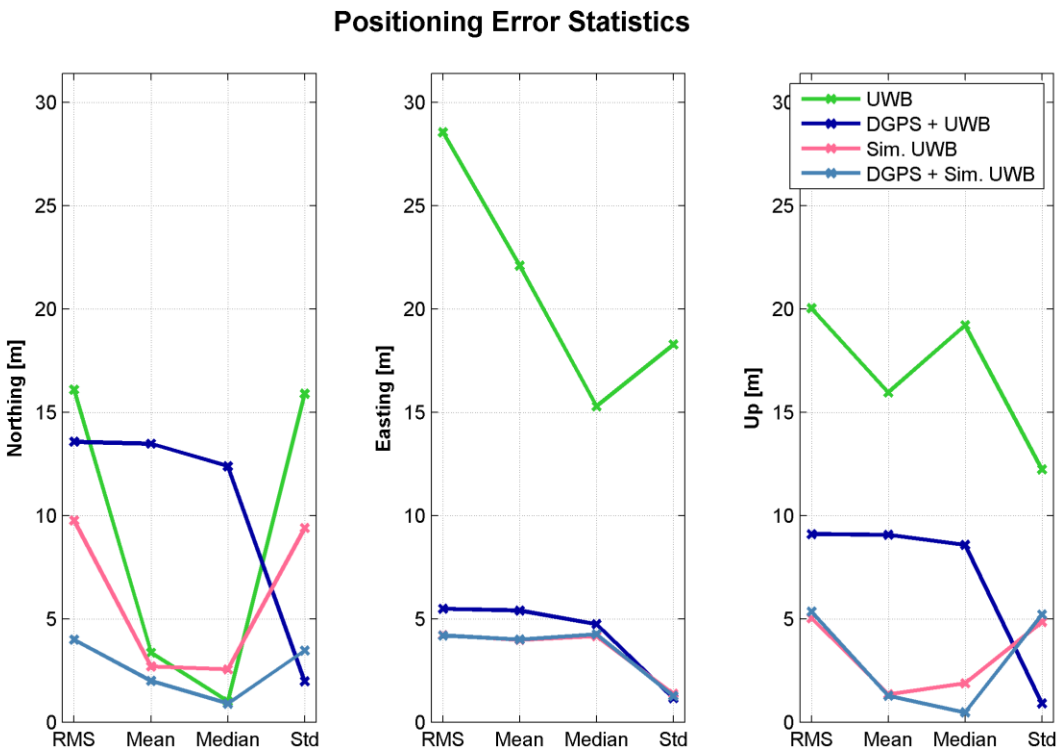

Figure 5.22: Positioning Error Statistics for Indoor Urban Environment using DGPS Corrections and Simulated UWB Range Measurements

By comparing the results between vector-based GNSS receivers that made use of only simulated UWB measurements and one that also incorporated DGPS corrections, it was found that the proper detection and rejection of blunder observation can play a critical role in the tracking stability, availability, and navigation accuracy of the receiver. Although DGPS corrections tended to impart a negative effect on navigation accuracy under high multipath environments, it was found that in certain circumstances, they may

allow a receiver to detect and remove observation blunders and improve the overall performance of the receiver.

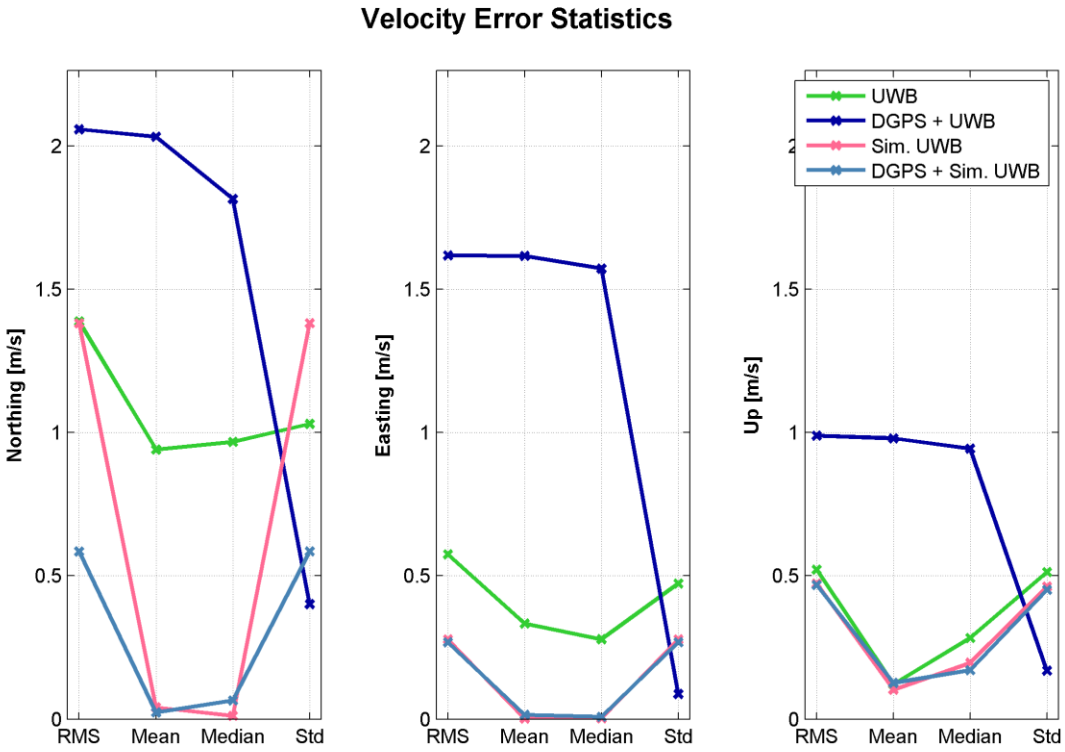

Figure 5.23: Velocity Error Statistics for Indoor Urban Environment using DGPS Corrections and Simulated UWB Range Measurements

5.5 Summary

In this chapter, the effect of augmenting a vector-based GNSS receiver with DGPS corrections and UWB ranging was examined for a high-multipath outdoor urban environment and an indoor weak signal environment. Due to the limitations of real-world UWB measurements presented in this chapter, the use of simulated UWB range measurements were also examined in order show how a vector-based GNSS receiver may perform in a best-case scenario where accurate UWB ranging measurements are made continuously available during the test. The following summarizes the key findings of this chapter.

From results presented in this chapter, it was found that in an outdoor high-multipath environment, the reduction of systematic biases in GNSS pseudorange observations may not necessarily result in any improvement on the horizontal positioning accuracy due to the introduction of additional multipath and receiver noise errors present in DGPS corrections. Although an improvement in vertical positioning accuracy was observed, the increase in stochastic errors in the corrected pseudorange observations also had a negative effect on the velocity error of the vector-based GNSS receiver. This increase in velocity error led to reduced tracking performance of the vector-based receiver and resulted in a reduction in the availability of GNSS observations. With this in mind however, it was also found that in an indoor environment, DGPS corrections can potentially allow a navigation filter to reject measurement blunders that otherwise would not be detected. As a result, the correct rejection of a single measurement blunder led to a noticeable improvement in the navigation solution accuracy of a vector-based GNSS

receiver which made use of both DGPS corrections and simulated UWB range measurements.

Although already discussed in Section 5.2, it must be restated that the negative effect that adding DGPS corrections had on the GNSS receiver performance is strictly attributed to the placement of the DGPS reference receiver in a high multipath environment; the DGPS reference receiver was placed in such an environment due to limitations in the equipment logistics at the time of the data collection for this experiment. Under ideal circumstances, a DGPS reference receiver should be placed in an open-sky, low multipath environment; in such ideal situations, adding differential GNSS corrections should not have a negative impact on GNSS receiver performance.

When using real-world UWB range measurements in a vector-based GNSS receiver, its effect was harder to observe; the primary reason for this was a lack of continuously available UWB measurements throughout the entire test period. Because the UWB radios used were susceptible to large ranging errors due to multipath, many of the UWB measurements that were originally observed had to be rejected. As a result of this, it was found that real-world UWB measurements, when available, improved the availability of a navigation solution especially in an indoor environment. However, this increase in solution availability was marginal at best. Because the availability of real-world UWB range measurements was quite irregular and sparse, the navigation solution of the UWB aided receiver was similar to that of a stand-alone vector-based GNSS receiver. Unlike the stand-alone receiver however, when UWB measurements became available, they

usually led to sudden jumps in the receiver's estimated position. These jumps in position resulted increase velocity errors that also had a negative effect on the tracking performance of the vector-based GNSS receiver. This negative effect was noticeable when both DGPS corrections were combined with real-world UWB range measurements.

In order to fully appreciate the effect of UWB augmentation on a vector-based GNSS receiver, simulated error-free UWB measurements were used. In the case where UWB range measurements is continuous available, the UWB augmentation did have a positive effect on the vector-based GNSS receiver. Not only did the availability of the navigation solution improve due to the addition of UWB range measurements, the UWB measurements also served to improve the accuracy of the receiver's velocity estimate when GNSS Doppler observations were not available indoors. This in, in turn, led to an improvement in track performance on the vector-based GNSS receiver.

Chapter Six: Summary and Conclusion

6.1 Overview

This chapter provides a brief summary along with concluding remarks based on the results discussed in preceding chapters.

6.2 Summary

The objective of this research, as described in Chapter 1, was to study the effects of combing DGPS corrections and UWB range measurements to aid a vector-based GNSS receiver. In particular, differences in receiver performance were compared in the following areas:

- GNSS tracking sensitivity
- GNSS measurement quality
- Navigation solution availability
- Navigation accuracy

Specific background information related to Software GNSS receiver design, GNSS error sources, DGPS positioning, and UWB ranging were discussed in Chapter 2. Details reviewed in Chapter 2 provide the information needed to understand the DGPS and UWB aided vector-based software GNSS receiver architecture used in this research.

Two large-scale data collections were performed to acquire the necessary real-world GNSS and UWB measurements needed to evaluate the effects of DGPS and UWB aiding

on a vector-based GNSS receiver. For both data collections discussed in this research, the GNSS receiver was initialized in an outdoor environment. Doing this allowed this research to focus on evaluating the *tracking* and *navigation* performance of the vector-based GNSS receiver rather than the *acquisition* of weak GNSS signals. Furthermore, by collecting IF samples of the incoming GNSS signal using an RF front-end, it was possible use a software GNSS receiver to reprocess the *same* IF data with different receiver aiding techniques such as DGPS corrections and UWB ranging.

In the first data collection, the test environment chosen was that of a traditional North American timber-framed house described in Chapter 3. Here, the performance between a standard scalar tracking GNSS receiver and a vector-based GNSS receiver was compared to illustrate the benefits that a vector-based GNSS receiver architecture. The receivers used in this analysis consisted of a scalar tracking and vector-based tracking software GNSS receiver which are named GSNRx™, and GSNRx-vb™ respectively; both software GNSS receivers were developed by the Position Location And Navigation (PLAN) Group at the University of Calgary.

In the second data collection, a more challenging urban environment was used for determining the impact of DGPS and UWB aiding on a vector-based software GNSS receiver. Modifications were made to GSNRx-vb™ to allow the software receiver to take advantage of DGPS corrections and UWB range measurements. Details of the receiver modifications made and the equipment needed for testing were presented in Chapter 4. Using the data collected from the urban environment, the impact of DGPS and UWB

aiding were examined in Chapter 5; these findings are summarized in the conclusion section below.

6.3 Conclusion

Concluding remarks based on findings from Chapter 5 are provided in this section. Statements that are specific to a particular environment are presented in their respective subsection; statements that apply to both environments are discussed directly below.

The impact of using DGPS corrections and UWB ranging for aiding a vector-based GNSS receiver was evaluated in four specific areas, namely:

1. Tracking sensitivity and robustness
2. GNSS measurement quality
3. Navigation solution availability
4. Navigation accuracy

In this research, it was found that the robustness of a vector-based tracking loop is related to the quality of the measurements used in the navigation filter – more specifically: pseudorange, Doppler, and range measurements. Stochastic errors such as noise and multipath result in a less stable navigation solution; erratic changes in the velocity and receiver clock drift estimates result in more frequent loss of signal lock due to the poor frequency estimates of the incoming GNSS signals. A prolonged period in which many receiver channels experience loss of lock will result in a deterioration of the navigation

solution and overall tracking stability. Based on this, it was found that the tuning of the navigation filter had a large impact on the tracking stability for a vector-based GNSS receiver. In particular, a loosely constrained navigation filter that allows for large changes in receiver dynamics is also less adept in smoothing out sudden changes in position and velocity due to measurement errors. As a result, a loosely constrained navigation filter will lead to a decrease in robustness when tracking weaker, non-line of sight GNSS signals that were otherwise reliably tracked when using a more tightly constrained navigation filter.

6.3.1 High-Multipath Outdoor Urban Environment

When operating in a high-multipath outdoor urban environment, it was found that when only using UWB ranging to aid a vector-based GNSS receiver, the tracking sensitivity for non-line of sight signals were marginally better but very similar to an unaided vector-based GNSS receiver. On the other hand, adding poor quality DGPS corrections for receiver aiding either as a stand-alone source of aiding or in combination with UWB ranging resulted in a 6-12 dB-Hz drop in C/N_0 due to an increase in velocity errors which led to a degradation in the prediction of the incoming signal frequency. Similarly, it was found that for a high-multipath outdoor environment, pseudorange measurement residuals for a UWB aided vector-based receiver was very similar to that of an un-aided vector-based GNSS receiver. However, the addition of poor quality DGPS corrections led to an overall increase in the magnitude of the pseudorange residuals. The DGPS corrections used were deemed to be of poor quality due to the DGPS reference station being located in a high multipath environment. Under normal circumstances, a DGPS reference station

should always be placed in a low multipath environment; however this was not possible due to limitations in equipment logistics.

For outdoor environments where direct line of sight signals are continuously available, the navigation solution availability was similar between aided and unaided vector-based receivers. This is due to the fact that a Kalman filter was used for navigation and only one GNSS measurement is needed for a filter update.

When using real-world UWB range measurements, positioning accuracy of the navigation solution was marginally degraded due to ranging errors from UWB measurements. In the high-multipath outdoor environment, horizontal positioning accuracy for both the unaided vector-based GNSS receiver and UWB aided vector-based receiver remained between 2-3 metres RMS while vertical positioning accuracy was around 2.3 metres RMS. When simulated, error-free UWB measurements were used to aid the vector-based GNSS receiver, horizontal positioning accuracy improved to the sub-metre level while vertical positioning accuracy degraded to approximately 3 metres.

DGPS corrections either used as a stand-alone source of aiding or in combination with UWB ranging had a negative effect on the positioning accuracy. Horizontal positioning error grew from 3-4 metres RMS without any form of aiding, to 5-6.5 metres RMS; meanwhile, vertical positioning errors were reduced from 2.2 metres RMS to around 1 metre RMS.

6.3.2 Indoor Urban Environment

For an indoor urban environment where no line of sight signals exist, it was found that when used individually for aiding a vector-based GNSS receiver, both DGPS corrections and UWB ranging resulted in improved tracking sensitivity on the order of 2-3 dB-Hz in C/N_0. However, for very weak signals, no appreciable differences were observed between aided and unaided receivers. It was also found that combining UWB ranging and poor quality DGPS corrections resulted in a reduction in tracking sensitivity; this was witnessed in the form of a drop in C/N_0 by 3-6 dB-Hz.

Due to the limited number of GNSS observations available and the lack of reliable estimates for the receiver clock states while operating in the indoor environment, it was not possible to make a definitive judgement on the quality of the observation measurements based on their residuals. However, it can be said that in an environment where the availability of GNSS measurements are significantly limited, the addition of UWB range measurements can greatly improve the overall navigation solution availability. The extent to which UWB range measurements can improve the navigation solution availability is based on the availability and update rate of reliable UWB range measurements; here, reliable UWB range measurements is defined as UWB range measurements that do not cause sudden jumps in the receiver velocity and clock drift estimates in which the stability of the vector-based tracking loop will be compromised.

The navigation solution accuracy for a vector-based GNSS receiver operating in an indoor urban environment can be greatly improved through the use of UWB ranging. As is the case for the high-multipath outdoor urban environment, the navigation solution accuracy when using UWB ranging as a form of receiver aiding, is a function of the accuracy of the UWB range measurements. In cases where error-free UWB range measurements are made available for receiver aiding, a horizontal positioning accuracy better than 10 metres RMS can be achieved indoors; this is in contrast to the 30 metre RMS error observed on an un-aided vector-based GNSS receiver. Lastly, the use of poor quality DGPS corrections had very large negative impact on the navigation accuracy of the vector-based GNSS receiver; in the indoor environment, the horizontal positioning errors grew from 30 metres without any aiding to over 110 metres RMS with DGPS corrections applied. As mentioned in the previous subsection, under normal circumstances, the use of DGPS corrections should not negatively impact GNSS receiver performance; however, due to limitations in logistics during the data collection for the experiment presented in Chapter 5, the DGPS reference station could not be placed in a low multipath environment. Because of this, the DGPS corrections generated by the DGPS reference station were corrupted in large multipath errors that had a negative impact on the DGPS results presented. Under normal circumstances, it should be expected that the use of DGPS corrections should, in general, improve the performance of a GNSS receiver.

6.4 Future Work

On a vector-based GNSS receiver, the velocity and clock drift estimates from the navigation filter are used to control the NCO for each tracking loop. When using a 20 ms coherent integration period on the GPS L1CA signal, a line-of-sight velocity error of 6.3 m/s between the receiver and satellite can result in a loss in sensitivity of over 7 dB (van Diggelen 2009c). Because of this, an accurate estimate of the receiver velocity is essential to a stable and robust vector-based tracking loop. Based on the findings of this research, the most prominent problems that limited the performance of the UWB and DGPS aided vector-based GNSS receiver presented in this work are the:

1. Lack of GNSS Doppler observations to directly and reliably observe both the receiver velocity and clock drift states while operating indoors
2. Inaccurate estimates of the receiver velocity and incoming signal frequency when using unbiased UWB measurements and biased (from slowly changing multipath errors) DGPS corrections

To address the first problem, several potential solutions exist, including:

- Using multiple GNSS constellations in order to increase satellite availability
- Improving the velocity estimate through other sensors such as accelerometers, speed sensors, acoustic Doppler velocimetres, and inertial measurement units (i.e. ultra-tight coupling)

In this work, the method used to address the second problem was to increase the constraint on the random-walk velocity model in the navigation filter. Although this improved tracking robustness, this method has a major drawback in that it does not allow

for high-dynamics applications. Other means of addressing velocity errors caused by poor quality DGPS corrections include:

- Placing a reference receiver antenna in a low multipath environment such as on the roof of a building with very few multipath reflectors
- Employing alternative means of reducing satellite orbit and clock errors, tropospheric delay, and ionosphere errors by using precise satellite ephemerides, improved tropospheric modelling, and more accurate ionosphere modelling respectively; these techniques are similar to those used in single receiver Precise Point Positioning (PPP)
- Combining a vector-based GNSS receiver architecture with a block-processing approach whereby DRC are performed on several nearby frequencies to reduce the chance of sensitivity degradation due to errors in the receiver velocity estimate
- Increasing the update rate and availability of real-world UWB measurements in order to improve the accuracy of the receiver velocity estimate
- Ensuring proper synchronization of UWB and GNSS measurements in order to reduce the effect of combining biased and unbiased observations which may lead to sudden changes in position estimates which, in turn, leads to increased errors in the receiver velocity estimate; to achieve this, UWB measurement generation would need to be made at the same instances as GNSS measurements
- In open-sky environments where a PLL can be used reliably, carrier-phase smoothing of pseudorange measurements can be used to improve the position and receiver clock bias estimates; this will also benefit the receiver velocity and clock drift estimates when using a Kalman filter for navigation

Works Cited

Aminian, B. (2011) *Investigations of GPS Observations for Indoor GPS/INS Integration*, MSc Thesis, published as Report No UCGE Report Number 20339, University of Calgary, pp. 171, Department of Geomatics Engineering

ARINC Research Corporation (2000) *Navstar GPS Space Segment / Navigation User Interfaces*, Technical Report No. ICD-GPS-200C, Interface Control Document, U.S. Department of Homeland Security and United States Coast Guard, pp. 138, The Navigation Center of Excellence (Available at http://www.navcen.uscg.gov/pubs/gps/icd200/ICD200Cw1234.pdf)

Benson, D. (2007) "Interference Benefits of a Vector Delay Lock Loop (VDLL) GPS Receiver," in *Proceedings of the Proceedings of the 63rd Annual Meeting of The Institute of Navigation, ,* Cambridge, MA, The Institute of Navigation, pp. 749-756

Chan, B. and M. G. Petovello (2011) "Collaborative Vector Tracking of GNSS Signals with Ultra-Wideband Augmentation in Degraded Signal Environments," in *Proceedings of the Proceedings of the 23rd International Technical Meeting of The Satellite Division of The Institute of Navigation, ,* San Diego, CA, The Institute of Navigation, pp. 404-413

Chiu, D. S.T. (2008) *Ultra Wideband Augmented GPS*, Technical Report No. 20277, MSc Thesis, published as Report No UCGE 20277, University of Calgary, pp. 172, Department of Geomatics Engineering (Available at http://plan.geomatics.ucalgary.ca/papers/08.20277_dchiu.pdf)

Conley, R., R. Cosentino, C. J. Hegarty, E. D. Kaplan, J. L. Leva, M. Uijt de Haag, and K. Van Dyke (2006a) "Measurement Errors," [Chapter 7] in *Understanding GPS: Principles and Applications, 2nd Ed*, Artech House, Boston, MA, 302-319

Conley, R., R. Cosentino, C. J. Hegarty, E. D. Kaplan, J. L. Leva, M. Uijt de Haag, and K. Van Dyke (2006b) "Performance of Stand-Alone GPS," [Chapter 7] in *Understanding GPS: Principles and Applications, 2nd Ed*, Artech House, Boston, MA, 301-379

Derbez, and R. Lee (2008) "GPStream: A Low Bandwidth Architecture to Deliver or Autonomously Generate Predicted Ephemeris," in *Proceedings of the Proceedings of the 21st International Technical Meeting of the Satellite Division of The Institute of Navigation (ION GNSS 2008), ,* Savannah, GA, The Institute of Navigation, pp. 1258 - 1264

Federal Aviation Administration (2008) *Global Positioning System Wide Area Augmentation System (WAAS) Performance Standard*, Performance Standards Document, Federal Aviation Administration, pp. 28, Federal Aviation Administration

Groves, P. D. and C. J. Mather (2010) "Receiver Interface Requirements for Deep INS/GNSS Integration and Vector Tracking," in *Proceedings of the The Journal of Navigation , ,* Cambridge, UK, The Royal Institute of Navigation, pp. 471–489

Groves, P. D., C. J. Mather, and A. A. Macaulay (2007) "Demonstration of Non-coherent Deep INS/GPS Integration for Optimised Signal-to-noise Performance," in *Proceedings of the ION GNSS ITM 2007*, 25-28 September, Fort Worth, The Institute of Navigation, pp. 2627-2638

Hamm, C. R. and D. M. Bevly (2005) "Simulated Performance Analysis of a Composite Vector Tracking and Navigation Filter," in *Proceedings of the Proceedings of the 18th International Technical Meeting of the Satellite Division of The Institute of Navigation, ,* Long Beach, CA, The Institute of Navigation, pp. 478-487

Hegarty, C. J. (2006) "Least Squares and Weighted Least Squares Estimates," [Chapter A1] in *Understanding GPS: Principles and Applications, 2nd Ed*, Artech House, Boston, MA, 663-664

IGS Products (2010) *International GNSS Service*, http://igscb.jpl.nasa.gov/components/prods.html, last accessed October 21, 2010

Jost, T., M. Khider, and E. A. Sánchez (2010) "Characterisation and Modelling of the Indoor Pseudorange Error using Low Cost Receivers," in *Proceedings of the Proceedings of the 2010 International Technical Meeting of The Institute of Navigation, ,* San Diego, CA, The Institute of Navigation, pp. 277-284

Kim, K.H., G.I. Jee, and J.H. Song (2008) "Carrier Tracking Loop using the Adaptive Two-Stage Kalman Filter for High Dynamic Situations," in *International Journal of Control, Automation, and Systems*, Vol. VI, Issue 6, pp. 948-953

Krumvieda, K., P. Madhani, C. Cloman, E. Olson, J. Thomas, P. Axelrad, and W. Kober (2001) "A Complete IF Software GPS Receiver: A Tutorial about the Details," in *Proceedings of the Proceedings of the 14th International Technical Meeting of the Satellite Division of The Institute of Navigation, ,* Salt Lake City, UT, The Institute of Navigation, pp. 789-811

Lashley, M. and D. M. Bevly (2009) "What About Vector Tracking Loops?," *InsideGNSS*, vol. IV, May, Gibbons Media & Research LLC, Eugene, OR, pp. 16-21

Lin, T., C. O'Driscoll, and G. Lachapelle (2011) "Development of a Context-Aware Vector-Based High-Sensitivity GNSS Software Receiver," in *Proceedings of the Proceedings of the 2011 International Technical Meeting of The Institute of Navigation, ,* San Diego, CA, The Institute of Navigation, pp. 1043-1055

Ma, C., G. Lachapelle, and M. E. Cannon (2004) "Implementation of a Software GPS Receiver," in *Proceedings of the Proceedings of the 17th International Technical*

Meeting of the Satellite Division of The Institute of Navigation, , Long Beach, CA, The Institute of Navigation, pp. 956-970

Ma, M. S.H., C. O'Driscoll, and G. Lachapelle (2011) "Automatic Parameter Determination for Real-Time Acquisition using Frequency Domain Methods in a High Sensitivity Software Receiver," in *Proceedings of the Proceedings of the 2011 International Technical Meeting of The Institute of Navigation*, , San Diego, CA, The Institute of Navigation, pp. 1257-1269

MacGougan, G. D. and R. Klukas (2009) "Method and apparatus for high precision GNSS/UWB surveying," in *Proceedings of the Proceedings of the 22nd International Technical Meeting of The Satellite Division of The Institute of Navigation*, , Savannah, GA, The Institute of Navigation, pp. 853-863

MacGougan, G., K. O'Keefe, and R. Klukas (2009) "Ultra-wideband Ranging Precision and Accuracy," in *Measurement Science and Technology*, Vol. XX, pp. 13

MacGougan, G., K. O'Keefe, and R. Klukas (2010) "Tightly-coupled GPS/UWB Integration," in *The Journal of Navigation, The Royal Institute Of Navigation*, Vol. LXI, Issue 1, pp. 1-22

Misra, P. and P. Enge (2006a) "GPS in 2005: An Overview," [Chapter 2] in *Global Positioning System: Signals Measurements, and Performance, end Ed*, Ganga-Jamuna Press, Lincoln, MA, 37-41

Misra, P. and P. Enge (2006b) "GPS Measurements and Error Sources," [Chapter 5] in *Global Positioning System: Signals Measurements, and Performance, 2nd Ed*, Ganga-Jamuna Press, Lincoln, MA, 147-198

Mongrédien, C., G. Lachapelle, and M. E. Cannon (2006) "Testing GPS L5 Acquisition and Tracking Algorithms Using a Hardware Simulator," in *Proceedings of the Proceedings of the 19th International Technical Meeting of the Satellite Division of The Institute of Navigation*, , Fort Worth, TX, The Institute of Navigation, pp. 2901-2913

Mongrédien, C. (2008) *GPS L5 Software Receiver Development for High-Accuracy Applications*, PhD Thesis, published as Report No 20268, University of Calgary, pp. 191, Department of Geomatics Engineering (Available at http://plan.geomatics.ucalgary.ca/papers/dissertationfinal_cecilem_07may08_fordept.pdf)

Montenbruck, O. (2003) *Performance Assessment of the NovAtel OEM4-G2 Receiver for LEO Satellite Tracking*, Technical Report, published as Report No DLR-GSOC TN 03-05, German Space Operations Center (GSOC), pp. 9, Deutsches Zentrum für Luft- und Raumfahrt (DLR)

Muthuraman, K. and D. Borio (2010) "C/N0 Estimation for Modernized GNSS Signals: Theoretical Bounds and a Novel Iterative Estimator," in *NAVIGATION: Journal of The Institute of Navigation*, Vol. 57, pp. 309-323

Ni, J., D. Arndt, P. Ngo, P. Chau, K. Dekome, and J. Dusl (2010) "Ultra-Wideband Time-Difference-Of-Arrival High Resolution 3D Proximity Tracking System," in *Proceedings of the Proceedings of IEEE/ION Position Location and Navigation Symposium (PLANS)*, , Indian Wells, CA, The Institute of Navigation, pp. 37-42

NovAtel Inc. (2005) *OEM4 Family User Manual - Volume 2 Command and Log Reference*, User Manual, published as Report No OM-20000047 Rev 18, NovAtel Inc., 74-76 pages

O'Driscoll, C., D. Borio, M. Petovello, T. Williams, and G. Lachapelle (2006) "The Soft Approach - A recipe for a Multi-System, Multi-Frequency GNSS Receiver," *InsideGNSS*, vol. IV, July, Gibbons Media & Research LLC, Eugene, OR, pp. 46-51

Pany, T. and B. Eissfeller (2006) "Use of a Vector Delay Lock Loop Receiver for GNSS Signal Power Analysis in Bad Signal Conditions," in *Proceedings of the Proceedings of IEEE/ION PLANS 2006*, , San Diego, CA, The Institute of Navigation, pp. 893-903

Pany, T., B. Eissfeller, G. W. Hein, and D. Sanroma (2004) "ipexSR: A PC Based Software GNSS Receiver Completely Developed in Europe," in *Proceedings of the Proceedings of the GNSS 2004 European Navigation Conference*, , Rotterdam, Netherlands, The European Navigation Conference

Petovello, M. G. and G. Lachapelle (2006) "An Efficient New Method of Doppler Removal and Correlation with Application to Software-Based GNSS Receivers," in *Proceedings of the Proceedings of the 19th International Technical Meeting of the Satellite Division of The Institute of Navigation*, , Fort Worth, TX, The Institute of Navigation, pp. 2407 - 2417

Petovello, M. G. and G. Lachapelle (2006) "Comparison of Vector-Based Software Receiver Implementations with Application to Ultra-Tight GPS/INS Integration," in *Proceedings of the ION GNSS 2006*, 26-29 September, Fort Worth, The Institute of Navigation, pp. 10

Petovello, M. G., C. O'Driscoll, and G. Lachapelle (2007a) "Ultra-Tight GPS/INS for Carrier Phase Positioning In Weak-Signal Environments," in *Proceedings of the NATO RTO SET-104 Symposium on Military Capabilities Enabled by Advances in Navigation Sensors*, 1-2 October, Antalya, Turkey, NATO, pp. 18

Petovello, M. G., K. O'Keefe, B. Chan, S. Spiller, and C. Pedrosa (2010) "Demonstration of Inter-Vehicle UWB Ranging to Augment DGPS for Improved Relative Positioning," in *Proceedings of the ION GNSS 2010*, 21-24 September, Portland, OR, The Institute of Navigation

Petovello, M. G., D. Sun, G. Lachapelle, and M. E. Cannon (2007b) "Performance Analysis of an Ultra-Tightly Integrated GPS and Reduced IMU System," in *Proceedings of the Proceedings of the 20th International Technical Meeting of the Satellite Division of The Institute of Navigation*, , Fort Worth, TX, The Institute of Navigation, pp. 602-609

Petovello, M. G. (2011) "GNSS Solutions: The differences in differencing," *InsideGNSS*, vol. VI, September, Gibbons Media and Research LLC, Eugene, OR, pp. 28-32

Psiaki, M. L. and H. Jung (2002) "Extended Kalman Filter Methods for Tracking Weak GPS Signals," in *Proceedings of the ION GPS 2002*, 24-27 September, Portland, Oregon, The Institute of Navigation, pp. 2539-2553

Psiaki, M. L. (2001) "Smoother-Based GPS Signal Tracking in a Software Receiver," in *Proceedings of the ION GPS 2001*, 11-14 September, Salt Lake City, The Institute of Navigation, pp. 2900-2913

Ray, J. K. (2000) *Mitigation of GPS Code and Carrier Phase Multipath Effects Usinga Multi-Antenna System*, PhD Thesis, published as Report No UCGE Report No. 20136, University of Calgary, pp. 260, Department of Geomatics Engineering

Schamus, J. J. and T. B.Y. Tsui (1999) "Acquisition to Tracking and Coasting for Software GPS Receiver," in *Proceedings of the Proceedings of the 12th International Technical Meeting of the Satellite Division of The Institute of Navigation*, , Nashville, TN, The Institute of Navigation, pp. 325-328

Schamus, J. J., J. B.Y. Tsui, and D. M. Lin (2002) "Real-Time Software GPS Receiver," in *Proceedings of the Proceedings of the 15th International Technical Meeting of the Satellite Division of The Institute of Navigation*, , Portland, OR, The Institute of Navigation, pp. 2561-2565

Spilker, J. J. (1996) "Fundamentals of Signal Tracking Theory," [Chapter 7] in *Global Positioning System: Theory and Applications - Volume I, American Institute of Aeronautics and Astronautics Inc., Washington DC, 245-327*

Thor, J., P.L. Normark, and C. Ståhlberg (2002) "A High-Performance Real-Time GNSS Software Receiver and its Role in Evaluating Various Commercial Front End ASICs," in Proceedings of the Proceedings of the 15th International Technical Meeting of the Satellite Division of The Institute of Navigation, , Portland, OR, The Institute of Navigation, pp. 2554-2560

Tsui, J. B.Y. (2005) "Acquisition of GPS C/A Code Signals," [Chapter 7] in Fundamentals of Global Positioning System Receivers - A Software Approach, 2nd Ed, John Wiley & Sons, Inc., Hoboken, NJ, 129-159

Van Dierendonck, A. J. (1996a) "Signal Acquisition," [Chapter 8] in Global Positioning System: Theory and Applications - Volume I, American Institute of Aeronautics and Astronautics Inc., Washington DC, 367-368

Van Dierendonck, A. J. (1996b) "Digital Signal Processing," [Chapter 8] in Global Positioning System: Theory and Applications - Volume I, American Institute of Aeronautics and Astronautics Inc., Washington, DC, 356-357

Van Dierendonck, A. J. (1996c) "Lock Detectors," [Chapter 8] in Global Positioning System: Theory and Applications - Volume I, American Institute of Aeronautics and Astronautics Inc., Washington DC, 390-394

van Diggelen, F. (2009a) A-GPS - Assisted GPS, GNSS, and SBAS, Artech House, Boston, pp. 43-60, 978-1-59693-374-3

van Diggelen, F. (2009b) "The Smartphone Revolution," GPS World, December, pp. 36-40

van Diggelen, F. (2009c) A-GPS - Assisted GPS, GNSS, and SBAS, Artech House, Boston, pp. 186-193, 978-1-59693-374-3

van Graas, F., A. Soloviev, M. Uijt de Haag, Gunawardena, and M. Braasch (2005) "Comparison of Two Approaches for GNSS Receiver Algorithms: Batch Processing and Sequential Processing Considerations," in Proceedings of the Proceedings of the 18th International Technical Meeting of the Satellite Division of The Institute of Navigation, , Long Beach, CA, The Institute of Navigation, pp. 200-211

Vydhyanathan, A., H. Luinge, M. Tanigawa, F. Dijkstra, M. S. Braasch, and M. Uijt de Haag (2009) "Augmenting Low-cost GPS/INS with Ultra-wideband Transceivers for Multi-platform Relative Navigation," in Proceedings of the Proceedings of the 22nd International Technical Meeting of The Satellite Division of The Institute of Navigation, , Savannah, GA, The Institute of Navigation, pp. 547-554

Wallner, S. and J. Á. Ávila-Rodríguez (2011) "Codes: The PRN Family Grows Again," InsideGNSS, vol. VI, September, Gibbons Media & Research LLC, Eugene, Oregon, pp. 83-92

Ward, P. W., J. W. Betz, and C. J. Hegarty (2006) "Satellite Signal Acquisition, Tracking, and Data Demodulation," [Chapter 5] in Understanding GPS: Principles and Applications, 2nd Ed, Artech House Inc., Boston, MA, 153-241

Watson, R., G. Lachapelle, R. Klukas, S. Turunen, S. Pietilä, and I. Halivaara (2006) "Investigating GPS Signals Indoors with Extreme High-Sensitivity Detection Techniques," in Navigation: Journal of The Institute of Navigation, Vol. LII, Issue 4, pp. 199-213

Won, J.H., D. Dötterböck, and B. Eissfeller (2009) "Performance Comparison of Different Forms of Kalman Filter Approach for a Vector-Based GNSS Signal Tracking Loop," in Proceedings of the ION GNSS 2009, 22-25 September, Savannah, Georgia, The Institute of Navigation, pp. 3037-3048

Xu, H., L. Yang, and J. Y.T. Morton (2007) "Positioning and Navigation with Ultra-Wideband Signals," in Proceedings of the Proceedings of the 20th International Technical Meeting of the Satellite Division of The Institute of Navigation, , Fort Worth, TX, The Institute of Navigation, pp. 1861 - 1866

Xu, H. (2006) "Long-Range High-Accuracy UWB Ranging for Precise Positioning," in Proceedings of the Proceedings of the 19th International Technical Meeting of the Satellite Division of The Institute of Navigation, , Fort Worth, TX , The Institute of Navigation, pp. 83 - 94

Yan, J. and G. Bellusci (2009) "Low-complexity Ultra-Wideband Indoor Positioning," in Proceedings of the Proceedings of the 22nd International Technical Meeting of The Satellite Division of The Institute of Navigation, , Savannah, GA, The Institute of Navigation, pp. 1013-1024

Ziedan , N. I. and J. L. Garrison (2004) "Extended Kalman Filter-Based Tracking of Weak GPS Signals under High Dynamic Conditions," in Proceedings of the Proceedings of the 17th International Technical Meeting of the Satellite Division of The Institute of Navigation, , Long Beach, CA, The Institute of Navigation, pp. 20-31